Proceedings of the Tenth Asian Congress of Fluid Mechanics
17-21 May 2004, Peradeniya, Sri Lanka

MODE 2 INSTABILITY OF THE SHIELDED MONOPOLAR VORTEX

A. Ooi, K. Higgins and M. S. Chong

(Department of Mechanical and Manufacturing Engineering,
University of Melbourne, Victoria, 3010 AUSTRALIA)

ABSTRACT:

It has been reported in the literature that azimuthal mode 2 perturbation of the shielded monopolar vortex can lead to complex multipolar vortex structures. These vortex structures include the tripole and the splitting of the vortex into two separating dipoles. From two-dimensional nonlinear Navier-Stokes calculations, it is shown in this paper that the formation of a different vortex structure is possible. This vortex structure is similar to the tripole, but the separation of the satellite vortices is larger. The satellite vortices in this structure are surrounded by patches of positive vorticity. However, this vortex configuration only emerges when the initial mean vorticity profile has a very high gradient.

1. INTRODUCTION

The evolution of azimuthal mode 2 instability of an shielded monopolar vortex has been investigated by various researchers. The interest in this flow comes from the need to obtain a fundamental understanding of the physical mechanism of the dynamics of coherent structures, which contain most of the kinetic energy in "two-dimensional turbulent flows". These studies have reported that depending on the steepness of the initial axisymmetric vorticity profile (usually measured by the parameter, α), different vortex structures will form. [3] and [8] have reported that if $1.8 < \alpha < 3.2$, then instabilities will result in the formation of a stable tripole structure. The tripolar structure, which consist of a large core and two satellite vortices of the opposite sign, has also been observed in a rotating tank experiment by [11]. If $\alpha > 3.2$, recent numerical simulations by [1] have shown that the resulting flow field is two separating dipoles. The tripolar and separating vortex dipole structure have also been simulated by [8] and they are the two most common vortex structures that have been studied in the open literature. Another vortex structure that can form from the perturbation of azimuthal mode 2 is similar to the tripole, but the satellite vortices are further apart than the tripolar vortex. In addition, there are patches of positive vorticity surrounding the satellite vortices. Similar vortex structure has been observed by [4] with numerical data obtained from inviscid contour dynamics simulations.

2. NUMERICAL SIMULATIONS

In this study, numerical data was obtain by solving the two-dimensional incompressible Navier-Stokes equations in the cylindrical coordinate system. A hybrid spectral-fourth order finite difference numerical scheme was used. An algebraic mapping was employed in the radial direction to map the computational domain (which is from $\eta \in [0, 1]$) to $r \in [0, \infty)$. Details of the numerical method can be found in [2].

We carry out simulations with initial conditions

$$\omega(r, \theta, t = 0) = \omega_\alpha(r) + \omega^{'}(r, \theta) \tag{1}$$

where $\omega_\alpha(r)$ is the shielded monopolar vortex given by

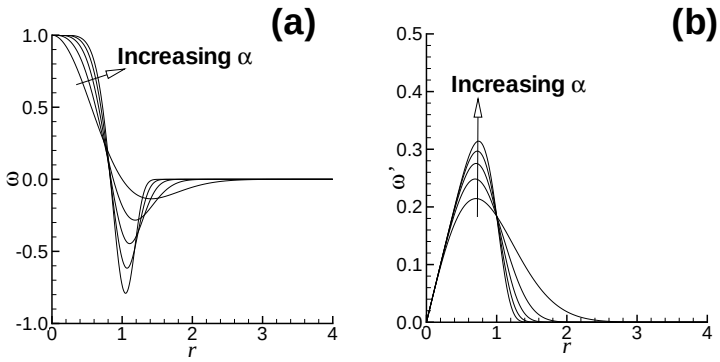

Figure 1: Initial vorticity and perturbation. (a) Axisymmetric profile (b) profile for perturbation introduced into the axisymmetric vorticity profile.

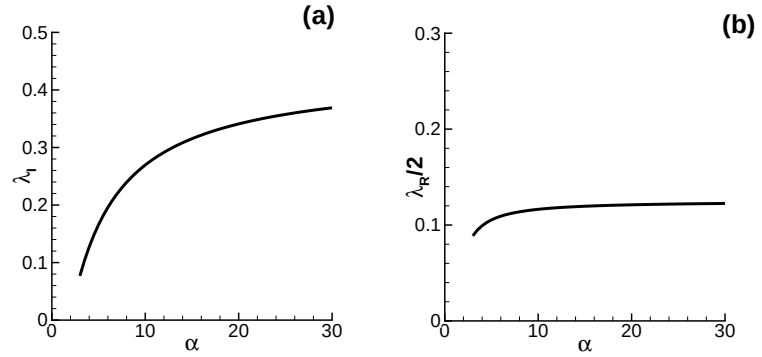

Figure 2: Results of inviscid stability analysis. (a) maximum growth rate and (b) phase speed.

$$\omega_\alpha(r) = \left(1 - \frac{1}{2}\alpha r^\alpha\right) e^{-r^\alpha}. \tag{2}$$

and $\omega^{'}(r,\theta)$ is the initial perturbation of the axisymmetric vorticity field. Equation 2 is shown in Fig. 1 (a) . This vorticity distribution is positive at the center and has a ring of negative vorticity around the central core. The total circulation of this initial vorticity distribution is zero. α is the steepness parameter with higher values of α leading to higher gradients in ω_α.

The functional form of the perturbation function is given by

$$\omega^{'}(r,\theta) = \mu r^{k'} \cos(k'\theta) \exp\left[\frac{-(\alpha r^\alpha - 2)^2}{2\sigma^2}\right] \tag{3}$$

and is shown in Fig. 1 (b). The amplitude of the perturbation is controlled by the parameter μ. k' is the wavenumber corresponding to the azimuthal mode that is perturbed. Note that the initial perturbation (Eq. (3)) is similar to the perturbation function used by other authors. There is, however, a difference. The function $\omega^{'}$ has been multiplied by $r^{k'}$ to ensure that the initial

vorticity distribution satisfies the pole conditions at $r = 0$, i.e. the azimuthal Fourier coefficient, $\hat{\omega}_k(r)$ must decay like r^k as r approaches zero. For more information on the pole conditions, see [7] and [10].

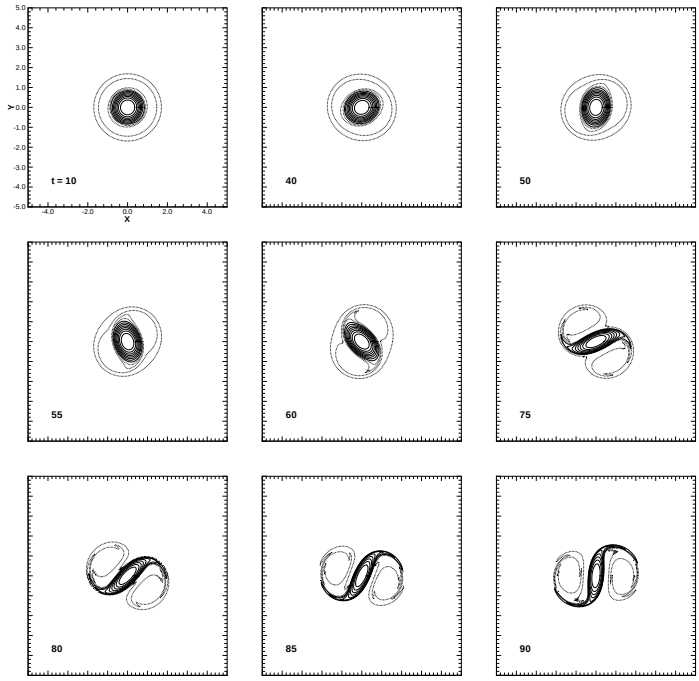

Figure 3: Evolution of vorticity contours for simulation A with $\alpha = 3.0$ and $\sigma = 0.23$.

To ensure that the initial perturbations will grow, a stability analysis was carried out. The perturbations are assumed to be normal modes of the form,

$$\psi^{'}(r, \theta, t) = \phi(r) e^{i(k'\theta - \lambda t)}, \tag{4}$$

where $\psi^{'}$ is the streamfunction corresponding to the perturbed velocity field. λ is a complex variable which can be decomposed into real (λ_R) and imaginary (λ_I) parts. The governing equations were linearised and the growth rates (λ_I) and phase speed ($\lambda_R/2$) of the perturbation can be obtained as a function of α. Results from this analysis is shown in Fig. 2. The maximum growth rate (Fig. 2 (a))and corresponding phase speed (Fig. 2 (b)) of the azimuthal enstrophy mode 2 is plotted against the steepness parameter, α. Similar analysis has been carried out before by [1], [9], [6] and [5] but for a smaller range of α. It is clear from the data shown in Fig. 2 (a) that higher growth rates will occur at higher values of α. It also appears that the phase speed is relatively constant for the range of α values investigated here. Since the behaviour of azimuthal mode 2 instability correspond to the properties of satellite vortices, one can expect from this analysis that the satellites will be of higher intensity but rotate at relatively constant speed for simulations with higher values of α.

Simulations have been carried out to investigate the effect of the higher initial growth rate of azimuthal mode 2 on the eventual flow field. Table 1 below summarizes the parameters used in the numerical simulations. In all calculations, $\mu = 0.25$ and $k' = 2$. As we vary α (and hence change the initial mode 2 growth rate), the total enstrophy of azimuthal mode $k = 2$,

$$A_k(t) = 2\pi \int_0^\infty \hat{\omega}_k(t) \hat{\omega}_k^*(t) r dr, \tag{5}$$

Simulation	N_r	N_θ	α	σ	$A_2(t=0)$
A	256	256	3.0	0.23	0.0435
B	512	512	10.0	0.85	0.0431
C	512	512	25.0	1.20	0.0433

Table 1: Table showing the parameters used in the simulations

changes. Here, the asterisk indicates complex conjugation. Thus, σ is adjusted to ensure that $A_2(t=0)$is similar for all three simulations.

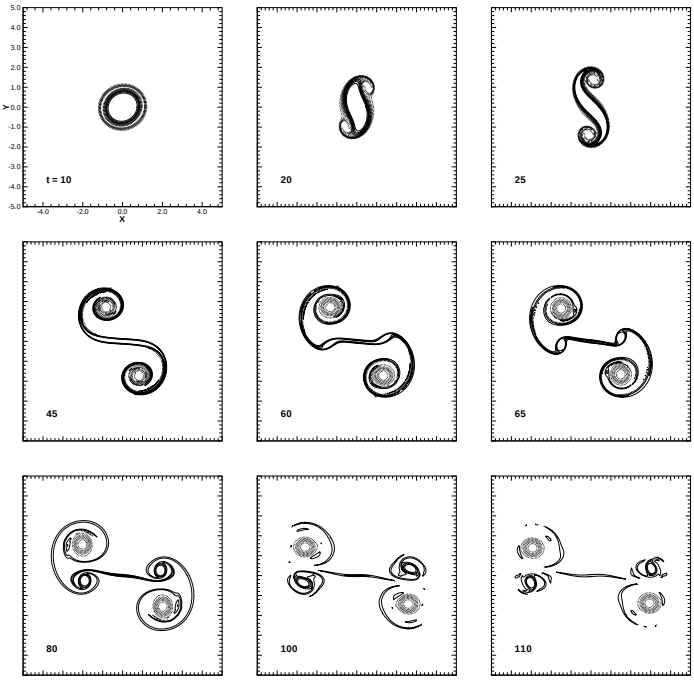

Figure 4: Evolution of vorticity contours for simulation B with $\alpha = 10.0$ and $\sigma = 0.85$.

3. RESULTS AND DISCUSSIONS

Evolution of vorticity contours for simulation A is shown in Fig. 3. Initially, the axisymmetric ($k = 0$) mode is dominant and the vorticity contours appear circular. As the vorticity field evolves, the $k = 0$ mode grows and eventually the tripolar vortex is formed. This structure, which has been investigated by many researcher before such as [6], consist of a central core vortex with two smaller satellites vortices of the opposite sign rotating around the core vortex. The tripolar vortex structure appear to be stable. The two satellites revolves around the positive central core for the whole duration of our simulation.

Figure 4 shows the evolution of the vorticity contours for simulation B. Initially, the vorticity contours are circular indicating that most of the enstrophy is contained in the $k = 0$ mode. Due to the growth of the enstrophy in the azimuthal mode $k = 2$, the satellite vortices emerge but the tripolar vortex structure (which existed in the previous simulation) does not eventuate. Instead, for this case, the positive vorticity at the core is 'torn' by the strain field generated by the satellite vortices. As a result, two vortex dipoles are formed and they move in opposite directions. This phenomena has been observed before by [1] and [4], and is commonly known as dipole-splitting.

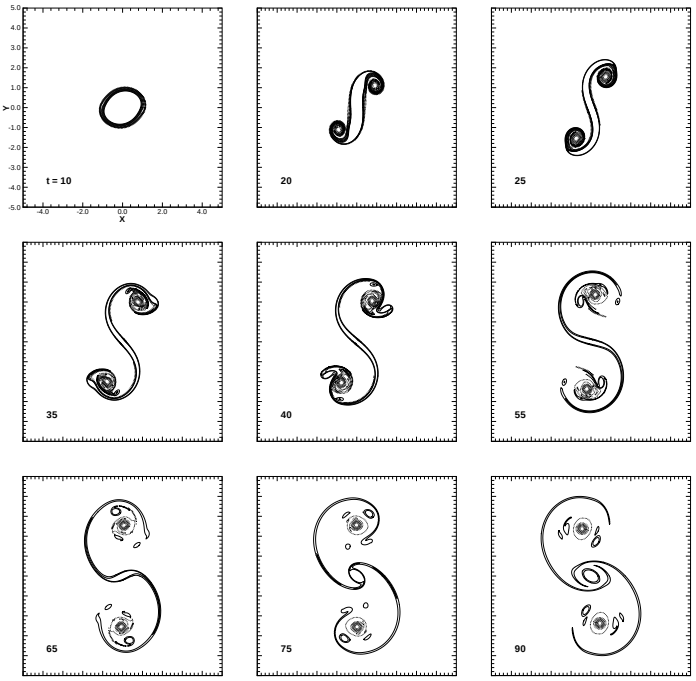

Figure 5: Evolution of vorticity contours for simulation C with $\alpha = 25.0$ and $\sigma = 1.2$.

Figure 5 shows the vortex evolution for the simulation carried out with $\alpha = 25$. Because of the high initial growth rate of azimuthal mode 2, the two satellites become quite strong and 'tear' the central vortex apart. The positive vorticity does not pair up with the satellites to produce vortex dipoles as in case B. Instead, the positive vorticity entrained by the satellites become very thin and become unstable. Instability develops in the tip of thin vortex layer which eventually breaks down into smaller positive vorticity which surrounds the satellites. The eventual structure is similar to the tripolar vortex. However, the satellites are further apart and have patches of positive vorticity surrounding them. Similar vortex structures have been observed by [4] using a nonlinear inviscid contour dynamics approach which shows that this is not a viscous effect.

Evolution of the azimuthal entrosphy modes, $A_k(t)$, for all simulations is shown in Fig. 6. Initially, due to the initial conditions used in the simulations, all the entrosphy is only concentrated in the $k = 0$ and $k = 2$ mode. As the flow evolves, the nonlinear interaction in the convective terms of the governing equations introduces energy into the higher modes. The enstrophy in all modes grows and eventually saturates owing to the action of viscous diffusion. As predicted by the linearised inviscid analysis, the initial growth rate for $A_2(t)$ is greater for simulations carried out with larger values of α.

4. CONCLUSIONS

Numerical simulations were carried out to investigate the various vortex structures that can result from the azimuthal mode 2 perturbation of the shielded monopolar vortex. Inviscid linear stability analysis has been conducted for a large range of steepness parameter, α, and it is shown that the maximum growth rate for mode 2 increases with α. The phase speed of the perturbation does not appear to vary much with α.

Results from two-dimensional nonlinear viscous Navier-Stokes simulations demonstrates that different vortex structures can result from simulations with different values of α. The three vortex structures observed in the simulations here are the tripolar vortex, dipole splitting and the 'long

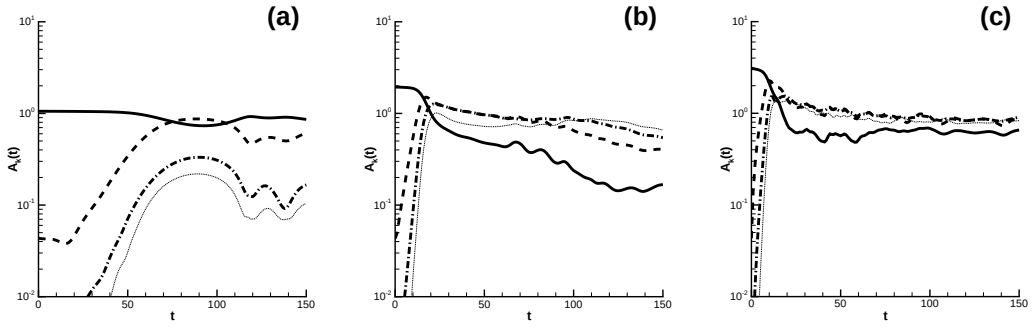

Figure 6: Evolution of azimuthal enstrophy modes for all simulations. $\alpha = 0.23$ (a), $\alpha = 10$ (b), $\alpha = 25$ (c). —— $A_0(t)$, - - - - $A_2(t)$, —·— $A_4(t)$, and ····· $A_6(t)$.

tripole'. The first two has been reported by many investigators previous. The 'long tripole' is not that common. This vortex structure consist of satellite vortices that are further apart from the central core compared to the tripole. These satellites have patches of positive vorticity surrounding them. The 'long tripole' appears to be stable and does not break down for the whole duration of the simulation carried out here.

REFERENCES

[1] Beckers M, Clercx H, van Heijst G and Verzicco R. "Evolution and instability of monopolar vortices in a stratified fluid". *Phys. Fluids*, 2003. **15**(4), 1033–1045.

[2] Buntine J and Pullin D. "Merger and cancellation of strained vortices". *J. Fluid Mech.*, 1989. **205**, 263–295.

[3] Carton X and Legras B. *J. Fluid Mech.*, 1994. **267**, 58–82.

[4] Flierl G. "On the instability of geostrophic vortices". *J. Fluid Mech.*, 1988. **197**, 349–388.

[5] Gent P and McWilliams J. "The instability of barotropic circular vortices". *Geosphys. Astrophys. Fluid Dynamics*, 1986. **35**, 209–233.

[6] Kloosterziel R and Carnevale G. "On the evolution and saturation of instabilites of two-dimensional isolated circular vortices". *J. Fluid Mech.*, 1999. **388**, 217–257.

[7] Kollmann W and Roy J. "Hybrid navier-stokes solver in cylindrical coordinates i: Method". *Computational Fluid Dynamics Journal*, 2000. **9**(2), 1–16.

[8] Morel Y and Carton X. "Multipolar vortices in two-dimensional incompressible flows". *J. Fluid Mech.*, 1994. **267**, 23–51.

[9] Orlandi P and Carnevale G. "Evolution of isolated vortices in a rotating fluid of finite depth". *J. Fluid Mech.*, 1999. **381**, 239–269.

[10] Shen J. "Efficient spectral-galerkin methods iii: Polar and cylindrical geometries". *SIAM J. Sci. Computing*, 1997. **18**, 1583–1604.

[11] van Heijst G.J.F. and Kloosterziel R. "Tripolar vortices in a rotating fluid". *Nature*, 1989. **338**, 569–571.

Proceedings of the Tenth Asian Congress of Fluid Mechanics
17-21 May 2004, Peradeniya, Sri Lanka

INFLUENCE OF CROSS SECTIONAL SHAPE ON VORTEXING DURING DRAINING FROM CYLINDRICAL TANKS: A PIV STUDY

B.H.L. Gowda
Fluid Mechanics Laboratory, Department of Applied Mechanics, IIT Madras, India

S. Mizuki, T. Uchibaba and H. Tsujita
Fluid Mechanics Laboratory, Department of Mechanical Engineering, Hosei University, Tokyo, Japan

ABSTRACT: When liquid drains from a cylindrical container a vortex with a central air core is formed. The air core reduces the drain port area thus decreasing the rate of draining. Initial rotation is found to augment this phenomenon. In this study, the effect of the cross sectional shape of the container on the vortexing phenomenon is investigated using PIV technique. It is found that in a container with square cross-section vortexing is prevented as the rotation imparted to the liquid decays very fast. In the case of cylindrical cross-section a vortex-suppressor is needed to suppress vortexing.

1. INTRODUCTION

During draining of liquid from a circular tank through an axisymmetrically placed circular orifice (drain), a vortex with an air core forms, as the free surface level reaches a critical height, H_c. The vortex extends to the bottom port, reducing the effective cross sectional area of the drain outlet and consequently the flow rate. Initial disturbances like rotational motion and vibration due to environmental disturbances can augment the vortex formation [1-3]. This phenomenon has practical relevance in fuel feed systems in space vehicles and rockets. During flight of space vehicles and rockets, such vortexing can affect the out flow from liquid propellant tank to the engines.

Gowda *et al*. [4] have suggested a simple device to suppress vortexing in circular tanks. In square and rectangular tanks it is found that vortexing does not occur even without a suppressor [5]. The reasons for the above are not clear. In this study an attempt is made to understand the mechanism responsible for it. With this objective, the flow field in cylindrical tanks with circular and square cross sections are visualized using PIV. Results are obtained without and with draining, after imparting rotation to the liquid in the tank.

2. EXPERIMENTAL SET UP

Acrylic tanks (test tanks) with circular and square cross sections, both having same cross sectional areas are utilized. In Fig.1a is shown the circular test tank. It is enclosed by another larger square tank and the space between the two is filled with water. This was needed to light the entire cross section of the circular test tank by the laser sheet while photographing. In case of square test tank such an arrangement was not needed. Rotation is imparted to the liquid in the container by controlled stirring (with the drain port closed by a rubber stopper) using varying number of revolutions of the stirrer over a constant period of time [3-5]. The dish-type suppressor (Fig.1b) is made of brass with suitable mesh size [4]. The dimensions are such that the dish can be pushed down the tank and made to occupy the position at the bottom.

For flow visualization two YAG lasers are used for a source of light sheet (Fig.1c). The tracers passing through the light sheet are visualized. In the present study, in order to visualize the flow patterns, the laser sheet is made to pass through the tank in horizontal planes at various values of height H_s (Fig.1a) and in a vertical plane through the axis of the test tank. The flow patterns are recorded by a HDTV (High Definition TV) camera located normal to the light sheet. The HDTV camera is connected to YAG lasers by a synchronizer (Fig.1c). The synchronizer controls the flash intervals of the laser sheet. Flash intervals of 3 ms for the horizontal plane and 15 ms for the vertical plane are used to record the movement

of the tracers. The tracers are white polystyrene particles with the specific gravity of 1.03, whose sizes are about 35~75 μm.

3. EXPERIMENTAL PROCEDURE

As mentioned earlier, rotation is imparted to the liquid in the container by controlled stirring (with the drain port closed by a rubber stopper) using varying number of revolutions of the stirrer over a constant period of time. The revolutions are imparted manually and to check the reliability of the results obtained the experiments are repeated several times [3-5]. The liquid used is water at room temperature. After imparting rotation, the rubber stopper is removed and the draining started. The results are obtained keeping the same initial height of water, H_i = 350 mm for all runs. This was chosen so that the critical height H_c and the time of draining can be conveniently measured. Experiments are carried out without suppressor (case : WOTS) and with suppressor (case : WS).

Rotation is imparted and simultaneously YAG lasers are started to produce light sheet for horizontal and vertical planes. After imparting rotation, the time dependent behavior of the flow pattern is recorded by using HDTV camera located normal to the laser sheet. The flow patterns captured for obtaining the velocity vectors by means of the flow analysis software are not in color. Micro AVS is used for making the final flow visualization so that the magnitude of velocities are clearly seen in fine color. For this purpose a special programme was written and utilized.

4. RESULTS

Flow visualization is carried out in horizontal planes at H_s = 50, 100, 150 and 200 mm (Fig.1a) and in vertical plane passing through the axis. Results are obtained without and with draining at various intervals of time `t'. The time `t' is the time elapsed after giving rotation. Results are obtained at t = 3, 5, 10, 15, 20, 30. 40 and 50 seconds. Here, the results at H_s = 100 mm only are described as the results at other heights are qualitatively the same. Considering the results in the horizontal plane at t = 3s (Fig.2), it is seen that the structure of the flow fields are much different for the three cases considered. At t = 3s, for the circular section, without suppressor (WOTS) the rotational velocities are nearly uniform over the entire cross section with a very small central core of low velocities. With suppressor (WS) the pattern is much different; a outer peripheral region with high rotational velocities and a much larger core with reduced velocities occur. For the square cross section, even without suppressor, the reduction in the magnitude of velocities and the change in the pattern of velocity vectors is striking. Even at t = 3s, the effect of imparted rotation appears to have very much dissipated. When the results at t = 10s (Fig.3) are considered, it is seen that for the circular tank the decay is very slow for the WOTS case compared to the WS case. For the square tank, the velocities become very small. Further, rotational trend in the velocity vectors is seen only in a small region near the core. The decay continues with increase in time.

The results in the vertical plane at t = 10s are given in Fig.4. The results at 3s (not included) show that the structure of the flow in the three cases are different. This is more strikingly seen in Fig.4 (t = 10s). In the WOTS case there is a region of high velocity in the shape of a inverted cone. In the WS case for the circular cross-section, there is considerable reduction in the region of high velocity between 3 and 10s. However a stronger decay is seen in the case of the square tank at 10s similar to that observed in the horizontal plane. Further, the structure of the flow pattern is different compared to the other two. The square shape with its sharp corners appears to give rise to bands of vortical structure along its height. Thus the square shape affects both the rate of decay and the structure of the flow. It is interesting to note that the mechanism of vortex suppression in a square tank (without suppressor) and that in a circular tank with suppressor are different.

Visualization is also done with draining after imparting rotation. Due to draining, the water levels in the tanks reduce with time and results at any height can be obtained only over limited time intervals. The results upto 9s in the horizontal plane at H_s = 100 mm are obtained. From these results the very rapid decay of the imparted rotation in the case of square container is clearly seen. Even at 3s the decay is very considerable compared to the other two cases.

In essence, the results indicate how vorticity imparted is either sustained or dissipated in the three cases considered. In the case of circular cross section, with suppressor, vorticity decays faster compared to that without suppressor. In the case of square cross section, the sharp corners in the changed geometry `kill' vorticity at a very rapid rate. This is probably the reason why vortexing is prevented in the latter two cases when draining is started after imparting rotation. The mechanism of vortex suppression appears to be different in the two cases.

5. CONCLUDING REMARKS

In circular tanks, a suppressor is needed to prevent vortexing. The suppressor dissipates vorticity imparted at a very fast rate and thus acts in suppressing the vortex. However, in the case of square cross section the changed geometry is seen to be effective in preventing vortexing even without a suppressor. The imparted rotation decays at a very fast rate with no chance for the vortex formation when draining is started. This has considerable practical implications in the design of liquid propellant tanks.

REFERENCES

[1] Lubin BT and Springer GS: The formation of a dip on the surface of a liquid draining from a tank. *J Fluid Mech*., 1967, 29, 385-390.

[2] Zhou QN and Graebel WP: Axisymmetric draining of cylindrical tank with a free surface. *J Fluid Mech*., 1990, 221, 511-532.

[3] Gowda BHL, Joshy PJ and Swarnamani SS: Influence of rotation and vibration on discharge of liquid from a cylindrical tank. *Ind.J Engg. & Material Sciences*, 1996, 3, 133-140.

[4] Gowda BHL, Joshy PJ and Swarnamani SS: Device to suppress vortexing during draining from cylindrical tanks. *J Spacecraft and Rockets*, 1996, 33, 598-600.

[5] Gowda BHL: Draining of liquids from tanks of square and rectangular cross sections. *J Spacecraft and Rockets*, 1996, 33, 311-312.

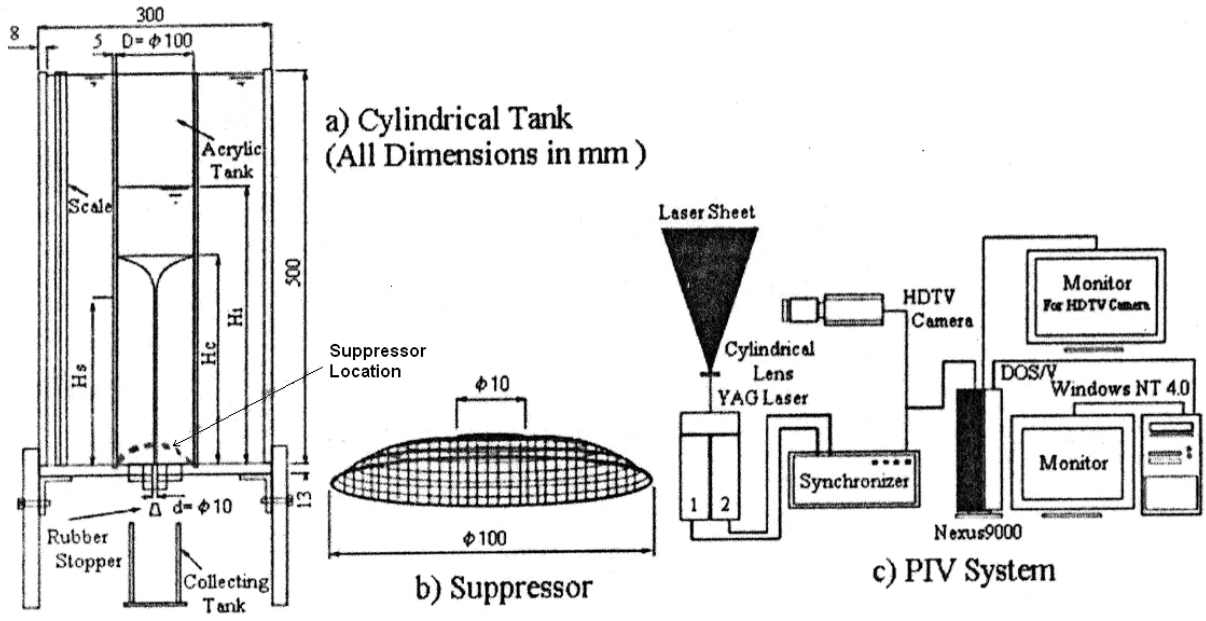

Fig.1 Experimental Arrangement

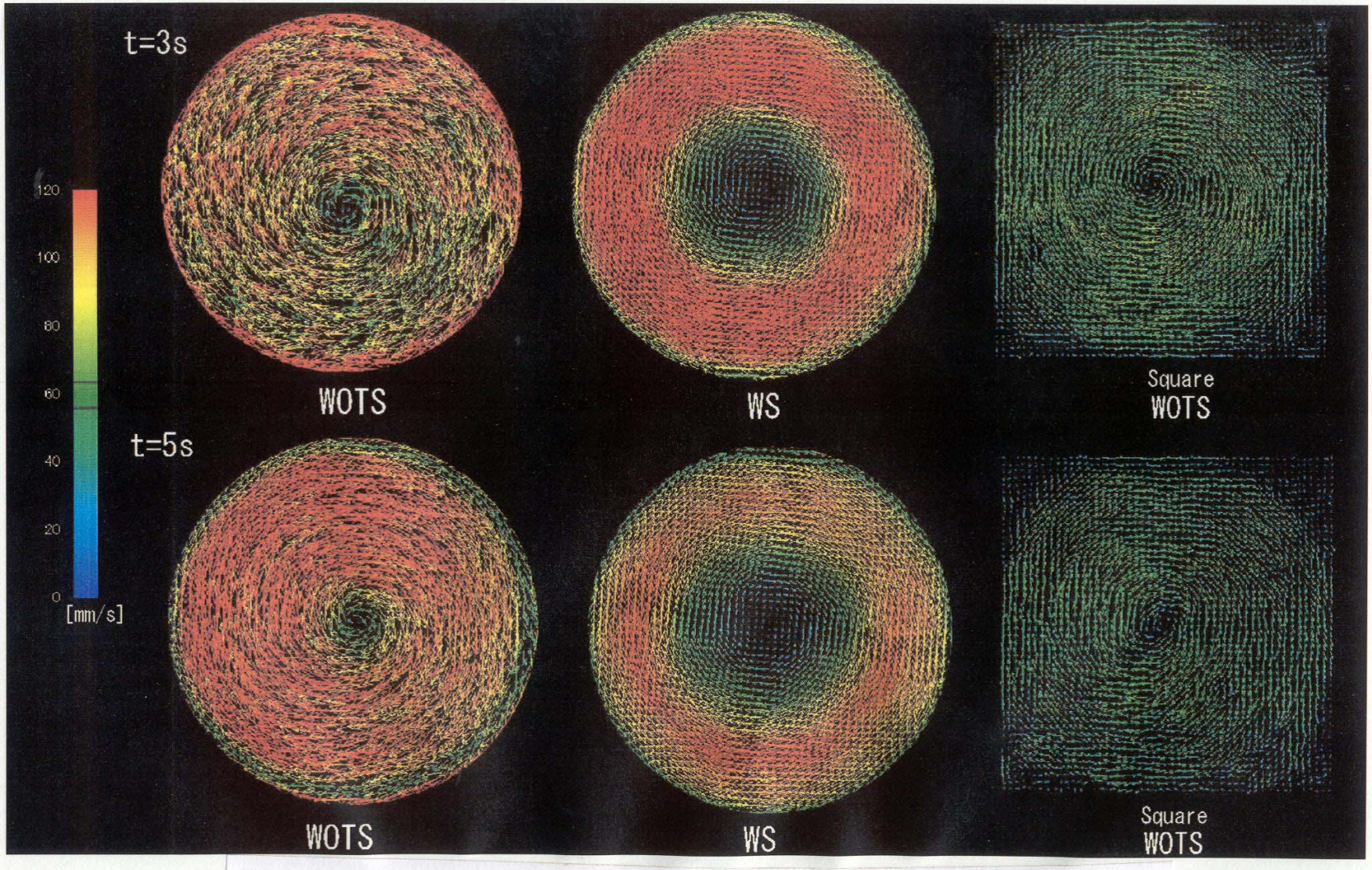

Fig.2 Velocity vectors in horizontal planes : RPM = 90 & H_s = 100mm (without draining : t = 3s & 5s)

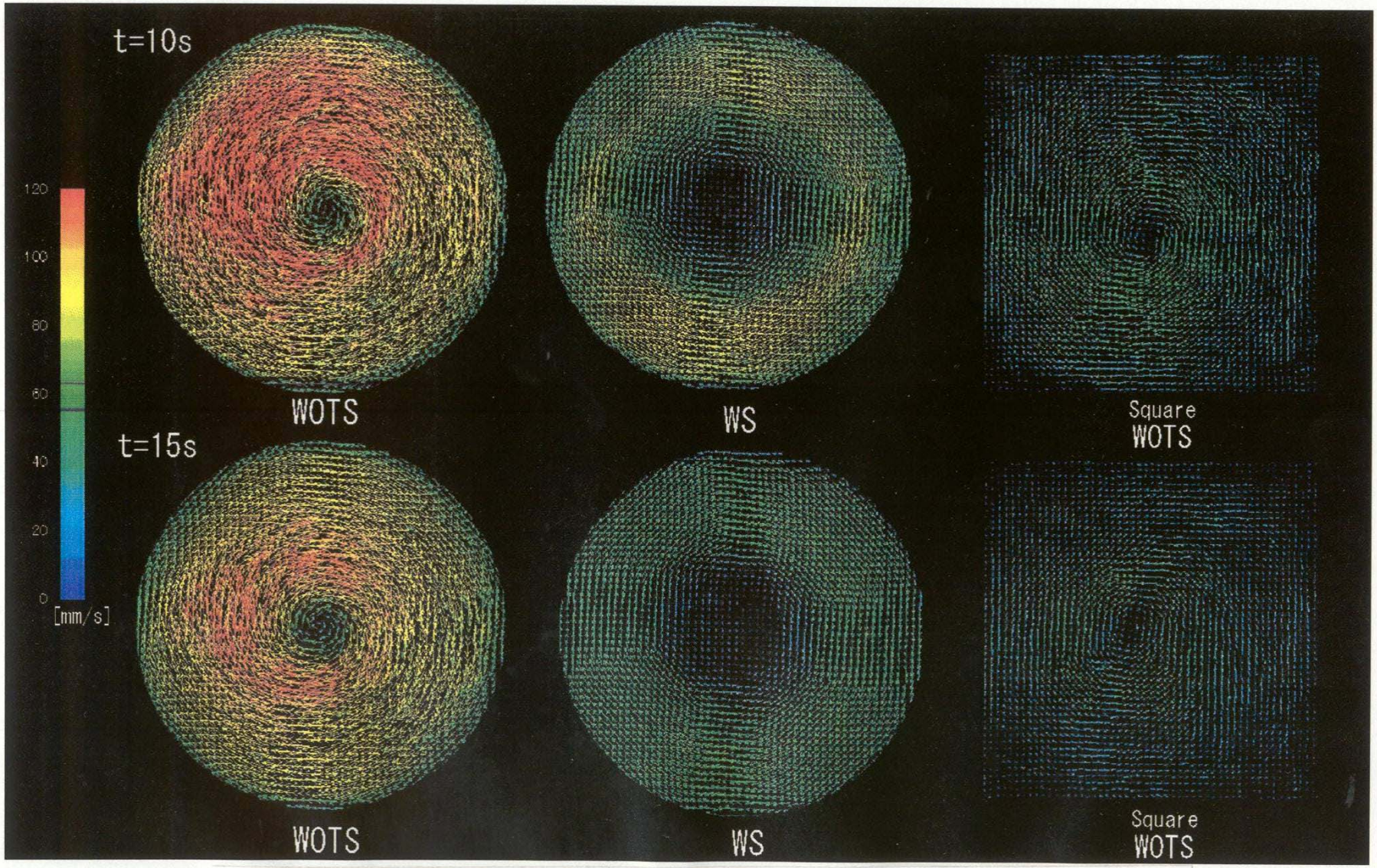

Fig.3 Velocity vectors in horizontal planes : RPM = 90 & H_s = 100mm (without draining : t = 10s & 15s)

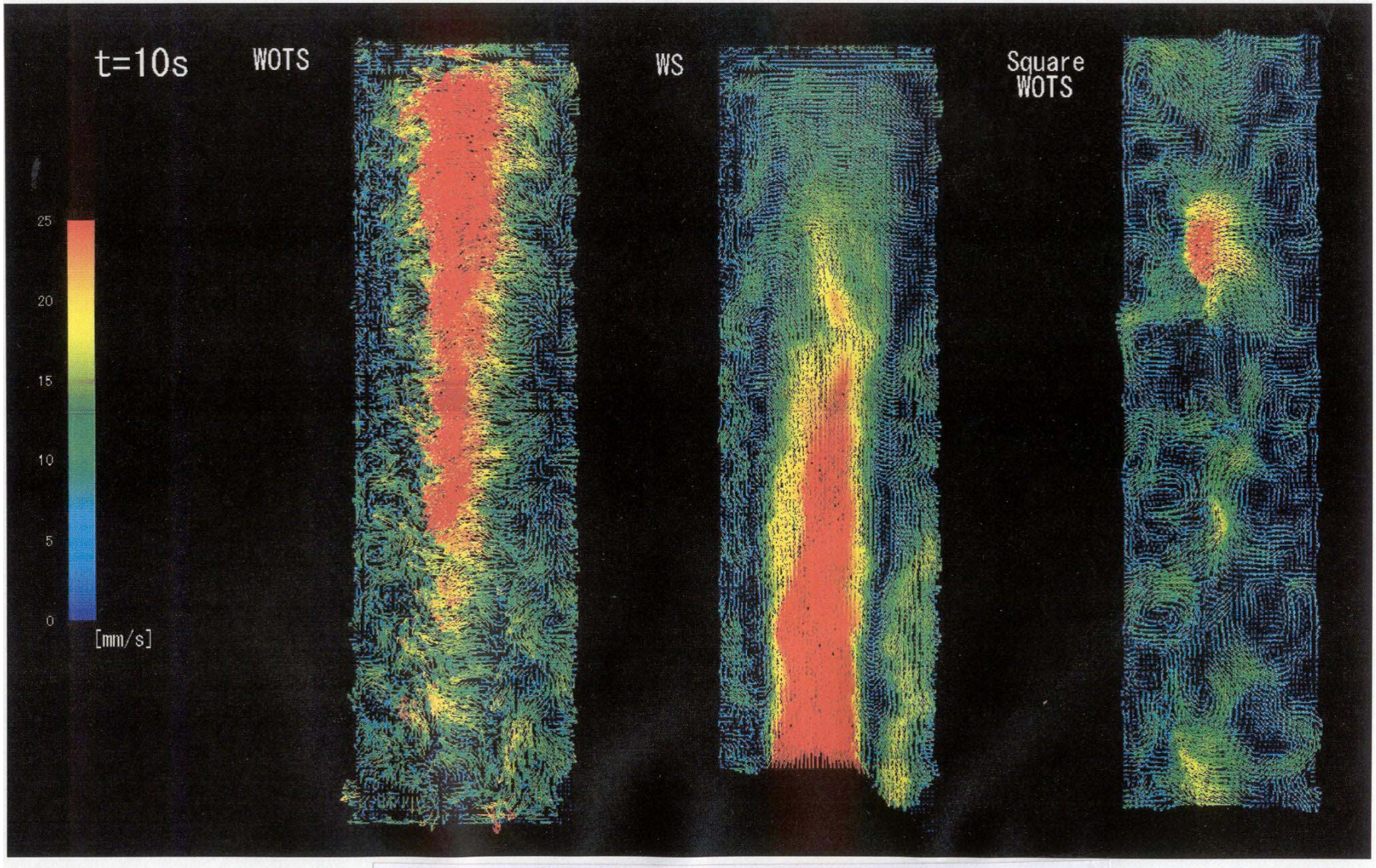

Fig.4 Velocity vectors in vertical plane : RPM = 90 (without draining : t = 10s)

Proceedings of the Tenth Asian Congress of Fluid Mechanics
17-21 May 2004, Peradeniya, Sri Lanka

WING-TIP VORTEX MEASUREMENT USING PIV

H. J. Zhang and Z. D. Su
Department of Metrological Engineering, China Institute of Metrology, Hang Zhou 310018, China

Y. Zhou
Department of Mechanical Engineering, The Hong Kong Polytechnic University, Hong Kong, China

ABSTRACT: Tip vortices generated from a rectangular half-span wing model (NACA 0012) have been experimentally investigated. A particle image velocimeter (PIV) was used to measure both qualitatively and quantitatively the velocity field in a plane normal to the flow at x/c = 3, where x is the downstream distance from the trailing edge of the wing model and c is the chord-length. The Reynolds number, Re_c, based on the chord-length, ranges between 3.4×10^4 and 26.6×10^4. The vorticity, tangential velocity, circulation of the tip vortices are examined in detail. The measurement agrees qualitatively well with previous reports. As the angle of attack (α) increases, the wing-tip vortex grows in both size and strength. It has been found that tip vortices occur rather symmetrically about one point in terms of its spatial location and strength for small α when flow separation is not evident, but become asymmetrical at a large α when flow separation occurs. The wandering phenomenon has also been studied based on the PIV data.

1. INTRODUCTION

Tip vortices are present in the wake of any finite lifting wing, and responsible for many adverse phenomena, such as the hazard posed by a large aircraft to following smaller aircraft and the damage caused by the vortices to the ground buildings, blade/vortex interaction on helicopter blades, and propeller cavitation on ships. Because of their practical significance, tip vortices have been a subject of extensive research for many decades.[1-6]

Wing-tip vortex is generated from the tip, and rolls up more and more as it moves downstream until its circulation is equal to that of the wing. The rollup distance is about several chord-lengths, [7,8] which is comparable with distance between interacting lifting surface, such as consecutive blades on a helicopter rotor, canard wings, sails of submarines and propeller blades. The near field behavior of a tip vortex is, therefore, important for these cases. Also, it is important in finding methods to destroy or control the far-field vortex. Some studies on the near field of a wing-tip vortex can be found in [7-9]. In these experimental studies on the wing-tip vortices, flow velocity was usually measured by pressure probe, hot wire probe, and LDV. These techniques have advantage, such as in the 3-dimensional measurement and statistical analysis.[7] However, they are not convenient in a flow field measurement. In the last decade, particle imaging velocimetry (PIV) technique has experienced a fast development accompanying with the occurring of high-speed computer. PIV system is suitable for flow field measurements and has been used to study many kinds of flow phenomena. However, there is very little work on tip vortex that has been made by PIV technique, possibly due to the difficulty in the implement to measure the longitudinal wing-tip vortices. [10]

In wind tunnel studies on wing-tip vortices, the problem of wandering is often encountered. [11,12] Wandering can lead to large errors in mean velocity and turbulence measurements by fixed probes, such as hot wire/film probe, multiple holes probe and LDV. For instance, Baker et al. [13] noted that the measurement error in the peak tangential velocity could be as much as 35%. Wandering may be self-induced or a consequence of free-stream unsteadiness, and is usually blamed on wind tunnel unsteadiness. Baker et al.[13] have made theoretical analysis of its effects. Further detailed analysis of wandering was performed by Devenport et al [11]. They developed a theory to correct mean-velocity profiles for the effects of wandering and to provide complete quantitative estimates of its amplitude and contributions to Reynolds stress fields. They found spectral decomposition was the most effective method of separating these contributions from velocity fluctuations due to turbulence. They found the wandering amplitudes to be typically less than 1% chord, or 30% of the core radius, in their special test condition of chord Reynolds number Re_c ($\equiv U_\infty c/\nu$,

where U_∞ is the main flow velocity, c is the chord-length, and ν is the kinematic viscosity) = 5.3×10^5 and angle of attack 5 degrees. This is much smaller than that in [12], many times the core diameter. Yeung and Lee [10] measured wing-tip vortices using PIV technique. In their test, the camera was placed inside the test section, and was protected by Plexiglass casing. The found the extent of core movement, or wandering, to be about 0.1c, which is comparable with the radius of the core itself, at x/c = 10. Obviously, there is great difference among these researchers' data, and further work should be performed on this issue.

In the present paper, some characteristics of the vortex, such as vorticity at the vortex core, effects of angle of attack and Reynolds number on the characteristics of wing-tip vortices will be presented, and effect of wandering on a fixed probe measurement will be discussed in detail based on PIV data.

2. EXPERIMENTAL SETUP DESIGN AND MEASUREMENT CONDITIONS

Experiments were carried out in a closed-loop low speed wind tunnel with a square working section (0.6 m × 0.6 m) of 2.4 m in length. The view window of the working section was made of optic glass in order to maximize the signal-to-noise ratio in PIV measurements. A rectangular airfoil of NACA 0012 wing section with a chord c = 250 mm and a span of 400 mm was used in the experiment. The wing-tip of the airfoil was blunt. The experimental setup was illustrated in Fig. 1. The wing was mounted horizontally on the rear wall of the test section. The angle of attack of the wing was adjustable. A mirror (height × width = 300 mm × 150 mm) was placed downstream of the light sheet plane with a distance about L = 2c, so that the image on the light sheet was rejected out of the wind tunnel and was captured by the CCD camera. The camera was mounted on a traversing mechanism, and can traverse in all 3 dimensions. This made it very convenient to perform the measurements at the near wake of x = 3c. The follows are details of PIV measurements:

A Dantec standard PIV2100 system was used in the measurements. Flow was seeded by smoke, which was generated from Paraffin oil of a particle size around 1 μm in diameter (smoke generator, Teknova, model RG 100). Flow was illuminated in the plane (about 3-5 mm in thickness) perpendicular to the main flow stream by two NewWave standard pulsed laser sources (Nd: YAG lasers) of a wavelength of 532 nm, each having a maximum energy output of 120 mJ and pulse widths of 8 ns at a repetition rate of 10 Hz. Digital particle images were taken using one CCD camera (HiSense type 13, gain × 4, double frames, 1280×1024 pixels). A Dantec FlowMap Processor (PIV2100 type) was used to synchronize image-taking and illumination**.** Each image covered typically a view area of 135 mm × 106 mm.

The cross correlation parameters (such as interrogation area, shift between images, and time between pulses) were chosen as a compromise between the velocity range and the accuracy of the measurement. In the image processing, 32 × 32 rectangular interrogation areas were used. Each interrogation area included 32 pixels with 25% overlap with each other areas in both the horizontal and vertical directions. The ensuing in-plane velocity vector field consisted of 53 × 42 vectors, which gave the same number of vorticity component, ω , which may be approximately obtained based on particle velocities. The horizontal and vertical image magnifications were identical, i.e. 0.1 mm/pixel. The typical spatial resolution for vorticity estimate was about 2.60 mm or 0.01c. Each laser pulse lasted for 0.01μs. The interval between two successive pulses varied from 100 to 20 μs for the main flow velocity varied between 2-15.5 m/s or $\mathrm{Re}_c = 3.4 - 26.6\times10^4$. Thus, a particle would only travel 0.2-0.3 mm (2-3 pixels).

To get the qualitative flow visualisation of the tip vortex, the airfoil was machined with pinholes (0.5 mm in diameter) at its tip. Smoke can be introduced into the hollow airfoil with a

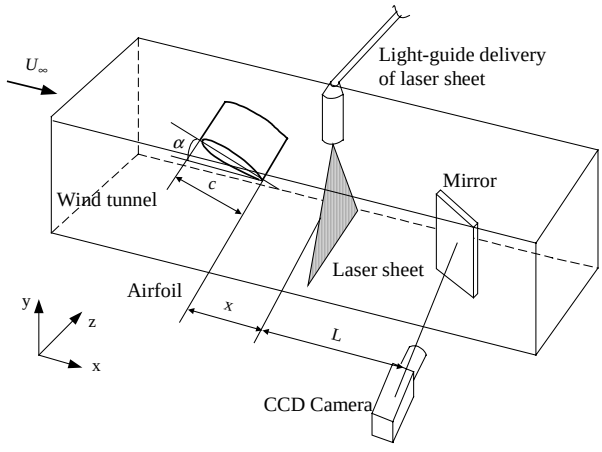

Fig. 1: Sketch of the experimental setup.

hose from another end of it. The tip flow can be traced by the smoke coming out from the pinholes, and be captured based on the flow visualisation function of the PIV system.

As a mirror was located downstream of the measuring plane, the evolution of wing-tip vortices may be influenced. This influence has been checked before measurements. It was found that while L is greater than or equal to $2c$ (refer to Fig. 1), an uncertainty of about 1% will be introduced in terms of the vorticity at vortex core, so the measurements were performed at $L=2c$, and the influence of the mirror can be ignored.

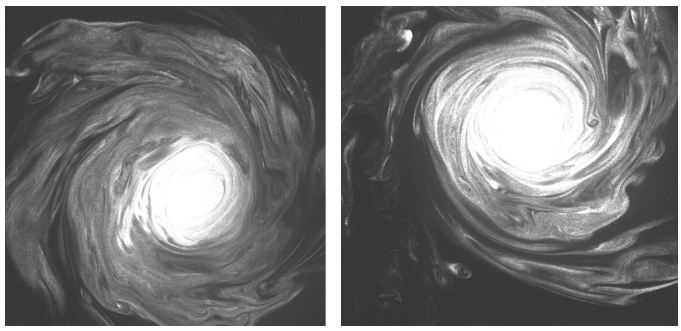

(a) (b)

Fig. 2: Qualitative flow visualization image of the tip vortex at $\mathrm{Re}_c = 7.6\times10^4$. (a) $\alpha = 8°$; (b) $\alpha = 16°$.

3. RESULTS AND DISCUSSIONS

3.1 General Characteristics of Wing-Tip Vortices

Figure 2 shows qualitative photographs of tip vortices at $\alpha = 8°$, and $\alpha = 16°$ at $\mathrm{Re}_c = 7.6\times10^4$. For this NACA 0012 wing, flow separation over the airfoil will occur at $\alpha > 12°$, but it can be found that the longitudinal vortex for $\alpha = 16°$ (Fig. 2b) is still well organized as that of $\alpha = 8°$ (Fig. 2a). In the two photos, some secondary vortex structures are discernable. The small secondary vortices have also been found in the previous works.[10,14] These small secondary vortices have not been captured in velocity vector map (Fig. 3) because of the lack of resolution. The vortex cores show white colour because the seeding smoke intensity is high at this region. The vortex cores appear to be laminar. It should be noted that due to the wandering of wing-tip vortices, the vortex center may not occur at the center of image window. The two images in Fig. 2 were captured at the same plane with the same camera setup, so they show the real relative size of the vortices. It can be found that the size of the vortex at $\alpha = 16°$ is remarkably larger than that of $\alpha = 8°$.

Figure 3 shows typical velocity vector and vorticity contour for $\alpha = 8°$ at $\mathrm{Re}_c = 7.6\times10^4$. In the figures, the origin of the coordinate was defined at vortex center. In Fig. 3a, all the vectors are regular. However, the corresponding vorticity contour in Fig. 3b shows a vortex zone within a range of radius about $0.1c$. This is because that out of this range, derivative secondary vortical structures made the local vorticity increase, and the sign of these secondary vortex may be opposite to the main one. It should be noted that, the values of velocity and vorticity in Figs. 3a and 3b, and the following figures, are normalized by U_∞ and c.

Using a polar-cylindrical coordinate system with the origin at the vortex core center, tangential velocity can be averaged, and plot against radius as shown in Fig. 4. Since a tip vortex will change its shape, vortex center position and strength as it moves to the downstream, using data of one image to character tip vortices will cause relative large error. Therefore, about one hundred images were used in the averaging. The mean tangential velocity was denoted as

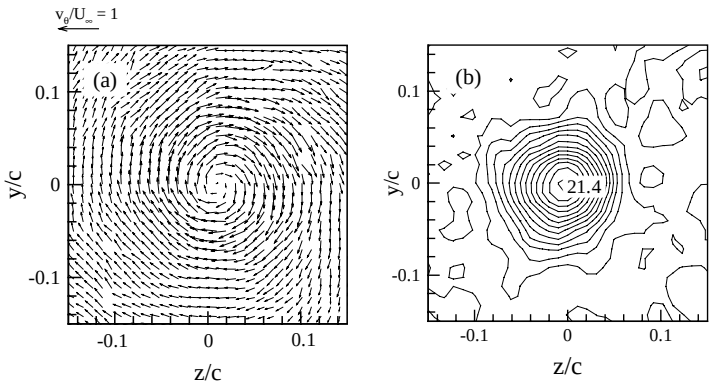

Fig. 3: Velocity vectors and contours of instantaneous streamwise vorticity $\omega c/U_\infty$ for $\alpha = 8°$, at $\mathrm{Re}_c = 7.6\times10^4$. (a) velocity vector; (b) vorticity contour.

$V_\theta^* = \overline{V_\theta} / U_\infty$. Although a real vortex is not fully axisymmetric,[9,10] the averaged data reveal some characteristics of the wing-tip vortex. For $\alpha = 8°$ (Fig. 4a), the maximum tangential velocity $V_{\theta,\max}^*$ occurs at r/c is about 0.05, and for $\alpha = 16°$ (Fig. 4b), this value is about 0.06. In general definition, the radius at which the tangential velocity reaches maximum is the core radius. It can be found that the core radius becomes larger as the angle of attack increases, and it varies slightly with Reynolds number. On the other hand, $V_{\theta,\max}$ increases significantly as α increases from 8° to 16°.

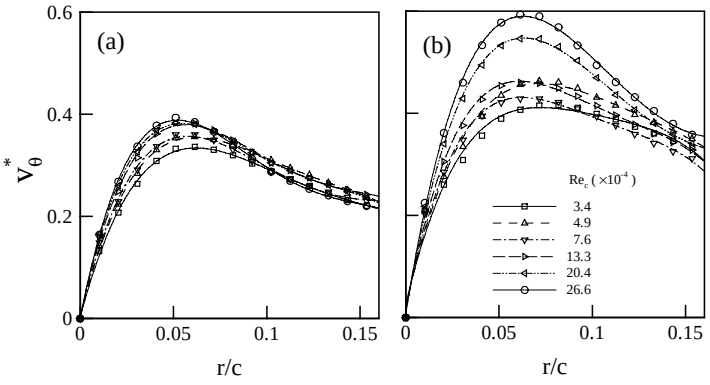

Fig. 4: Circumferentially averaged tangential velocity, $V_\theta^* = \overline{V_\theta} / U_\infty$, at (a) $\alpha = 8°$; (b) $\alpha = 16°$.

Figure 5 presents the maximum vorticity $\omega_{\max}^*$ ($= \overline{\omega}_{\max} \cdot c / U_\infty$) for $\alpha = 8°$ and $\alpha = 16°$. Values of $\omega_{\max}^*$ for $\alpha = 16°$ are much larger than that of $\alpha = 8°$, indicating that vortices become stronger as the angle of attack increases in the test range.

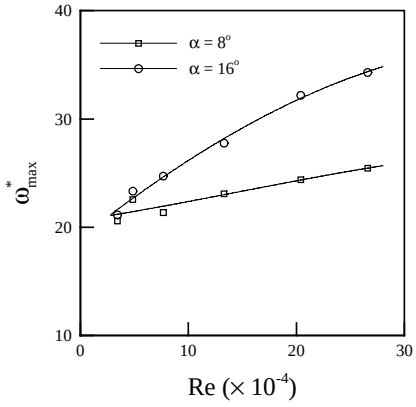

Fig. 5: Maximum vorticity $\omega_{\max}^*$ against Reynolds number, for $\alpha = 8°$ and $\alpha = 16°$.

Reynolds number affects the tip vortex performance. Figure 4 shows that as Reynolds number increases, $V_{\theta,\max}$ increases, but different behavior can be readily observed for $\alpha = 8°$ and $\alpha = 16°$. For $\alpha = 8°$ (Fig. 4a), $V_{\theta,\max}^*$ increases slightly from 0.32 to 0.38 as Re_c increases from 3.4 to 26.6×10^4, the increment is 19%, and at $\alpha = 16°$, this value is much larger, 48% (being increased from 0.4 to 0.59). The increase in $V_{\theta,\max}$ indicates that as Reynolds number increases, the tip vortex structure rotates faster. In Fig. 5, a similar trend is found to the maximum vorticity (or the vorticity at the vortex core) as Reynolds number varies, i.e. the strength of the wing-tip vortex increases while Reynolds number increases. It should be noted that $\omega_{\max}^*$ increases faster for $\alpha = 16°$ than that for $\alpha = 8°$. This is believed to be associated with wing-tip vortex formation distance, and will not be discussed in this paper.

3.2 Wandering

Wandering is observed in wind tunnel measurements of wing-tip vortices. Wandering may be self-induced or a consequence of free-stream unsteadiness.[11] In using PIV to measure tip vortex, images were captured at a fixed coordinate system. Vortex core may occur at different positions for different images due to wandering. The scattering of vortex core location is shown in Fig. 6. There are one hundred points in Fig. 6a and 6b, respectively, each point representing a vortex core center. The origin of coordinates in the figure is the averaged center of all the points. It can be found that at $\alpha = 8°$ (Fig. 6a), points are distributed in a circle of radius about 0.01c, and the distribution is nearly uniform, while, for $\alpha = 16°$ (Fig. 6b), the distribution range becomes larger significantly to about 0.1c, the distribution of the vortex center becomes asymmetric, and the points in the fourth quadrant are clearly less than those in the other three quadrants. Since there is boundary layer separation at $\alpha = 16°$, this difference was conjectured to be associated with the variation of the separation locations, and further investigation of this phenomenon will be performed in our later work.

To quantify the degree of scattering of the tip vortices, we define the distance from a point to the origin of the coordinates as Δr_i, the degree of scattering of the vortex core can be quantified by $\overline{\Delta r} / R_v$, where $\overline{\Delta r} = \frac{1}{N}\sum_{i=0}^{N} \Delta r_i$, R_v is the radius of the tip vortex.

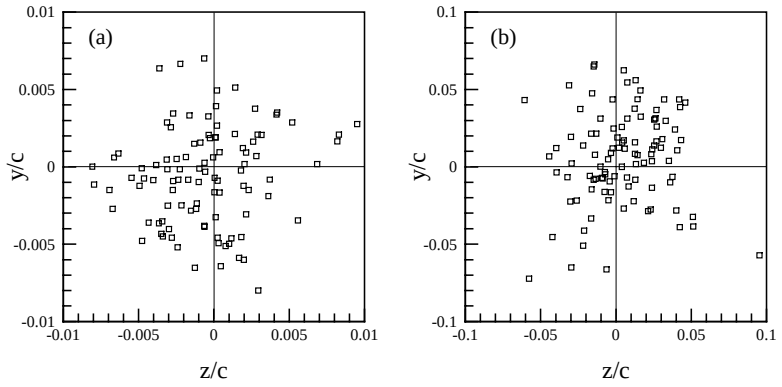

Fig. 6: Maps of vortex centers distributions, at (a) $\alpha = 8°$; (b) $\alpha = 16°$.

Figure 7 shows results of calculations. For $\alpha = 8°$, scattering is very small, $\overline{\Delta r} / R_v$ is about 0.06-0.14. But for $\alpha = 16°$, $\overline{\Delta r} / R_v$ is much larger, from 0.4 to 0.7 depending on Reynolds number. For such a large angle of attack, $\alpha = 16°$, flow separation may occur over the wing. It seems that it is the flow separation that make the flow much unsteady, and leads to a serious wandering of wing-tip vortex.

Devenport et al[11] noted that wandering may lead to error when using a fixed probe to measure the tip vortex. In their study, a method was developed to correct the data, and they found after correction that there is a 12% smaller core radius, 15% greater tangential velocity, and an 11% greater axial velocity deficit. To estimate wandering effect, two averaging methods are adapted in the present data analysis. In the method 1, vortex center in each image was determined firstly, and the origin of the coordinates was defined at the vortex center, all the images, about one hundred in our work, were superimposed in this 'relative coordinates system'. Results in all the above presentations have been obtained by method 1. In method 2, all the images will be superimposed in an absolute coordinates. The origin of this coordinates was at the averaged center of all the points as shown in Fig. 6. In the following, vorticity calculated using these two methods are presented as an example. The maximum vorticity, i.e. vorticity at the vortex center, calculated by method 1 is denoted as $\overline{\omega_{\max}}$, and the vorticity at the nominal vortex center, i.e. origin of the coordinates, in method 2 is denoted as ω_0. The difference between these two values is calculated as $\xi_\omega = (\overline{\omega_{\max}} - \omega_0) / \overline{\omega_{\max}}$. ξ_ω represents wandering effect on the vorticity of vortex center. Figure 8 shows ξ_ω for $\alpha = 8°$ and $\alpha = 16°$. For $\alpha = 8°$, ξ_ω is very small, generally less than 5%. For $\alpha = 16°$, ξ_ω becomes much higher, from 13% to 33% in the whole Reynolds number range. Similarly, wandering effect on the values of peak tangential velocity and vortex circulation has also been examined. There is a 20% smaller in the $V_{\theta,\max}$, while almost no difference between circulations based on the two averaging methods. This is because wandering makes the measuring core vortex smaller than the real one, but while the measured size of vortex become larger than the real one, the overall effect leads to circulation measurement almost not affected by wandering.

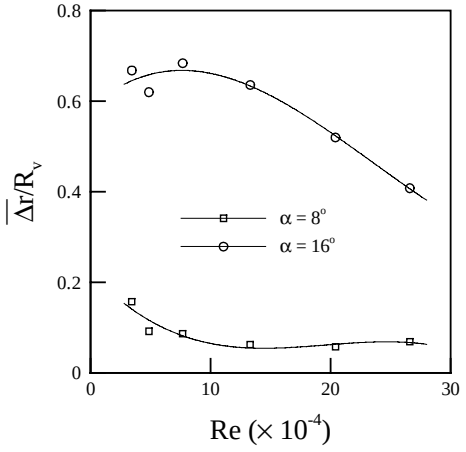

Fig. 7: Mean values of the scattering radius, $\overline{\Delta r} / R_v$ (R_v is the radius of the tip vortex).

4. CONCLUSIONS

The near-field tip vortices (*x/c* = 3) generated by a rectangular NACA 0012 wing model have been investigated based on the PIV measurement. The investigation leads to following conclusions.

(1) The wing tip vortex formation is accelerated as angle of attack, α, increases from 8^o to 16^o. This is linked to the occurrence of flow separation, which does not occur at small α say 8^o but does at large α say 16^o. In general, large α leads to a large tip vortex core, high tangential velocity and large circulation.

(2) As the Reynolds number increases, tip vortices become smaller in the vortex core size, but greater in strength.

(3) Tip vortices occur rather symmetrically about one point in terms of its spatial location and strength for a small α when flow separation is not evident, but become asymmetrical at large α when flow separation occurs. This is believed to be associated with the fact that the boundary layer separation points are wandered along the wing-tip.

(4) Without flow separation such as at $\alpha = 8°$, the scattering of tip vortex location is very small. Once flow separation occurs say at $\alpha = 16°$, the scattering increases markedly. Wandering can lead to about 30% smaller vortex core vorticity, 20% smaller tangential velocity, but do not affect magnitude of vortex circulation.

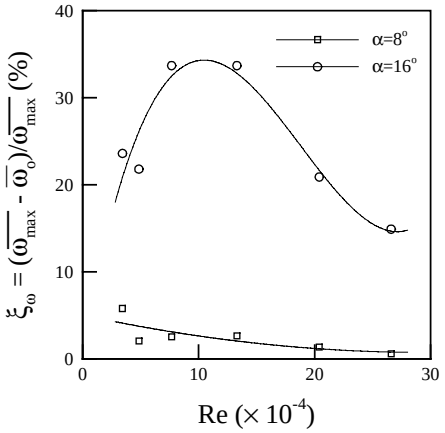

Fig. 8: Difference between the two averaging methods to calculate the mean vortcity at vortex center.

ACKNOWLEDGEMENTS

The authors wish to acknowledge support by the Research Grant of China Institute of Metrology through Grant 59-038.

REFERENCES

[1] Batchelor GK: Axial flow in trailing line vortices, *J Fluid Mech.* 1964, **20**(4), 645-658.
[2] McCormick BW, Tangler JL, and Sherrieb HE: Structure of trailing vortices, *J Aircraft* 1968, **5**(3) 260-267.
[3] Robins ER and Delisi DP: Potential hazard of aircraft wake vortices in ground effect with crosswind, *J. Aircraft* 1993, **30**(2), 201-205.
[4] Spalart PR: Airplane trailing vortices, *Annu. Rev. Fluid Mech.* 1998, **30**, 107-138.
[5] Rossow VJ: Lift-generated vortex wakes of subsonic transport aircraft, *Progress in Aerospace Sciences* 1999, **35**, 507-660.
[6] Liu ZJ, Russell JW, and Sankar LN: A study of rotor tip vortex structure alteration techniques, *J Aircraft* 2001, **38**(3), 473-477.
[7] Chow JS, Zilliac GG, and Bradshaw P: Mean and turbulence measurements in the near field of a wing-tip vortex, *AIAA J* 1997, **35**(10), 1561-1567.
[8] Shekarriz A, Fu TC, Katz J, and Huang TT: Near-field behavior of a tip vortex, *AIAA J* 1993, **31**(1), 112-118.
[9] Dacles-Mariani J, Zilliac GG, Chow JS, and Bradshaw P: Numerical/experimental study of a wing-tip vortex in the near wake. *AIAA J.* 1995, **33**(9), 1561-1568.
[10] Yeung AFK and Lee BHK: Particle imaged velocimetry study of wind-tip vortices, *AIAA J* 1998, **36**(2), 482-484.
[11] Devenport WJ, Rife MC, Liapis SI, and Follin GJ: The structure and development of a wing-tip vortex, *J. Fluid Mech.* 1996, **312**, 67-106.
[12] Corsiglia VR, Schwind RG, and Chigier NA: Rapid scanning, three-dimensional hot-wire anemometer surveys of wing-tip vortices, *J Aircraft* 1973, **10**(2), 752-757.
[13] Baker GR, Barker SJ, Bofah KK, and Saffman PG: Laser anemometer measurements of trailing vortices in water, *J Fluid Mech.* 1974, **65**, 325-336.
[14] Francis TB and Katz J: Observations on the development of a tip vortex on a rectangular hydrofoil, *J Fluids Engineering* 1988, **110**, 208-215.

Proceedings of the Tenth Asian Congress of Fluid Mechanics
17-21 May 2004, Peradeniya, Sri Lanka

A STUDY OF SWIRLER FLOW FIELD CHARACTERISTICS IN A SUDDEN EXPANSION SQUARE CHAMBER USING PIV

A. Panduranga Reddy, N. Jayaprakash, R. I. Sujith and S. R. Chakravarthy
Department of Aerospace Engineering, Indian Institute of Technology – Madras, Chennai – 600 036, India

ABSTRACT: This study investigates the flow field characteristics of a stand-alone swirler in the plane of a sudden expansion into a confined geometry of square cross-section, using particle image velocimetry (PIV). Detailed mean and RMS velocities were obtained at various cross sections downstream of the swirler and in planes along the inlet flow direction. The swirl velocities and the reverse-flow in the central re-circulation zone are observed to be diminishing far downstream of the swirler. The maximum RMS velocity magnitude is observed to be over 60% of the mean velocity at an axial distance of 20 mm downstream of the exit plane of the swirler. The instantaneous velocity vector fields indicate that small-scale structures dominate the region near the swirler, whereas the flow far downstream is characterized by sparsely distributed large-scale vortical structures.

1 INTRODUCTION

Swirling flows occur in a wide range of applications such as vortex amplifiers, cyclone separators, agricultural spray machines, heat exchangers, and jet pumps, and in natural phenomena such as whirlpools and tornadoes. Swirling flows are also created in combustors of gasoline and diesel engines, gas turbines, industrial furnaces, utility boilers, etc., since such flow field helps in flame stabilization and enhanced mixing of fuel and air.

The simplest means of generating a swirling flow is by the use of a vane swirler to induce a tangential velocity component to an otherwise axial flow of an annular round jet. Swirling flows are highly three-dimensional in structure since the centrifugal action of the tangential component induces a large central re-circulation zone (CRZ), besides the re-circulation zones at the periphery of the jet. The flow field is often further complicated by the use of double swirlers that are either co-rotating or counter-rotating, and by use of swirler units that allow radial entry of flow into the chamber.

Fujii et al.[3] and Sislian and Cusworth[12] have experimentally studied the flow field of a free jet, issuing out of a pair of concentric swirlers and a single swirler unit, respectively. Wang et al.[14] have characterized the two-phase flow field included by a dual-swirler and a central air-blast atomizer in a free field. Several others have worked on swirling flows issuing into a confined region. Vu and Gouldin[13] have studied swirling flow surrounded by non-swirling co-flow in a confined duct. Rhode et al.[10] have performed static pressure probe measurements of mean velocity in a flow through a swirler suddenly expanding into a circular duct. Samimy and Langenfeld[11] and Ahmed[1] had the swirler unit located about 50 mm upstream of the sudden expansion. The swirling flow field in a realistically complicated geometry of a gas turbine combustor has been experimentally characterized by Bharani et al.[2] Similar works have also been reported in Mongia et al.[7] The most significant finding from bulk of these reports is that the maximum turbulent intensity ranges from ~36%[11] to ~100%[1], depending upon the level of swirl. This feature has also been highlighted by Mongia et al.[7]

Most of the works mentioned above have adopted the laser Doppler velocimetry (LDV) technique to determine the velocity distribution in the swirl flow field. Notable exceptions are the investigations by Kucukgokoglan and Aroussi[5] and Pruvost et al.[8], which adopt the particle image velocimetry (PIV) technique, the former for flow radially entering the chamber through swirlers in a water tank, and the latter for swirl created by tangential entry of the flow into the duct. Grosjean et al.[4] have reported combined LDV and PIV measurements to utilize the complementary advantages of the two techniques. Whereas LDV offers time-series data, with which unsteady fluctuations can be resolved very well, the planar nature of the PIV technique offers the possibility of resolving typical length scales of turbulent fluctuations more easily.

The present work is performed in the context of the flow field in a gas turbine combustor. The objective of this study is to adopt a simple geometry as much as possible, so that the complexity in the flow field is due primarily to the swirl generated by a single vane swirler rather than by any other aspect of the geometry. This is so that the data generated for such geometry can be used to anchor CFD models based on relatively simplistic Reynolds-averaged Navier-Stokes (RANS) approaches for suitable choice of model-parametric values. Of specific interest is the flow field immediately downstream of the swirler exit plane, so the location of the swirler exit flush with a sudden expansion is important here. Further, the situation in a sector of a gas turbine combustor enclosing a single swirler unit is simulated here by consideration of a test section of square cross-section downstream of the swirler exit.

Two-component PIV is adopted as the diagnostic technique to obtain the velocity vector field in planes along and perpendicular to the axis of the test section. The 2-D PIV technique is difficult to implement for a highly three-dimensional flow field such as that investigated here, since a trade-off is necessitated to obtain appreciable displacement of particles in the given time-interval between two laser pulses and to minimize out-of-plane loss of particles at the same time. The results are, however, quite instructive in that they indicate high levels of turbulent intensity as expected, besides allowing for examination of typical length-scales of vortical structures in the flow field, as mentioned earlier.

2 EXPERIMENTAL DETAILS

The schematic of the test section used in the present study is shown in Fig. 1. The test section has a square cross-section of 120 mm side, and is 500 mm long. The exit of the test section is under ambient conditions. The test section has glass windows for optical access on all four sides; the two side faces are made entirely of glass to allow a light sheet perpendicular to the axis of the test section, whereas, the top and bottom sides have a glass slit of 10 and 15 mm width respectively, which allows light sheet along the axis of the test section. In the former arrangement, the receiving optics is placed downstream of the exit of the test section, and in the latter, the flow field is viewed from one of the side faces. The swirler is fitted to the centre of a square flange of 120 mm side, which is attached to the upstream end of the test section. The swirler has an inner diameter of 32 mm and an outer diameter of 40 mm, and contains 12 vanes inclined at an angle of 50° to the free stream direction. The central portion of the swirler is blocked by a circular disc.

The experimental test facility has provision for supply of compressed air up to 6 bar from three reservoirs with a capacity of 12 m^3 each. Air enters through a settling chamber into a 1.5 m long seamless tube of 50-mm i.d. that leads to the swirler. The tube is fitted with 50 mm-long flow straighteners at its inlet. A glass tube of 50 mm i.d., 2 mm wall thickness, and 100 mm length, is inserted at the other end of the seamless tube. This glass tube section is located 100 mm upstream of the swirler, and is used to measure the inlet velocity, by PIV. Two pressure taps, one at about 50 mm upstream of the swirler, and another on the square flange at the exit plane of the swirler, are connected to two limbs of a U-tube manometer for measurement of the pressure-drop across the swirler. The pressure drop across the swirler is maintained as 0.1 bar throughout the present work. This is about 10% of the static pressure in the test section, which is on the higher side than typical values in combustors, considering that the design pressure drop across an entire combustor is ~5% only. However, the pressure drop of 0.1 bar across the swirler is maintained in order to obtain high velocities in the test section, similar to what is observed in a realistic combustor, considering the low test section pressure and temperature relative to the real case.

A double-pulsed frequency-doubled Nd:YAG laser (532 nm wavelength) is used as a source of illumination for the PIV measurements in the test section. An interline transfer digital CCD camera (Pixelfly model, PCO Imaging make) is used as the receiving optics. It has a resolution of 1360 1024 pixels. Edible oil is used to generate tracer particles of < 1 m size using a seeding arrangement that employs Laskin nozzles. Such size of the seeding particles ensures that they follow the flow very closely.[6] The laser and the camera are synchronized for a pre-programmed delay between a pair of laser pulses and the corresponding pair of shutter exposures of the camera. More than 200 pairs of instantaneous images are obtained for determining ensemble-averaged velocity vectors and the RMS velocity fluctuations. The interrogation area for determining the cross-correlation of the pair of images is

maintained at 64 64 pixels, with an overlap of 50% between adjacent cells. The time interval between the pairs of pulses is varied in the 20-120 s range, depending upon the range of velocities in different regions of the flow field in different parts of the test section, so that the particle displacement obtained is ~4 pixels. A subpixel accuracy of 0.2 pixel can be obtained, which yields an uncertainty in the velocity measurement within ~5%.[9]

3 RESULTS AND DISCUSSION

A fully developed turbulent flow is established as observed at the glass tube section about 100 mm upstream of the swirler, with a centerline ensemble-averaged velocity of 10 m/s under the test conditions mentioned above. The corresponding RMS velocity as a fraction of the mean velocity is 0.10.

The ensemble-averaged velocity vector fields in several cross-sectional planes at different axial locations along the test section are shown in Fig. 2. The contours of the magnitude of the corresponding mean vorticity are superposed over the velocity vector fields. It can be seen that at a location 10 mm downstream of the swirler exit plane, the flow is predominantly inward particularly from the corners, indicating that this location is within the recirculation zone of the jet issuing out the swirler annulus. The tangential component of the velocity is marginal at this location. As opposed to this, a strong swirl flow is observed at 20 mm downstream from the swirler exit, with maximum velocity levels measured to be about 27 m/s at this plane. The locations of the maximum velocity vectors coincide with the openings between the vanes in the swirler. Small re-circulation zones are set up in the regions between the circular swirling region and the square walls of the test section. The 20 mm location also shows the maximum levels of vorticity, that too in regions coinciding with the swirler vane openings. Subsequent near-field locations, such as at 30, 40 (not shown), and 50 mm, exhibit homogenization of the swirl flow field in the azimuthal direction. The velocity vectors further downstream (100-400 mm) show a continuous decay of the swirling flow, as the flow straightens along the axial direction at large distances from the swirler exit.

Fig. 3 shows the velocity vectors and vorticity contours in planes that are perpendicular to the swirler exit plane. The scales of the velocity vectors and the vorticity contours are maintained the same as in the previous figure for ease of comparison. It can be seen in Fig. 3 that a strong jet-like structure is established from the swirler annulus into the sudden-expansion region of the test section, with the central bluff-body region causing a massive flow reversal. The maximum velocity in the jet is slightly lesser in magnitude than that observed for the tangential velocity in the cross-sectional plane at the axial location of 20 mm. This indicates a strong swirl field. The re-circulation zone caused by the annular jet is limited in extent to about 35-40 mm at the corners of the test section. Large cells of re-circulation are set up downstream of the re-attachment point of the jet flow with the test section walls, in view of the flow reversal along the centerline. The CRZ extends quite near to the exit of the test section under these test conditions, commensurate with the strong swirl field that is established.

Turning to the magnitude of the RMS velocity fluctuations obtained at the different cross-sectional planes (Fig. 4), the maximum magnitude is observed in a very small circular region around the swirler exit at the location 10 mm downstream of the exit plane, whereas a thick circular region of highly intense turbulent fluctuations is observed at the 20 mm location. At this plane, where the mean tangential velocities attain maximum values, the turbulent fluctuations also attain maximum values; the maximum turbulent intensity ($\sqrt{\overline{u'^2}+\overline{v'^2}}/\sqrt{\bar{u}^2+\bar{v}^2}$, where the symbols have their usual meanings) is ~63% at this location. This substantial level of turbulence cannot be ignored in numerical models based on the Reynolds-averaging approach, which inherently assumes small levels of turbulent intensity.[7] Subsequent near-field locations (30-50 mm) downstream of this plane show a radially outward spreading and slight decay of the turbulent intensity. At the location 30 mm downstream of the swirler exit, high fluctuation levels are observed in pockets coinciding with the swirler vane openings. The fluctuation magnitudes assume very low values beyond 50 mm downstream of the swirler.

This is supported by the plots of the RMS velocity fluctuations measured in planes perpendicular to the swirler exit, shown in Fig. 5. It can be clearly seen that the maximum fluctuation levels are observed in the region of sudden expansion that separates the corner re-circulation zones and the flow field downstream of the flow re-attachment point.

This raises the question as to whether the turbulence in the flow field is predominantly generated by the swirling action or due to the annular jet entering the sudden expansion region. While the flow is predominantly jet-like immediately downstream (10 mm) of the swirler exit, it acquires high tangential velocity within a very short distance (20 mm) due to the swirling action. The instantaneous velocity field in the cross-sectional plane at 20 mm from the swirler exit (Fig. 6a) shows several small-scale vortical structures sporadically distributed over the cross-section of the test section. By contrast, 1-2 large-scale structures are observed at cross-sectional planes far downstream (Fig. 6b). The instantaneous velocity field observed in the streamwise plane (Fig. 6c) does not indicate predominance of large-scale structures with length-scales of the order of the step height of the sudden expansion in the jet just downstream of the swirler exit. This suggests that the turbulence is predominantly created due to the swirling action rather than due to entrainment of the corner re-circulation zones by the jet from the swirler annulus. The multiple small-scale structures in the near-field of the swirling flow appear to merge into a few large-scale ones farther downstream before decaying out near the exit of the test section.

4 CONCLUSIONS

Two-component PIV has been adopted to measure the mean and RMS velocity in a sudden-expansion geometry with swirl flow. The measurements have been performed at several cross-sectional planes downstream of the swirler, and in planes along the inlet flow direction. The velocity vectors in these orthogonal planes show the relative magnitudes of the tangential and axial velocities attained in the flow field. The RMS velocity fluctuations are significant in magnitude relative to that of the mean velocity, and are predominantly generated by the swirl in the annular jet between the swirler exit and the point of its re-attachment at the walls of the test section.

ACKNOWLEDGEMENT

The authors wish to acknowledge the support of the Gas Turbine Research Establishment, Bangalore, India.

REFERENCES

[1] Ahmed SA: Velocity measurements and turbulence statistics of a confined isothermal swirling flow. *Exp. Therm. Fluid Sci.* 1998, **17**, 256-264.

[2] Bharani S, Singh SN, Agrawal DP: Effect of swirl on the flow characteristics in the outer annulus of a prototype reverse-flow gas turbine combustor. *Exp. Therm. Fluid Sci.* 2001, **25**, 337-347.

[3] Fujii S, Eguchi K, Gomi M: Swirling jets with and without combustion. *AIAA J.* 1981, **19**(11), 1438-1442.

[4] Grosjean N, Graftieaux L, Michard M, Hubner W, Tropea C, Volkert J: Combining LDA and PIV for turbulence measurements in unsteady swirling flows. *Meas. Sci. Tech.* 1997, **8**, 1523-1532.

[5] Kucukgokoglan S and Aroussi A: Isothermal swirling burner flow measurements. PIV'01 Paper 1074, *4th Int. Symp. on Particle Image Velocimetry*, Gottingen, Germany, 17-19 Sep. 2001.

[6] Melling A: Tracer particles and seeding for particle image velocimetry. *Meas. Sci. Tech.* 1997, **8**, 1406-1416.

[7] Mongia HC, Gore JP Grinstein FF, Gutmark EJ, Jeng S-M, McDonell VG, Menon S, Samuelsen GS, Santavicca D, Santoro RJ: Combustion research needs for helping development of next-generation advanced combustors. AIAA Paper 2001-3853, *37th AIAA/ASME/SAE/ASEE Joint Propulsion Conference & Exhibit*, Salt Lake City, UT, 8-11 July 2001.

[8] Pruvost J, Legrand J, Legentilhomme, P, Doubliez L: Particle image velocimetry investigation of the flow-field of a 3D turbulent annular swirling decaying flow induced by means of a tangential inlet. *Exp. in Fluids* 2000, **29**, 291-301.

[9] Raffel M, Willert CE, Kompenhans J: ***Particle Image Velocimetry, A Practical Guide***. NY: Springler, 1998.

[10] Rhode DL, Lilley DG, McLaughlin DK: Mean flowfields in axisymmetric combustor geometries with swirl. *AIAA J.* 1983, **21**(4), 593-600.

[11] Samimy M and Langenfeld CA: Experimental study of isothermal swirling flows in a dump combustor. *AIAA J.* 1988, **26**(12), 1442-1449.

[12] Sislian JP and Cusworth RA: Measurements of mean velocity and turbulent intensities in a free isothermal swirling jet, *AIAA J.* 1986, **24**(2), 303-309.

[13] Vu BT and Gouldin FC: Flow measurements in a model swirl combustor. *AIAA J.* 1982, **20**(5), 642-651.

[14] Wang H, McDonell VG, Sowa WA, Samuelsen S: Experimental study of a model gas turbine combustor swirl cup, part I: Two-phase characterization. *J. Propulsion* 1994, **10**(4), 441-445.

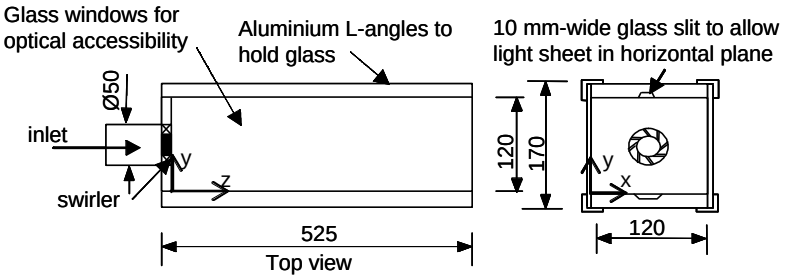

Fig. 1. Schematic of the experimental test section.

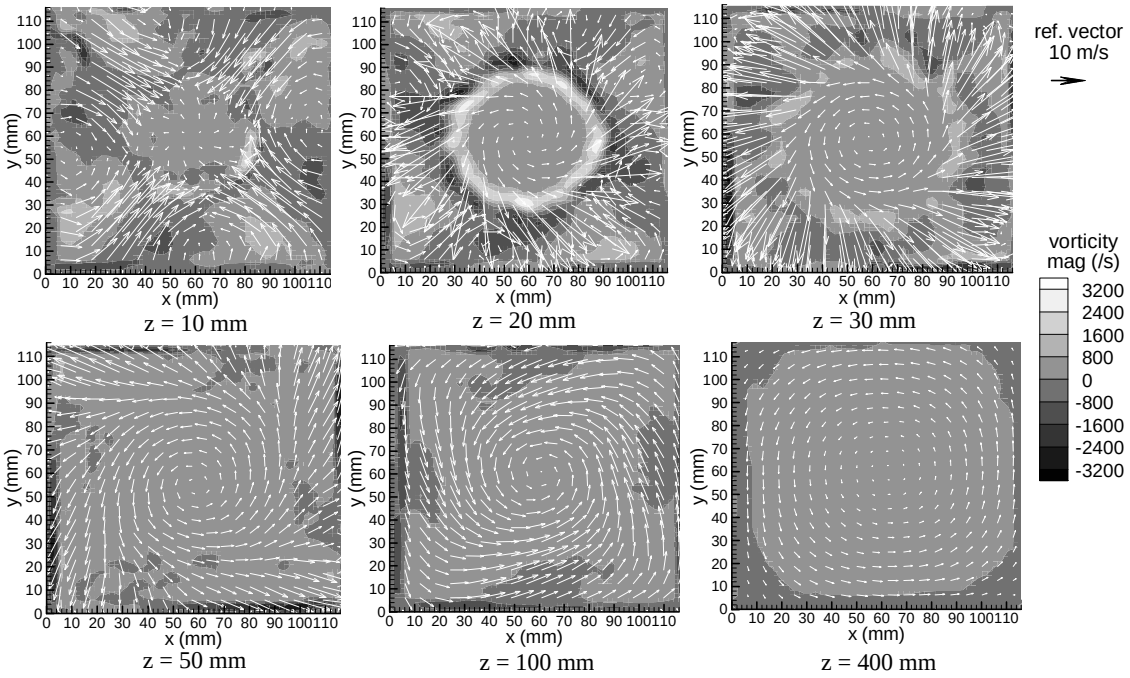

Fig. 2. Mean velocity vector and mean vorticity contour plots in cross-sectional planes at different axial locations from the swirler exit.

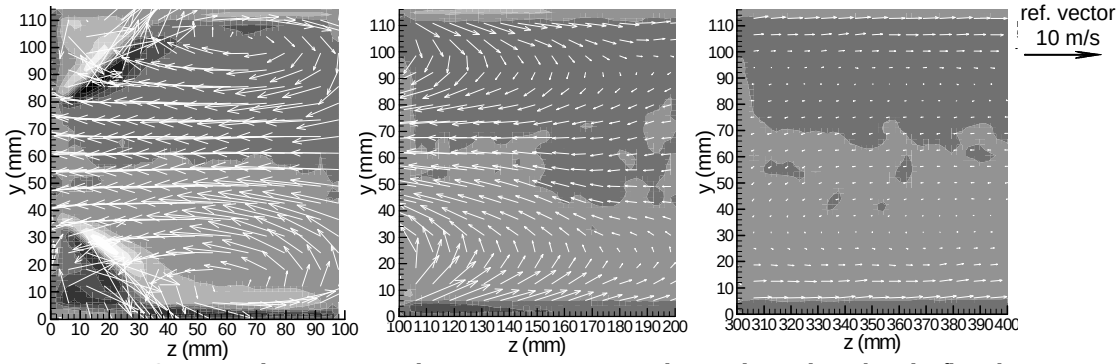

Fig. 3. Mean velocity vector and mean vorticity contour plots in planes along the inlet flow direction.

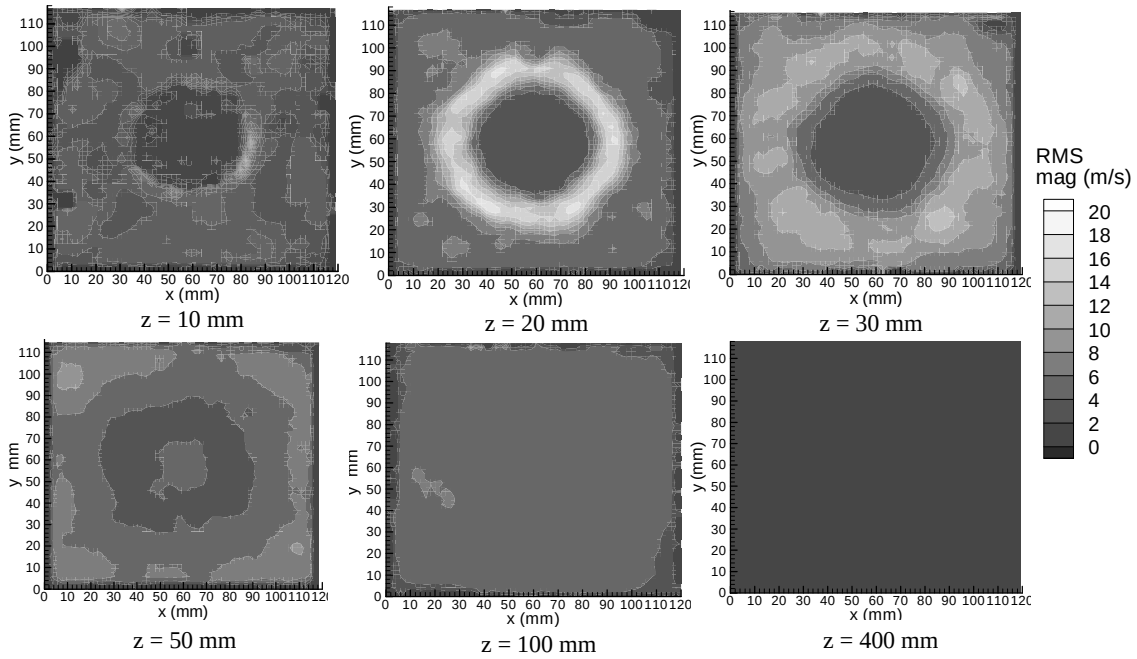

Fig. 4. RMS velocity magnitude contours in cross-sectional planes at various axial locations from the swirler exit.

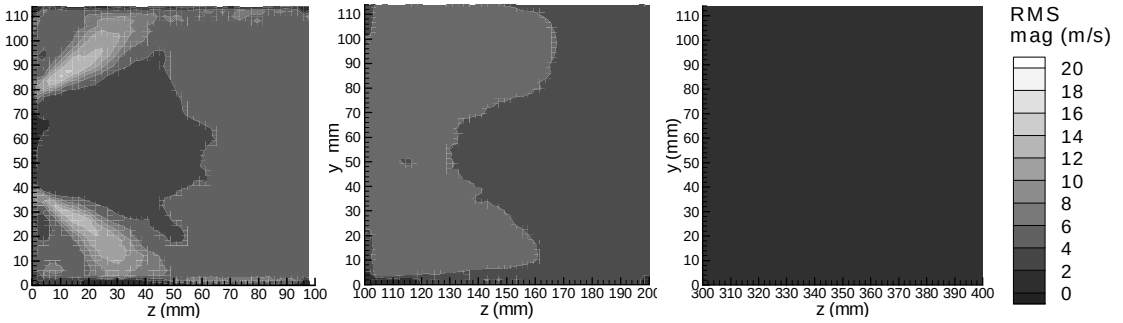

Fig. 5. RMS velocity magnitude contours in planes along the inlet flow direction.

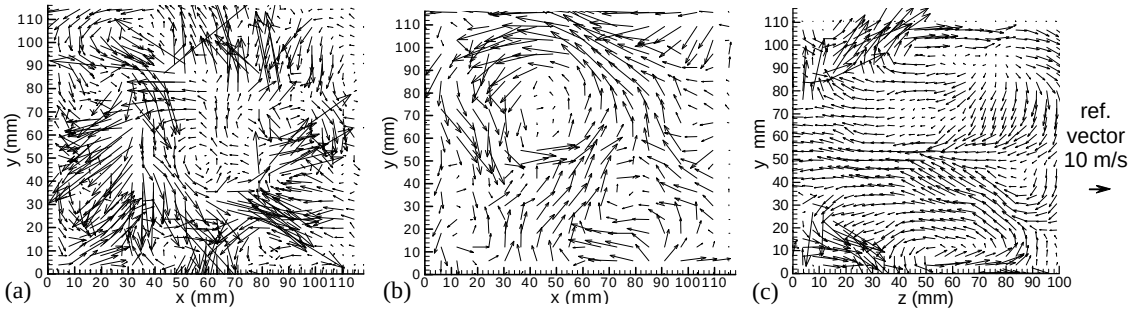

Fig. 6. Instantaneous velocity vectors in cross-sectional planes at 20 mm and 100 mm from the swirler exit (a and b), and in plane along the inlet flow direction (c).

Proceedings of the Tenth Asian Congress of Fluid Mechanics
12-21 May 2004, Peradeniya, Sri Lanka

PROTOPLASMIC STREAMING IN AMEBA

Y. Kokugan and O. Mochizuki
(Department of Mechanical Engineering, Toyo University, Kawagoe 350-8585, Japan)

ABSTRACT Protoplasmic streaming in an ameba is studied experimentally to understand a moving mechanism of mirobes and cells. The motion of the body of an ameba as a micro moving machine and streams of protoplasm as propellant are observed by using a high resolution digital microscope system. The motion of an ameba itself and protoplasmic streaming are recorded by a cooled CCD video camera every 1/30 seconds. The velocity field is obtained by applying a PTV method to the motion pictures. Tracking particles are granular materials that are intrinsic substance in an ameba. The maximum velocity of protoplasmic migrating to a stretching pseudopodium is found to be 4 times larger than that stretching speed of the pseudopodium. The ratio of influx to efflux of some control volumes in an ameba is calculated from the velocity field to check on the local balance of flow rate. It is found that the flow rate at every tested control volume is unbalanced locally.

1. INTRODUCTION

A motion of an ameba crawling over a surface is investigated in order to apply it to a micro soft robot like a white blood cell. It is popular that many cells move by crawling over surfaces rather than by using cilia or flagella to swim. Cell crawling has also a role in many cancers, when cells in a primary tumor invade neighboring tissues and crawl into blood vessels or lymph vessels and are thereby carried to other sites in the body to form metastases. In the molecular biological point of view, the cell locomotion occurs by repeating the cycles consisting of two steps[1]: the leading edge extends forward and stretches actin cortex , then contraction at the rear of the cell propels the body of the cell forward. The actin-rich structures are pushed out at the front of the cell in the protrusion. The myosin II helps to push the cell body forward in the contraction phase. In contrast to the molecular mechanism, when we focus on an ameba as shown in Fig. 1, the micro scale motion of an ameba characterized by

Fig. 1 Ameba. Size is about 300μm.

protoplasmic streaming seems to play an important role to the motion of an ameba itself. Protoplasmic streaming observed in a stretching pseudopodium flows actually faster than the stretching speed of the pseudopodium. We need to consider some peculiar mechanism to biological motion, not normal fluid mechanics.

The purpose of our study is to understand a micro scale moving mechanism of mirobes and cells, because we try to apply the motion of an ameba to a micro moving machine. The important specification to design the micro moving machine is the propellant. Therefore, we investigate the motion of an ameba and flow field inside its body as the first step. A relation between the motion of an ameba itself and protoplasmic streaming is discussed in this paper.

2. EXPERIMENTAL EQUIPMENTS AND METHODS

The motion of the body of an ameba and streams of protoplasm are observed by using a high resolution digital microscope system shown in Fig. 2. The microscope is magnification of 1,000. Pictures are recorded every 1/30 seconds by the CCD camera of this system that is cooled by a Pertier module to increase sensitivity. The velocity field is obtained by applying a PTV method to the motion pictures. Tracking particles are granular materials that are intrinsic substance in an ameba, being easily distinguished by small dots as seen in Fig. 1. The average diameter of granular materials is 1.5 μm. The velocity is calculated by the moving distance of the granular material in 1/30 seconds. Ratios of influx to efflux of distinctive parts in an ameba are estimated by velocity distributions.

Fig.2 High resolution Digital Micro Scope.

Amebas are bred in an incubator under a constant temperature 20 ℃. Medium is KCM solution. Since the body of an ameba is a three-dimensional structure, it is flattened between a prepared specimen and cover grass for flow visualization and PTV measurement.

3. RESULTS AND DISCUSSIONS

The motion and deformation of an ameba in 1 minute is shown in Fig. 3. Protrusions like fingers are pseudopodia. Small granular materials move in an ameba. Since these materials move into a stretching pseudopodium, we suppose that protoplasm migrates into the pseudopodium if these motion coincide with protoplasmic stream. When a pseudopodium lengthen, protoplasm flow into the pseudopodium, and vice versa. The direction of stream in a pseudopodium changes quickly as if the

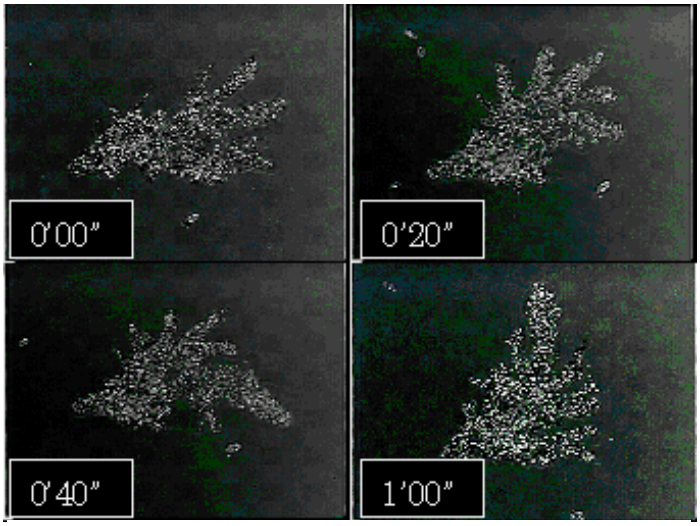

Fig. 3 Motion of ameba in a minute.

inertia force were not dominant at all because of Re = $O(10^{-2})$. The merging of the different streams coming from the different shrinking pseudopodia is observed. The branching away of the main stream is also observed in the body of an ameba. At this stage, it is not clear that whether pseudopodium moves due to protoplasmic stream or whether protoplasm flows due to stretching or shrinking of a pseudopodium.

The velocity field obtained by the microscopic visualization and PTV method is shown in Fig. 4. Instantaneous major inflow and outflow of finite regions numbered 1, 2 and 3 are estimated by the flow field, which are presented by thick arrows in Fig. 4. There are three inflows and two outflows in the region 1. Two streams merge and one stream flows away in the region 2. One stream flows away from the region 3. The influx and efflux of each region are calculated from the velocity field to check on the local balance of the flow rate. It is obvious that the flow rate at all tested regions is unbalanced as shown in Fig.5. The reason is not clear yet because we just only observed the motion of granular materials not the protoplasmic flow itself. We try to observe the protoplasmic flow by several staining techniques in next stage.

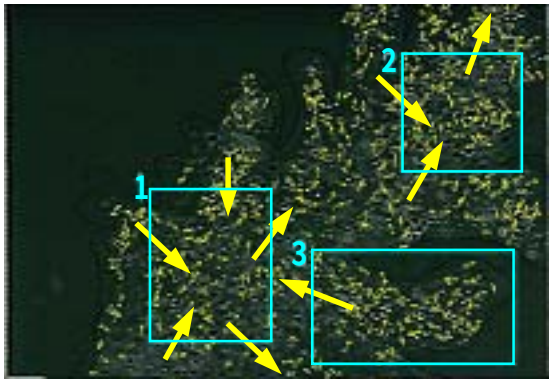

Fig. 4 Instantaneous velocity field in ameba. Box is control volume and thick arrow shows the flow direction to control volume.

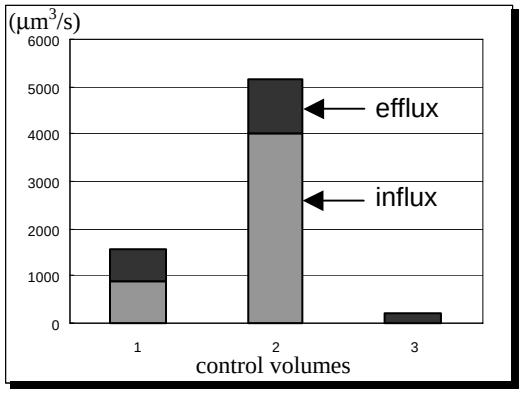

Fig. 5 Flow rate balance of control volumes numbered 1,2,3 in Fig. 4.

The instantaneous velocity profile is obtained at the A-A section in a pseudopodium traced from the magnified picture as shown in Fig. 6. The width at the section of the pseudopodium is 30 μm. The velocity near the center position is faster than that beside the center as seen in Fig. 7. The broken line shows the parabolic curve. The distance between the points that the curve intersects the y-axis shows the width of sol stream, being 8μm in this case. We consider that the sol reached at the leading edge of the pseudopodium is converted into gel stacked against the side wall as sketched in Fig. 6 when the pseudopodium stretches. Then, the ratio of width of gel layer to sol layer is 3.75. The maximum velocity of protoplasmic migrating to a stretching pseudopodium is found to be 4 times larger than that stretching speed of the pseudopodium. Therefore, if the mass is conserved and the velocity profile is parabolic as sketched in Fig. 7, the width ratio of gel and sol layers is calculated by 3.70. This value coincide with that estimated by the velocity profile as above mentioned. This means that the velocity of a protoplasmic streaming is correlated with the moving speed of an ameba.

4. CONCLUSIONS

The relation between the micro motion of an ameba and protoplasmic streaming is investigated by using a micro scope and micro flow visualization. It is interesting that the flow rates of influx and efflux at several regions in ameba is unbalanced locally. The velocity ratio of protoplasmic streaming into a stretching pseudopodium to stretching speed of the pseudopodium is the result of mass conservation.

REFERENCES

[1] B. Alberts, et. al., Molecular biology of The Cell, fourth edition, Grand Science, 972, 2002.

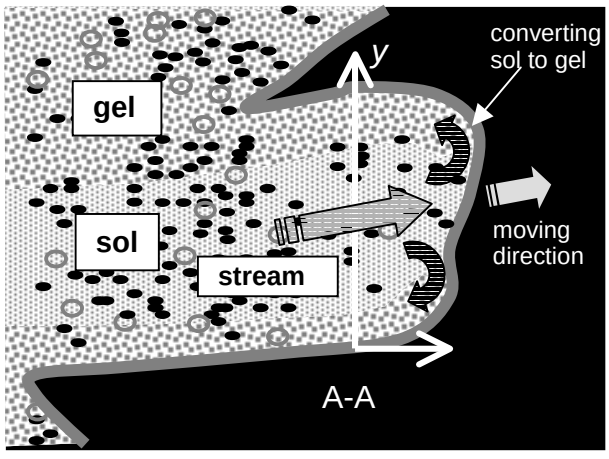

Fig. 6 Image of protoplasmic stream and motion of pseudopodium. This figure is traced from a picture.

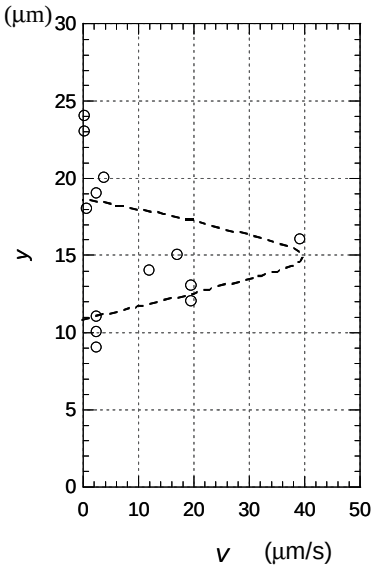

Fig. 7 Velocity profile at A-A line shown in Fig. 6.

PROCEEDINGS OF THE TENTH ASIAN CONGRESS OF FLUID MECHANICS
17-21 MAY 2004, PERADENIYA, SRI LANKA

COMBUSTION OSCILLATIONS IN ROUND SUDDEN EXPANSIONS WITH A STRATIFIED PREMIXED UPSTREAM FLOW

D Luff, JH Whitelaw
Department of Mechanical Engineering, Imperial College of Science Technology and Medicine,
London SW7 2BX, United Kingdom

S. Sivasegaram
Faculty of Engineering, University of Peradeniya, Peradeniya, Sri Lanka

ABSTRACT: The paper presents an experimental investigation of combustion oscillations in a round sudden expansion flow with an area expansion ratio of 2.5 with a stratified mixture of fuel and air provided by a coaxial duct arrangement upstream of the step, with methane, propane and ethylene as fuels, and equivalence ratios in the core and annular flow in the upstream duct as variables. The uneven composition of the fuel-air mixture led to larger amplitudes of pressure oscillation than in uniformly premixed flows. Cycles of local extinction and reignition, caused by large instantaneous strain rates, led to large amplitudes of oscillation at low equivalence ratios and important modulation of acoustic oscillations at higher equivalence ratios. Methods to control the oscillations were examined and were hampered by the large amplitudes, the broadband nature of those due to extinction and reignition and by the modulation of the acoustic oscillations.

1. INTRODUCTION

Pressure oscillations in premixed flames in round sudden expansion flows have been examined over a wide range of area expansion ratios and for different exit boundary conditions [1-4]. Although they could be dominated by a circumferential, radial, longitudinal or bulk mode (Helmholz) frequency of the combustor, the emphasis of studies of the oscillations and their control has been on the last two, since they are more difficult to avoid. Rough combustion, characterised by large amplitudes of pressure oscillation, tends to be dominated by a longitudinal frequency in ducts without an exit nozzle, and constriction of the exit with a nozzle generally gives rise to a bulk mode frequency.

The dominant longitudinal frequency in ducts without an exit nozzle depends on the area ratio of the sudden expansion: with area ratio greater than 3, oscillations are dominated by the ¼-wave frequency of the duct downstream of the step, and smaller ratios give rise to a longitudinal frequency of the entire duct. Larger area ratios lead to larger amplitudes of pressure oscillation due to shorter flames and a greater intensity of heat release in the vicinity of the step. The amplitude also depends on the ratio of the duct lengths on either side of the step, and is largest when the longitudinal acoustic wave in the entire duct had a pressure antinode near the step [3].

Studies of control of combustion oscillations showed that active control by imposing oscillations on the flow at the dominant frequency of the naturally occurring oscillation, but out of phase with it, was highly effective in sudden expansions with area ratio grater than three [5] but less so with smaller area ratios [6,7]. The difficulty related mainly to the pressure oscillations having a modulated wave-form. Strongly modulated wave-forms have been observed close to the extinction limit due to cycles of local extinction and reignition, causing a variation in the position of the flame at a frequency of order 10 Hz compared with acoustic frequency values a periodic of order 100 Hz [8].

Combustion oscillations and their control in sudden expansions with moderate area ratio have in recent years been studied in detail because of their importance to gas turbine combustors. Also, since most of the earlier studies were with methane as fuel and since gas turbines burn heavier hydrocarbons with higher flame speed [9,10], the study has recently been extended to include fuel as an additional variable [11,12]. It was found that the oscillations were fuel dependent to the extent that the fuels had different flame speeds: for example, flames with ethylene, with a higher flame speed than methane and propane, attached close to the step, and tended to move upstream of the step following onset of rough

combustion. The consequent excitation of the longitudinal frequency of the upstream duct led to competition between this frequency and the dominant frequency associated with the entire duct and to a reduction in the amplitude of pressure oscillations.

Earlier studies [13] have also shown that unpremixedness, i.e. uneven composition of the fuel-air mixture, led to higher amplitudes of oscillation than in uniformly premixed flows with the same overall equivalence ratio (ϕ = the fuel to air ratio expressed as a fraction of the stoichiometric fuel to air ratio), and, since the fuel-air mixture in practical gas turbine combustors is of non-uniform composition, the implications of unpremixedness are important to the control of oscillations in practical combustors.

Thus, the purpose of the present study is to examine the importance of fuel and unpremixedness to oscillations in sudden expansion flows with a moderate area expansion ratio. Unpremixedness of different degrees was introduced by a stratified flow arrangement with a rich air-fuel mixture at the core surrounded by a leaner fuel-air mixture, in a coaxial upstream duct arrangement. Tests were also carried out with the core flow leaner than that around it.

The amplitude of pressure oscillations and the modulation in amplitude, in view of its importance to the effectiveness of active control, have been quantified with the equivalence ratios in the core and the annulus as variables for three different fuels, namely methane propane and ethylene. The paper presents the results and their implications, and includes the findings of some tests to impose active control on the naturally occurring pressure oscillations.

2. THE FLOW ARRANGEMENT AND INSTRUMENTATION

The flow arrangement (Figure 1) comprised an upstream duct of inner diameter 50 mm with a coaxial thin-walled core duct of internal diameter 33 mm and outer diameter 35 mm, and joined at a step to a duct of internal diameter 80 mm. The ducts were constructed in modules to allow variation of their lengths and of the axial distance between the end of the core pipe and the step so that the fuel concentration profile could also be varied. The present study was carried out with the duct dimensions of Figure 1, which were similar to those in the earlier studies of [6,7,11,12], but for the core duct. The duct lengths ensured that an antinode of the ¾-wave in the whole duct was close to step and gave rise to large amplitudes of pressure oscillation during rough combustion. The core pipe was truncated 50 mm upstream of the step and sharpened to a knife-edge, so that the wake effect behind the duct and the risk of flame attachment on the end of the duct were minimised.

The fuel (94% pure methane, 96% pure propane and 99.9% pure ethylene) and air in the core flow were premixed in the swirl register, with swirl removed subsequently by a honeycomb flow straightener and wire mesh screens. Fuel and air in the annular flow were mixed by impingement of closely located radial jets of fuel and the air, and wire mesh screens enhanced mixing and rendered the flow uniform. A pair of acoustic drivers was located close to the upstream end to impose pressure oscillations on the flow.

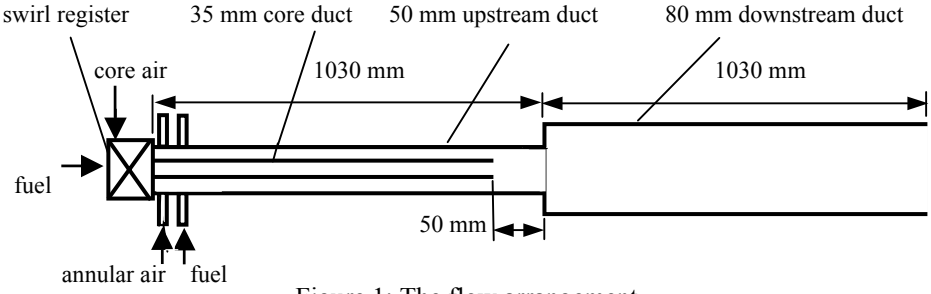

Figure 1: The flow arrangement

All flows were metered to a precision of around 1% with calibrated float-type flow meters (Rotameter-KDG Instruments) with readings corrected for density variation by monitoring the pressure and temperature of the fluid at the flow meter exit. Pressure oscillations were measured using a pressure transducer (Kistler 6121 with charge amplifier 5007) mounted flush with the inner wall of the upstream

duct 70 mm upstream of the step, and the signal transmitted via an interface (National Instruments DAQ BNC-2090 and PCI MIO 16E4 A/D card) to a computer for acquisition (LabView software). Eight seconds of pressure signal data were acquired at 4096 Hz for each condition and post-processed using custom-written software (C++ and Excel VBA) to provide the rms amplitude of fluctuation and the modulation of amplitude to a resolution of 10 Pa, and the power spectrum to a resolution of 1 Hz.

Active control was examined for a selection of flow conditions by imposing pressure oscillations with the acoustic drivers (Naigara NAS-813-22). The active feedback system comprised a band-pass filter (Krohn-Hite 3202), from 160 to 180 Hz to filter out the dominant frequency of around 170 Hz, and a custom-built phase shifter to provide an input to the acoustic drivers through a custom-built stereo amplifier to ensure constructive interference.

3. RESULTS

Tests were carried out with nearly equal bulk flow rates in the core and the annulus so that the mean velocities were similar in the core and the annulus. The influence of Reynolds number on flammability and stability limits and amplitude of oscillation for uniformly premixed flames has been quantified earlier [12] and, on that basis, extensive measurements were done at a Reynolds number of 62 000 based on a bulk mean velocity of 18 m/s, the duct diameter, and fluid properties immediately upstream of the step.

The lean flammability limit depended mainly on the equivalence ratio of the annular flow, and was highest for methane at around 0.6 in the annulus and lowest for ethylene at around 0.4. The influence of the equivalence ratio of the core flow was a decrease in the lean limit with increase in the equivalence ratio in the core flow from zero to greater than unity. Transition to rough combustion, marked by a sharp increase in rms pressure fluctuation from under 0.5 kPa to over 2 kPa, depended on the overall equivalence ratio, at around 0.85 for methane, 0.8 for propane and 0.7 for ethylene.

Figure 2 shows the influence of the equivalence ratio in the core and the annulus on the rms pressure fluctuation (p') for the three fuels. Ethylene gave rise to larger amplitudes than propane because the flame attached closer to the step owing to the higher flame speed. However, in all cases, for a given overall equivalence ratio (approximately the average of the values in the core and the annulus), the amplitude increased as the annular flow became leaner. This is consistent with the earlier observations of [13] that unpremixedness led to an increase in amplitude of oscillations. However, with the core flow very lean, the amplitude was reduced to levels observed in smooth combustion. This effect is similar to that of a central jet of air on combustion oscillations in an otherwise uniformly premixed flow [14]: the oscillations were attenuated by the quenching of heat release by the central jet when the heat release was at its maximum with the flame closest to the axis of the duct.

With a large difference between the core and annular equivalence ratio, methane flames tended to blow off with rms pressure oscillation increasing above 4 kPa, while the amplitudes of propane and ethylene showed a sharp decline after reaching a peak value between 3 and 5 kPa for propane and between 3 and 7 kPa for ethylene. The decline in amplitude for ethylene with a rich annular flow (ϕ>0.8), as found in earlier studies with uniformly premixed flows, seems to be due to the excitation of the upstream quarter-wave frequency [12], and in other cases it appears that large amplitude of oscillation caused the flame to detach from the step and stabilise some distance downstream of the step rather than blow off. The tendency for the flame to blow off following the onset of oscillations of large amplitude is known to increase with decease in expansion ratio, owing to poorer flame stabilisation [3,4], and the larger amplitudes of pressure oscillation than in uniformly premixed flows lead to larger instantaneous strain rates and therefore a greater susceptibility to blow off. Flame speeds for ethylene and propane are, respectively, twice and 1.3 times that for methane so that flames with ethylene and propane are more robust than methane flames.

Typical power spectra in oscillations of large amplitude for the three fuels (Figure 3) show the upstream ¼-wave frequency in addition to the dominant ¾-wave in the whole duct, but with a tenth of the amplitude of the dominant frequency. More importantly, the dominant frequency did not show a well-defined sharp peak in the spectrum. The spread in the frequency suggests a variation in the frequency value caused by periodic shift in the flame position [6].

The selection of pressure traces in Figure 4 show that, even for moderate amplitudes of oscillation, the pressure signal has the form of a modulated wave. Causes for such modulation have been identified as competition between rival frequencies for domination of the oscillations [15], variation in flame position due to low frequency oscillation of the bulk flow [6], and cycles of extinction and reignition [16,17]. The power spectra do not point to rival frequencies and the modulation is too uneven to be due to a low frequency oscillation of the bulk flow. Also, the extent of the modulation, shown superimposed on the pressure traces is far more than in uniformly premixed flows with comparable flow conditions.

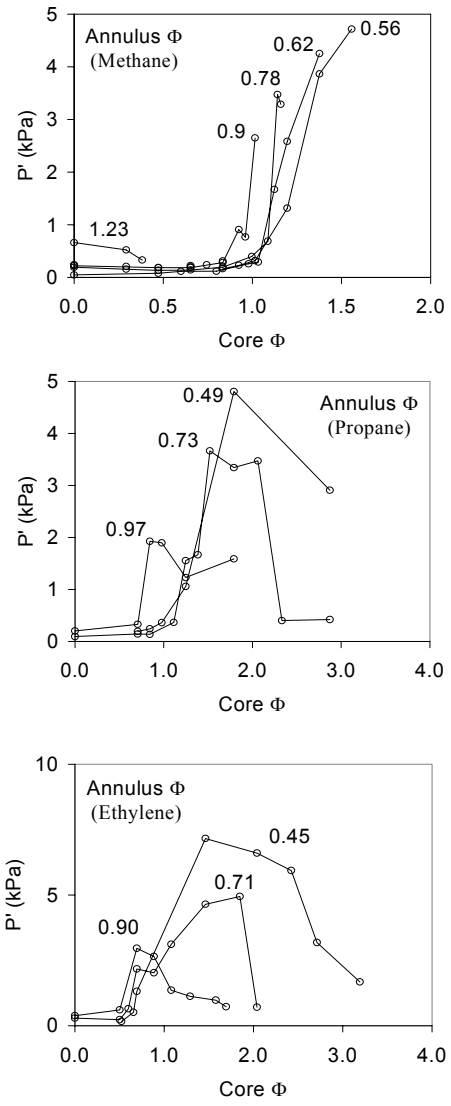

Figure 2: Variation of rms pressure oscillati with equivalence ratio

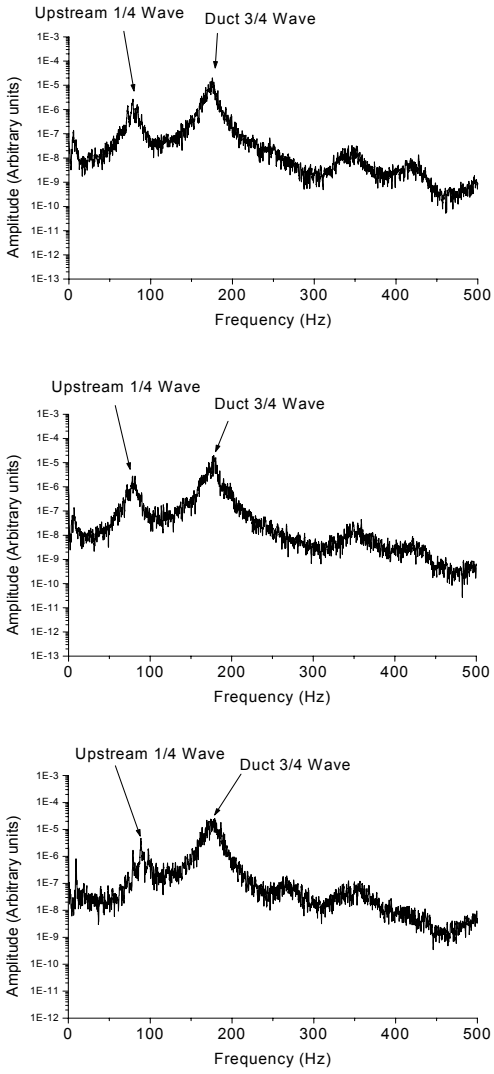

Figure 3: Typical power spectra for (top to bottom) methane, propane and ethylene for oscillations of large amplitude

Cycles of extinction and reignition with a strongly modulated wave-form have been observed in the vicinity of the extinction limit [17]. The extent of modulation in Figure 4 is larger and comparable with the variation in amplitude in the bulk mode oscillations in ducts with an exit nozzle [4], with intermittency at frequency less than 5 Hz, and considered to be due to poor flame stabilisation. The

modulation although not regular, is periodic to the extent that it is identifiable in the pressure spectra as a broadband low frequency, increasing from around 6 Hz for methane to 8 Hz for propane and 12 Hz for ethylene. The dependence of this frequency on the fuel points to the existence of extinction and reignition cycles as observed close to the lean flammability limit, and the correlation between the frequencies and the flame speeds for the fuels suggests that the period of the extinction cycle depends strongly on the time taken by the relit flame to return it its initial position close to the step.

Active control by pressure oscillations with a phase difference was examined for a limited range of flow conditions and with methane as fuel. Control was effective only for equivalence ratios close to transition to rough combustion. With larger amplitudes and modulation in amplitude, active control was hampered by the broadband nature of the extinction and reignition cycles.

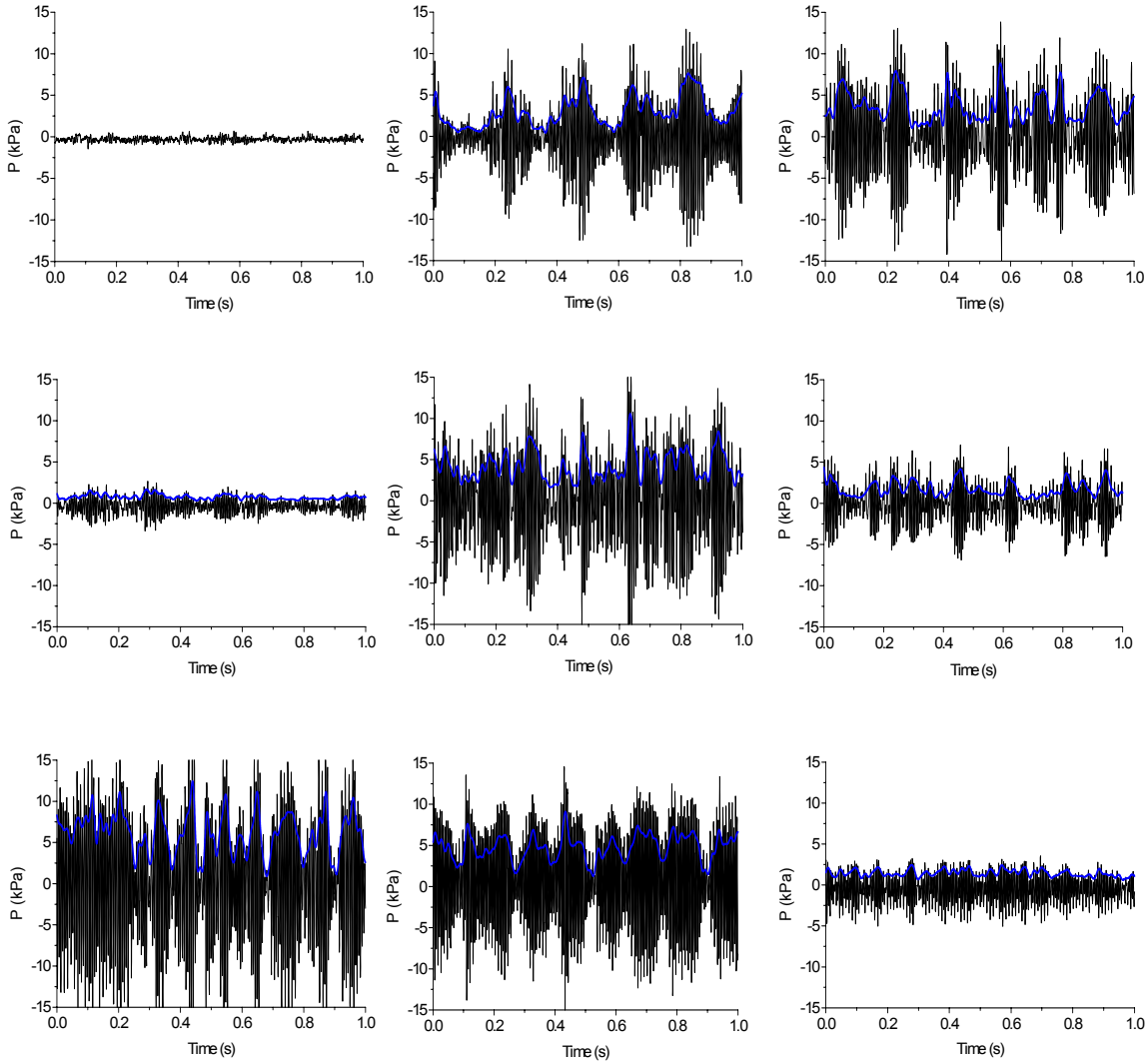

Figure 4: Typical pressure signals: top - methane, middle - propane, bottom –ethylene
Equivalence ratios from left to right: methane (Φannulus = 0.56, Φ core = 1.01, 1.38, 1.56), propane (Φ annulus = 0.49, Φ core = 1.25, 1.79, 2.87), and ethylene (Φannulus = 0.45, Φ core = 1.47, 2.43, 3.20)

4. CONCLUDING REMARKS

Unpremixedness in the flow upstream of the sudden expansion led to higher amplitudes, greater proneness to extinction and therefore cycles of extinction and reignition that led to a large modulation in pressure oscillations and a greater tendency of the flame to blow off.

The higher amplitudes observed in the present flows than in corresponding flows with uniform premixing of fuel and the large modulation in pressure oscillations appear to be due to cycles of extinction and reignition.

Although proneness to extinction with increase in amplitude of pressure oscillation was less with ethylene, with a higher flame speed, than for propane and methane, all fuels were subject to modulation in the pressure oscillations. This has important implications for control of pressure oscillations in gas turbine combustors with a considerable degree of unpremixedness. Active control is likely to be ineffective due to the combination of large amplitude of oscillations and a large modulation in amplitude at a broadband low frequency caused by cycles of extinction and reignition.

Under the circumstances, active control, even with a large oscillated input in the form of pulsed fuel injection, may be ineffective due to its inability to deal with broadband oscillations. An alternative could be passive control by imposing oscillations at an alternative frequency [15,18]. This method has the advantage of being independent of the phase of the pressure oscillation and insensitive to the uncertainty in the value of the dominant frequency. Other possibilities include the reinforcement of flame stability by adding swirl [4,19] or by the addition of fuel to the shear layer [7,12]. The former is subject to considerations of the effects of swirl on the flow distribution and the risk of flashback, while the latter is effective only over a limited range of flow conditions and injection rates.

ACKNOWLEDGMENTS

The research was carried out with financial support from the US Office of Naval Research under grant N000014-02-1-0664. Advice and practical assistance from Dr GD Roy and useful discussions with Drs SRN De Zilwa and I Emiris are gratefully acknowledged.

REFERENCES

[1] Putnam AA. **Combustion Driven Oscillations in Industry**, American Elsevier Publishing Co. 1971

[2] Crump JE, Schadow KC, Bloomshield FS, Culick FEC, Yang V. Combustion instability in dump combustors: acoustic mode determinations, *Proc. 19th JANNAF Combustion Meeting*, CPIA Publication 366

[3] Sivasegaram S, Whitelaw JH. Oscillations in axisymmetric dump combustors, *Comb. Sci. Technol.* 1987, **52**, 423-426

[4] Sivasegaram S, Whitelaw JH. Combustion oscillations in dump combustors with a constricted exit, *Proc. IMechE* 1988, **C 202**, 205-210

[5] Sivasegaram S, Tsai RF, Whitelaw JH. Control of combustion oscillations by forced oscillation of part of the fuel, *Comb. Sci. Technol.* 1995, **52**, 423-426

[6] De Zilwa SRN, Sivasegaram S, Whitelaw JH. Control of combustion oscillations close to stoichiometry, *Flow, Turbulence, Combustion* 1999, **63**, 395-414

[7] Emiris I, Whitelaw JH. Control of premixed ducted flames from lean limit to stoichiometry, *Comb. Sci. Technol.* 2003, **175**, 1-28

[8] SRN De Zilwa, I Emiris, JH Uhm & JH Whitelaw (2001) Combustion of premixed air and methane in ducts, *Proceedings of the Royal Society London* **A 457**, 1915-1949

[9] Warnatz J. Chemistry of high temperature combustion of alkanes up to octane, *Proc. 20th Symp. (Int.) on Combustion*, 845-856

[10] Egolfopoulos, FN, Dimotakis, PE. A comparative numerical study of premixed and non-premixed ethylene flames, *Comb. Sci. Technol.* 2001, **162**, 19-35

[11] Korusoy E, Whitelaw JH. Effects of wall temperature and gas on ducted premixed flames, Proc. 19th Int. Colloq. Dynamics of Explosions and Reactive Systems, Hakone, Japan, 2003

[12] Emiris I, Korusoy E Sivasegaram S, Whitelaw JH. (2003) Control of ducted flames by combinations of imposed oscillation and added fuel, *Proceedings of the International Colloquium on Combustion and Noise Control*, Cranfield, UK, August 2003, Paper A1

[13] Bhidayasiri R, Sivasegaram S, Whitelaw JH. Control of oscillations in premixed gas turbine combustors, **Advances in Chemical Propulsion: Science to Technology** (ed. GD Roy), CRC Press, 2002, 303-322.

[14] Emiris I. PhD Thesis, University of London, 1992
[15] Sivasegaram S, Whitelaw JH. Active control of combustion oscillations in combustors with several frequency modes, **Active Control of Noise and Vibration, ASME DSC-38**, 1992, 69-74
[16] Sardi E, AMKP Taylor AMKP, Whitelaw JH. Extinction of turbulent counterflow flames under periodic strain, *Comb. Flame* 2000, **113**, 13-26
[17] De Zilwa SRN, Uhm JH, Whitelaw JH. Combustion oscillations close to the lean flammability limit, *Comb. Flame* 2001, **86**, 347-358
[18] Wilson K, Gutmark E, Schadow KC. Flame kernel pulse actuator for active combustion control, **Active Control of Noise and Vibration, ASME DSC-38**, 1992, 75-81
[19] S Sivasegaram S, Whitelaw JH. The influence of swirl on oscillations in ducted premixed flames, *Comb. Flame* 1991, **85**, 195-205

Proceedings of the Tenth Asian Congress of Fluid Mechanics
17-21 May 2004, Peradeniya, Sri Lanka

COLLAPSE AND GROWTH OF CAVITY REGION AND NETWORK FORMATION IN A GRANULAR MATERIAL DUE TO VISCOUS FLUID

O. Sano and Y.Kaneko,
Department of Applied Physics, Tokyo University
of Agriculture and Technology, Koganei, Tokyo 184-8588, Japan

Y.Nagata
VBL, Tokyo University of Agriculture and Technology, Koganei, Tokyo 184-8588, Japan

ABSTRACT: Experimental and numerical studies on the flow-induced collapse of a cavity region in an otherwise homogeneous granular material are made. We have already shown a great influence of the presence of macroscopic void spaces on the flow field and the volume flux into the latter. Conversely the enhanced viscous stress has greater possibility to destroy the cavity boundary in the local scale, which leads to global deformation and/or migration of the cavity. Here we shall elucidate fundamental processes of the collapse of the cavity boundary. The interaction of two or more cavities is also examined. Dependences of center-to-center distance and orientation of the cavities are studied, which reveals the presence of optimum growth rate of void fingers. The present result is applied to waterway network formation, which is considered to be one of the mechanisms of landslides at the time of heavy rainfall.

1. INTRODUCTION

The presence of a void space or a cavity in an otherwise homogeneous granular material changes the flow field, which has great influence on the deformation or migration of a cavity, as well as merging of two or more cavities.[1-8] Here an important parameter is ζ_0 (= $R_0/\sqrt{k}$), where R_0 is the size of the cavity, $\sqrt{k}$ is the characteristic length of the interstices of the granular material, and k is the permeability. In our previous analysis on the flow through a single circular cavity,[1] we have shown that the volume flow rate into a circular hole increases as much as 2 times, whereas the velocity at the center of the hole amounts to 3 times of the velocity without that hole for larger ζ_0 case (i.e. macroscopic cavity). In the presence of a spherical cavity,[3] they become 3 times and 6 times, respectively. These situations raise a question about accurate estimation of groundwater flow in natural condition because velocity measurement introduces a hole for the detector. They are also important for the formation of groundwater network, which might lead to landslides at the time of heavy rain. In this paper we shall investigate experimentally the influence of void space(s) on the flow field, as well as the deformation or growth of cavity boundary. At this moment analytical work is limited to the infinitesimal deformation of the cavity, which is complemented by numerical simulation for its further development in the granular material.

2. EXPERIMENT

2.1 Experimental Apparatus

We observed the flow field in a thin transparent rectangular box of 660mm× 360mm× 3mm, in which glass spheres of a diameter d (=1mm) are filled. A uniform steady seepage flow U_∞ of specified magnitude is maintained at far upstream side by a constant hydrostatic pressure. We show schematically our experimental apparatus in Fig.1. In our previous experiment,[6] we placed a circular disc-like hole of a diameter D about 40mm near the central region of the test section, so that $\zeta_0 \approx 600 (>>1)$, and the flow field was visualized by a fluorescent dye. Comparison of our observation with streamlines observed in independent experiment using long cylindrical hole[2] as well as comparison with those calculated by the two-dimensional theory[1] revealed that our apparatus could successfully reproduce two-dimensional seepage flow through granular material.

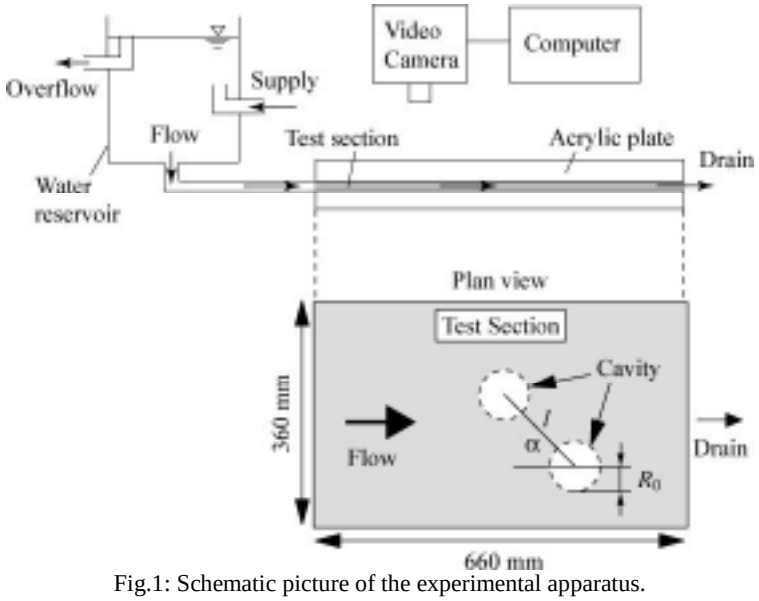

Fig.1: Schematic picture of the experimental apparatus.

2.2 Flow around Cavities of Fixed Boundary

We show the flow field around two circular holes of an equal diameter.[6] Center-to-center distance of the cavities and the angle of attack α (i.e. angle between the line joining their centers and undisturbed flow direction) are varied. In these experiment the boundary shape was kept unchanged by placing a mesh along the interface, and the flow field was observed by a video camera from above. Figures 2(a)-(c) show the streamlines around two circular cavities in (a) tandem, (b) angled, and (c) transverse positions. Flow direction is from left to right.

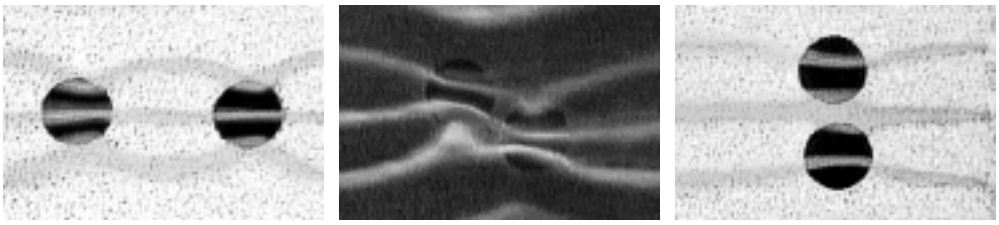

Fig 2: Two circular cavities (a) along the flow (b) at angled position $\alpha = \pi/6$ and (c) perpendicular to the flow. Center-to-center distance l is 2.5 R_0. Visualization is made by sodium fluorescein. Volume flux into the downstream-side cavity is enhanced by as much as 30% than that expected for a single cavity in (b) .

Figure 3 shows the dependence of the volume flux into cavity regions. The abscissa is the center-to-center distance l normalized by the cavity radius R_0 (i.e. $l^*=l/R_0$), whereas the ordinate is the angle of attack α. We denote ψ_u and ψ_d, respectively, the volume fluxes into upstream-side and downstream-side cavities, which are normalized by $2U_\infty R_0$ (i.e. the volume flux into the same region in the absence of the cavity). We observe that (i) when two cavities are arranged in tandem (α =0), the volume flux is almost the same as that for a single cavity ψ_s for l^* larger than about 4, but increases as l^*decreases, (ii) when two cavities are arranged across the flow ($\alpha = \pi/2$), the volume flux becomes less than that for a single cavity ψ_s as far as l^* is smaller than about 4, (iii) for $\alpha = \pi/4 \sim \pi/3$, $\psi_u \approx \psi_d \approx \psi_s$, although the streamlines near the symmetry axis deviate considerably from those for a single cavity, and (iv) for $\alpha = \pi/12 \sim \pi/6$ and l^* less than about 4, volume flux is larger than ψ_s.

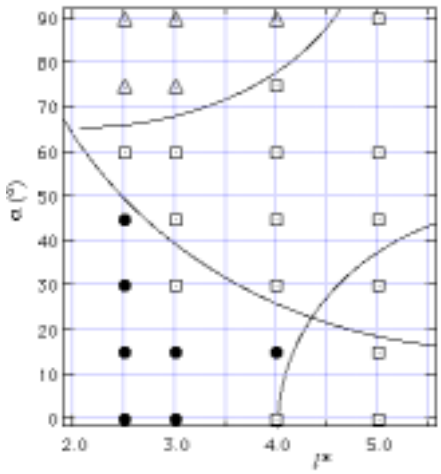

Fig.3: Volume flux into upstream and downstream cavities. Solid circles and triangles show, respectively, the increase and decrease of volume flux in comparison to a single hole. Regions with open squares show almost no changes.

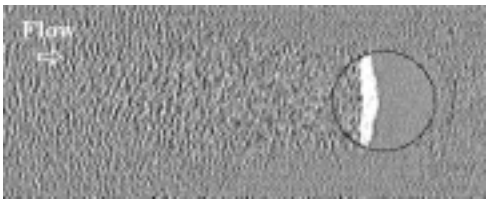

Fig.4: Collapse of a single cavity due to uniform flow (U_∞=1.6cm/s). The circle shows the initial cavity boundary (D=40mm). Fluidized region develops toward upstream direction. Subtraction of image data with time difference 0.60s.

2.3 Collapse of Cavity Region due to Viscous Flow

(i) Collapse of a single cavity due to uniform flow

Deformation of the cavity region due to viscous flow is observed by allowing the collapse of the boundary. Figure 4 is an example, in which successive image data after a certain time interval are subtracted. Undisturbed velocity U_∞ is 1.6cm/s from left to right, which is above a certain critical velocity U_{cr} at which collapse first occurs. Particles on the upstream-side boundary disintegrate and are carried away to the downstream-side boundary. This occurs because the normal stress along the upstream-side boundary is negative, whereas it is positive along the downstream-side boundary, and because granular materials are vulnerable to the former. By this process, front part of the void region moves or elongates *toward upstream direction*, leaving a fluidized region behind. In contrast to the rising bubbles in ordinary fluid, the boundary of the void in granular material is diffused and no sharp front of void region is defined. Nevertheless we could see quite rapid growth of the void tip. Time dependence of cavity area S^* and the dependence of the tip growth velocity $V_{collapse}$ on U_∞ is shown in Figs.5 and 6, respectively.

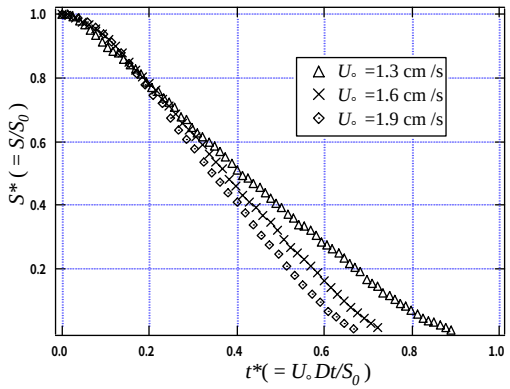

Fig.5: Change of cavity region. S^* is the area

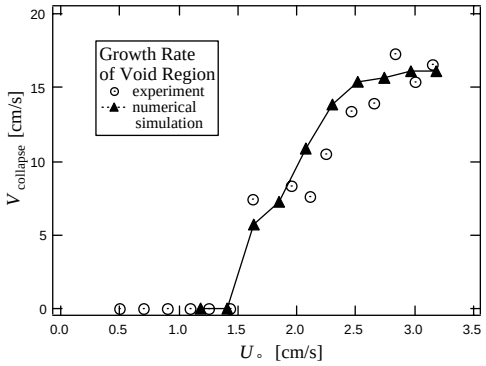

Fig.6: Dependence of growth velocity $V_{collapse}$ on U_∞.

normalized by initial area S_0, and $t^*=(U_\infty D/S_0)t$.

(ii) Collapse of two cavities due to uniform flow

Figure 7 shows the collapse of two cavities in tandem position, which are exposed to undisturbed flow (from left to right) slightly below U_{cr}. The upstream-side void remains unchanged, whereas the downstream-side one collapses due to the enhanced flow by the former. This phenomenon shows a remarkable contrast to that a solid body placed in the wake of another solid body experiences less drag in pure fluid flow. In the present case downstream-side cavity merges and no further deformation occurs. In the case of undisturbed flow sufficiently larger than U_{cr}, two voids merge and migrate toward upstream direction, or tongue-like fluidized region extends toward upstream direction.

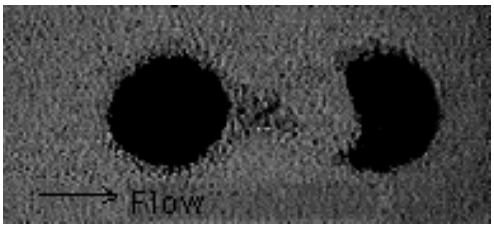

Fig.7: Collapse of two cavities in tandem position. Upstream velocity U_∞ is slightly below U_{cr}.

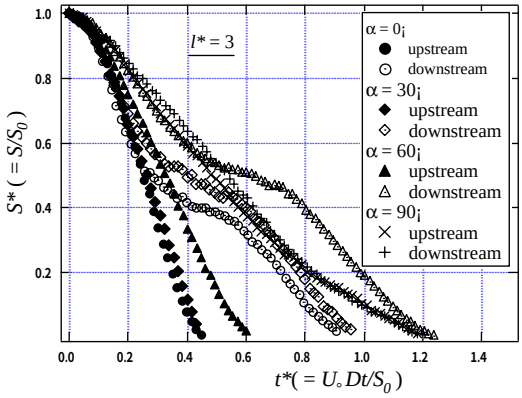

Fig.9: Change of cavity area S^* normalized by initial area S_0, and $t^*=(U_\infty D/S_0)t$.

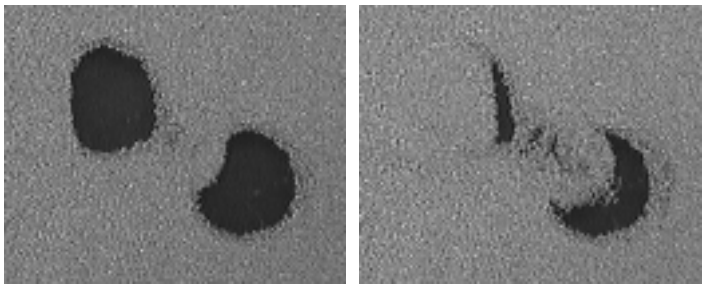

(a) (b)

Fig.8: Interaction of two cavities in angled position $\alpha = \pi/6$, $l^*=3$ and $U_\infty = 1.6$cm/s: (a) t = 0.06s and (b) t = 0.66s after the start of collapse.

When two cavities are in angled position with $0<\alpha<\pi/2$, both of the upstream-side boundary of the cavities starts to collapse, followed by faster destruction of the downstream-side cavity (Fig.8(a)). This process ceases midway, and the collapse of the downstream-side cavity is suspended until the upstream-side one completely collapsed (Fig.8(b)), which is reflected by the plateau region in the time dependence of the cavity area (Fig.9). Figure 9 also shows that the speed of the collapse is almost the same for $0<\alpha<\pi/6$, but that it decreases with α. No difference on the speed of collapse is recognized for cavities of the same size with $\alpha = \pi/2$, as is expected from the symmetry of the arrangement of the cavities. In the presence of many cavities distributed randomly in an otherwise homogeneous granular material, network formation of fluidized region followed by collapse and merge of the former was observed.

3. THEORETICAL ANALYSIS

The flow is analyzed on the basis of the generalized Darcy's equation[9-11] in a porous media and the Stokes equation in the void region. The solution is obtained so as to satisfy the continuity of velocity and stress components on the boundary of the cavity as well as the condition that the flow field approaches to uniform flow at infinity. So far we have obtained flow in and around a circular cavity,[1] slightly but arbitrarily deformed cylindrical cavity[4,5] and a spherical one[3] in a granular material. In the first case, the normal stress distribution on the boundary is proportional to cosθ, where θ is the angle measured from downstream direction, which explains the observation that the collapse of cavity almost always starts at far upstream position on the boundary. These analyses, however, are limited to infinitely small deformations, so that further development of the void space is numerically simulated.

4. NUMERICAL SIMULATION

Numerical simulation is performed, in which each particle is assumed to move with the local velocity (Lagrange's method) whereas the flow field is calculated on the fixed coordinate (Euler's method). Two-fluid model equations derived by Anderson et al. [12] :

$$\frac{\partial \varepsilon}{\partial t} + \frac{\partial \varepsilon u_i}{\partial x_i} = 0 \qquad \rho_f \frac{\partial \varepsilon u_i}{\partial t} + \rho_f \frac{\partial \varepsilon u_i u_j}{\partial x_j} = - \varepsilon \frac{\partial P}{\partial x_i} + \mu \frac{\partial^2 \varepsilon u_i}{\partial x_j{}^2} + F_i \tag{1}$$

are used as the governing equations, where ε is the porosity, ρ and μ are the density and viscosity of the fluid, respectively, $\boldsymbol{u}$ and P are the locally averaged velocity and pressure of the fluid, respectively, and $\boldsymbol{F}$ is the force acting on the fluid from the particles. The motion of each particle is computed by applying the Newton's equation of motion. The forces acting on the particle are the drag $\boldsymbol{F}_d$ by the fluid, the lubrication force from neighboring particles $\boldsymbol{F}_l$, the gravity force and the buoyancy force. Virtual mass m_0 (= ρ V_0/2 for a sphere of volume V_0) should be added to the mass of the particle m (= $\rho_p V_0$), where ρ_p is the density of the particle. Therefore, the equation of motion becomes

$$(m + m_0) \frac{d\mathbf{v}_p}{dt} = \mathbf{F}_d + \mathbf{F}_l + (m - m_1)\,\mathbf{g} \tag{2}$$

where $\boldsymbol{v}_p$ is the velocity of the particle, $- m_1 \boldsymbol{g} = - \rho V_0 \boldsymbol{g}$ is the buoyancy force and $\boldsymbol{g}$ is the acceleration of gravity. From order estimation in typical situation, the Basset term, which represents the effect of the hysteresis, is found to be negligible. The lubrication forces are given by

$$F_l^n = - \frac{3}{32 h_0} \pi \mu d^2 w^n \qquad F_l^t = \frac{1}{2} \ln 2 \; \pi \mu d \, w^t \tag{3}$$

where $\boldsymbol{w}$ denotes the relative velocity of the two particles and h_0 is the minimum distance between them. Superscripts n and t denote the components in the normal and tangential directions, respectively. As for the drag force, we employ the empirical formula derived by Ergun[13]:

$$\mathbf{F}_d = -\left[150\mu(1-\varepsilon) + 1.75\rho d \,|\, \mathbf{u} - \mathbf{v}_p \,|\right] \frac{1-\varepsilon}{\varepsilon^3 d^2} (\mathbf{u} - \mathbf{v}_p) \tag{4}$$

The computation is carried out by repeating the following four procedures: (i) determine the porosity from the locations of particles, (ii) estimate the drag on the fluid by using the porosity and the velocity, (iii) compute the flow field, and (iv) calculate the movement of each particle.

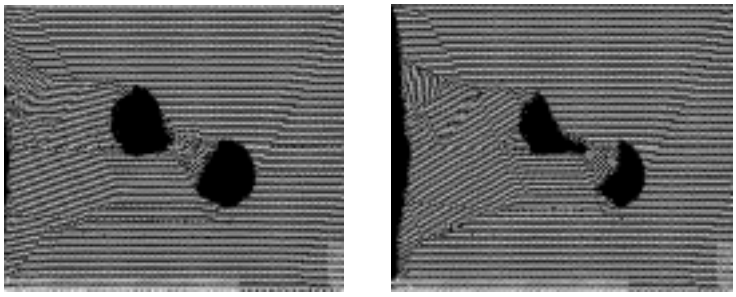

(a) (b)

Fig.10: Numerical simulation of the collapse of two cavity regions. Center-to-center distance $l = 3R_0$ and angle of attack $\alpha = \pi/6$. Number of particles is 50532.

Figures 10(a) and (b) show examples of the present calculation with the same particle size, cavity size, and undisturbed upstream velocity as those in the experiment. Center-to-center distance $l = 3R_0$ and angle of attack $\alpha = \pi/6$. Local fluidization between the two cavities, followed by the spread of the fluidized region toward upstream direction, is reproduced similarly to experimental observation.

5. CONCLUSION

1. Observation is made on the streamlines and velocity distribution around a single cavity of fixed shape in an otherwise uniform granular material, as well as those around two cavities with various center-to-center distances and orientations. In the latter, volume flux into the downstream-side cavity is enhanced by as much as 30% at a certain arrangement compared with that expected for a single cavity.
2. Experimental studies are also made on the deformation of a void due to a viscous flow. The far upstream-side position of the cavity boundary is the weakest. In the case of two cavities, the collapse of the downstream-side cavity can occur even below the threshold velocity due to flow enhanced by the upstream cavity. Collapse of the downstream cavity proceeds first, then suspended until the upstream cavity completely collapses. Narrow fluidized region grows quickly toward upstream direction.
3. Numerical simulation is made on the development of fluidized region, which qualitatively reproduces the experimental observation.

When heavy rainfall penetrates into the soil containing randomly distributed small void space, the migration and merging of the latter are expected, which is considered to be one of the mechanisms of network formation of groundwater. If this slowly progressing destruction of local arch structures in the granular material are linked at a certain phase, rapid global scale slippage will be caused, which can explain the onset of landslide.

ACKNOWLEDGMENTS

This work is partially supported by Grant-in-Aid for Scientific Research (C) from the Ministry of Education, Science and Culture, Japan.

REFERENCES

[1] Sano O: Viscous flow past a cylindrical hole bored inside porous media ----- with Application to Measurement of the Velocity of Subterranean Water by the Single Boring Method. *Nagare* 1983, **2**, 252-259 (in Japanese).
[2] Momii K, Jinno K and Hirano F: Laboratory Studies on a New Laser Doppler Velocimeter System for Horizontal Groundwater Velocity Measurements in a Borehole. *Water Resources Res*. 1993, **29**, 283-291.
[3] RajaSekhar GP and Sano O: Viscous flow past a circular/spherical void in porous media ----- an application to measurement of the velocity of groundwater by single boring method. *J. Phys. Soc. Jpn*. 2000, **69**, 2479-2484.
[4] RajaSekhar GP and Sano O: Two-dimensional viscous flow past a slightly deformed circular cavity in a porous medium. *Fluid Dyn. Res*. 2001, **28**, 281-293.
[5] RajaSekhar GP and Sano O: Two-Dimensional Viscous Flow in a Granular Material with a Void of Arbitrary Shape. *Phys. Fluids* 2003, **15** , 554-567.
[6] Kaneko Y and Sano O: Experimental Study on the Interaction of Two Two-Dimensional Circular Holes Placed in a Uniform Viscous Flow in a Porous Medium. *Fluid Dyn. Res.* 2003, **32**, 15-27.
[7] Sano O: Collapse and Growth of Cavity in a Granular Material due to Viscous Flow. *Theor. Appl. Mech.*, 2003, **52**, 91-96 .
[8] Yano H, Kieda A and Mizuno I: The fundamental solution of Brinkman's equation in two dimensions. *Fluid Dyn. Res.* 1991, **7**, 109-118.
[9] Brinkman HC: A calculation of the viscous force exerted by a flowing fluid on a dense swarm of particles. *Appl. Sci. Res.* 1947, **A1**, 27-33.
[10] Tam CKW: The drag on a cloud of spherical particles in low Reynolds number flow. *J. Fluid Mech.* 1969, **38**, 537-546.
[11] Childress S: Viscous flow past a random array of spheres. *J. Chem. Phys*. 1972, **56**, 2527-2539.
[12] Anderson TB and Jackson R: A Fluid Mechanical Description of Fluidized Bed. *Ind. Eng, Chem. Fund.* 1967, **6**,

527-539.
[13] Ergun S: Fluid flow through packed columns. *Chem. Eng. Prog*. 1952, **48**, 89-94.

Proceedings of Tenth Asian Congress of Fluid Mechanics
17-21 May 2004, Peradeniya, Sri Lanka

TRANSPORT AND DEPOSITION OF NANO- AND MICRO-PARTICLES IN A TURBULENT CHANNEL FLOW

M.D. Emami and H. Nasr
Department of Mechanical Engineering, Isfahan University of Technology, Isfahan, Iran

G. Ahmadi
Department of Mechanical and Aeronautical Engineering, Clarkson University, Potsdam, NY, 13699-5725, USA

ABSTRACT: The motion of spherical solid particles in a fully developed turbulent channel flow is numerically simulated. An empirical mean velocity profile and experimental data for turbulent intensities are used in the analysis. The instantaneous fluctuating velocities are simulated as continuous Gaussian random fields. The particle equation of motion includes the Stokes drag, the Saffman lift, the Brownian, and the gravitational forces. The Brownian diffusion is simulated as a white noise process. An ensemble of particle trajectories is generated and statistically analyzed. Several simulations for deposition of aerosol particles of various sizes are performed and the corresponding deposition velocities are evaluated. The computational model predictions for particle deposition velocity are compared with the existing experimental data and earlier simulation results.

1. INTRODUCTION

Recently increased attention has been focused on two-phase flows due to its significance in numerous industrial processes. Although gas-solid flows are very common in industrial and environmental process, their knowledge is still incomplete. The need of microelectronic industries to control microcontamination, … have motivated a number of new studies on the topic. An extensive review of particle diffusion in laminar flows was provided by Levich [1]. More recent studies in connection with microcontamination processes were presented by Cooper et. al [2] and Liu and Ahn [3]. In turbulent flows, particles are transported by the mean motion and are dispersed by turbulence fluctuation and Brownian diffusion. Fuchs [4], Davies [5], Freidlander and Johnstone [6] and Cleaver and Yates [7] provided semi-empirical expersions for particles mass flux from a turbulent stream to smooth surfaces. Extensive reviews on the subject were provided by Wood [8], Hidly [9] and Papavergos and Hedley [10]. Using digital simulation to study the diffusion of particles in turbulent pipe or channel flows was considered by a number of authors. Ahmadi and Goldschmidt [11] used numerical simulation and analytical techniques to study the turbulent dispersion of small spherical particles. McLaughlin [12], Pedinotti et al. [13], Ounis and Ahmadi [14] analyzed the aerosol particle deposition in a channel using a pseudospectral computer code to simulate the instantaneous turbulent flow field. Soltani and Ahmadi [15] studied the particle entrainment in turbulent channel flow. Chen and Ahmadi [16] studied the deposition of particles in a turbulent pipe flow. Shams et al. [17] used a sublayer model for deposition of nano- and micro-particles in turbulent flows.

The present study adopts a Lagrangian approach for analyzing particle dispersion in a turbulent channel flow. Starting with an initially uniform concentration near the wall, a series of computer simulation for deposition of aerosols of various sizes is performed. The particle equation of motion includes the Stokes drag, the Brownian and the Saffman lift, in addition to the turbulent dispersion effect and gravity. An empirical mean velocity profile and the experimental data for turbulent intensities in the channel are used for simulating the flow field. The instantaneous turbulent fluctuating velocity field is modeled by an anisotropic Gaussian random process. The Brownian motion is simulated as a white noise process.

2. PARTICLE EQUATION OF MOTION

The equation of motion for a particle in a Lagrangian framework may be written as:

$$\frac{du_i^p}{dt} = \frac{3\nu C_D \mathrm{Re}_p}{4d^2 S C_c}(u_i - u_i^p) + \frac{2K\nu^{\frac{1}{2}} d_{ij}}{S\, d\, (d_{lk} d_{kl})^{\frac{1}{4}}}(u_j - u_j^p) + g_i + n_i(t) \tag{1}$$

and

$$\frac{dx_i}{dt} = u_i^p \tag{2}$$

where $u_i = \overline{u_i} + u_i'$ is the instantaneous fluid velocity, $\overline{u_i}$ is the mean velocity vector, u_i' is the fluctuation velocity, u_i^p is the particle velocity, x_i is the particle position, t is the time, d is the particle diameter, S is the ratio of particle density to fluid density, d_{ij} is the deformation rate tensor, ν is the kinematic viscosity, $K = 2.594$ is the constant of Saffman's lift force, and g_i is the acceleration of body force, and $n_i(t)$ is the Brownian force per unit mass.

The first term on the right-hand side of the equation (1) is the drag force. Drag force is always present and is generally the dominating force for particle motion in most regions of the flow. Here C_D is the drag coefficient, which varies with particles Reynolds number, Re_p. The drag coefficient for the solid particles could be obtained from various correlations, among them:

$$C_D = \begin{cases} \dfrac{24}{Re_p} & Re_p < 1 \\ \dfrac{24}{Re_p}(1 + 0.15\, Re_p^{0.687}) & 1 < Re_p < 1000 \\ 0.44 & Re_p > 1000 \end{cases} \tag{3}$$

In which the particle Reynolds number is defined as

$$\mathrm{Re}_p = \frac{d\left|u_i - u_i^p\right|}{\nu} \tag{4}$$

In equation (1), C_c is the Stokes-Cunninghum slip correction given as

$$C_c = 1 + \frac{2\lambda}{d}\left(1.257 + 0.4\exp(-1.1\frac{d}{2\lambda})\right) \tag{5}$$

where λ is molecular mean free path of the gas.

The second term on the right-hand side of equation (1) is a generalization of the expression provided by Saffman [18] to a three-dimensional shear field.

The third and fourth terms on the right-hand side of the equation (1) are gravitational force and Brownian force, respectively. The Brownian force is very important for submicron particles. According to the standard theory on the Brownian motion (e.g. Chandrasekhar [19]), the distribution of particle velocity incremental due to the Brownian motion during Δt time, $P[\Delta u_i(\Delta t)]$, is given by

$$P[\Delta u_i(\Delta t)] = \frac{1}{\sqrt{2\pi}\,\sigma_B} \exp\left(-\frac{|\Delta u_i(\Delta t)|^2}{2\sigma_B{}^2}\right) \tag{6}$$

The standard deviation of the aforementioned distribution, σ_B, is given by

$$\sigma_B = \sqrt{\frac{216\nu k T \Delta t}{\pi \rho d^5 S^2 C_c}} \tag{7}$$

where $k = 1.38\times10^{-23}\ J/K$ is the Boltzman constant, and T is the gas absolute temperature. In the derivation of equation (6), the influence of the reaction force from the particle to fluid molecules was neglected and the Boltzman distribution was assumed. The correctness of equation (6) has been validated *a posteriori* by comparisons between observations and the prediction using equation (6) (Chandrasekhar [19]). The superficial force due to Brownian motion in time Δt, which actually is identical to the computational time step, can therefore be modeled using a Gaussian random number with zero-mean unit variance, G_i, as

$$n_i(t) = G_i \frac{\sigma_B}{\Delta t} \tag{8}$$

In this study, it is also assumed that the two phase flow is dilute and the particles have no effect on the flow field. Furthermore, the rebounding effect is neglected and when a particle reaches the wall, it is assumed that it will stick to the surface.

3. SIMULATION OF TURBULENT FLOW FIELD

The mean velocity field in a turbulent channel flow may be expressed as [20] :

$$\frac{\bar{u}}{\bar{u}_o} = \frac{1-\eta^2 - \frac{k_v'}{k'}\frac{\cosh(k'\eta)}{\sinh k'} + \frac{k_v'}{k'}\frac{\cosh k'}{k'\sinh k'}}{1+\frac{k_v'}{k'}\frac{\cosh k' - 1}{\sinh k'}} \tag{9}$$

where $\eta = 1 - \frac{y}{h}$ is the nondimensional distance from the center line, h is the half channel width, k_v' and k' are nondimensional parameters which are defined as:

$$k_v' = \frac{0.00703\ \mathrm{Re}^{0.763}}{1-0.71\,\mathrm{Re}^{0.0134}} - 2 \qquad , \qquad k' = k_v'\frac{1-0.71\,\mathrm{Re}^{0.0134}}{0.71\,\mathrm{Re}^{0.0134}} - 0.5 \tag{10}$$

Here, $\bar{u}_o$ is the mean centerline velocity and is given by

$$\bar{u}_o = V/(0.71\mathrm{Re}^{0.0134}) \tag{11}$$

where V is the mean channel velocity and

$$\mathrm{Re} = \frac{2\rho V h}{\mu} \tag{12}$$

is the flow Reynolds number. In equation (12) h is the half width of the channel, ρ is the fluid mass density, and μ is the fluid viscosity.

The experimental data of Kreplin and Eckelmann [21] for root-mean-square (RMS) turbulence intensities is used in the present analysis.

The turbulence fluctuations are random functions of space and time. The Monte-Carlo velocity simulation techniques have been used as an economical method for generating time histories that have the random characters and statistical properties of turbulence. Kraichnan [22] suggested a simple method for generating a Gaussian random field which resembles a pseudo-isotropic turbulence. Accordingly, the scaled instantaneous fluctuating velocity is given as

$$\vec{u}^{I_*}(x^*,t^*)=\sqrt{\frac{2}{N}}\left\{\sum_{n=1}^{N}\vec{u_1}(\vec{k_n})\cos(\vec{k_n}.\vec{x^*}+\omega_n t^*)+\sum_{n=1}^{N}\vec{u_2}(\vec{k_n})\sin(\vec{k_n}.\vec{x^*}+\omega_n t^*)\right\} \tag{13}$$

In this equation

$$\vec{u_1}(\vec{k_n})=\vec{\zeta}\times\vec{k_n} \quad , \quad \vec{u_2}(\vec{k_n})=\vec{\xi}\times\vec{k_n} \tag{14}$$

$$\vec{k_n}.\vec{u_1}(\vec{k_n})=\vec{k_n}.\vec{u_2}(\vec{k_n}) \ = 0 \tag{15}$$

Equation (15) ensures the incompressibility condition. The components of vectors $\vec{\zeta}_n$ and $\vec{\xi}_n$ and the frequencies ω_n are picked independently from Gaussian distribution with a standard deviation of unity. Each component of $\vec{k_n}$ is a Gaussian random number with a standard deviation of 1/2. Here, N is the number of terms in the series.

In equation (13), the dimensionless quantities are defined as

$$x^*=\frac{x}{l_o} \quad , \quad t^*=\frac{t}{t_o} \quad , \quad u_i^{I_*}=\frac{u_i^{I}}{u_o^*} \tag{16}$$

where l_o, t_o and u_o^* are the length, time and the velocity scales of turbulence and $u^{I}{}'_i$ is the fluctuation fluid velocity. For this pseudo-turbulent velocity field the energy spectrum $E(k)$ is given by

$$E(k)=16\left(\frac{2}{\pi}\right)^{\frac{1}{2}}k^4 e^{-2k^2} \tag{17}$$

where k is the wave number.

The instantaneous turbulent fluctuating velocity vector is then given by

$$u_i'=u^{I}{}'_i\, e_i(y) \quad , \quad \text{no sum on } i \tag{18}$$

where $e_i(y)$ are the shape functions for the axial, vertical, and transverse RMS velocities.(Here 1, 2, and 3 stand for x, y, and z directions, respectively.) Normal component of turbulence fluctuations near a wall has a profound effect on the deposition rate of the particles. Therefore, the magnitude of $e_2(y)$ must be correctly evaluated for small values of y. It is well known (Hinze [23]) that v' has a quadratic variation at short distances from the wall, i.e.,

$$v' \sim y^2 \quad \text{as} \quad y^+ \to 0 \tag{19}$$

In this study

$$e_2(y)=Ay^{+^2} \quad \text{for} \quad y^+ < 2 \tag{20}$$

with $A=0.0278$ is used. The normalized wall distance, y^+ may be written as:

$$y^+=\frac{y\,u^*}{\nu} \tag{21}$$

where $\nu = \frac{\mu}{\rho}$ is the kinematic viscosity of fluid.

Estimates for the length and time scales of turbulent flows were provided by Davies [24]. Accordingly

$$l_o = 0.1h(2\mathrm{Re})^{-\frac{1}{8}} \quad , \qquad t_o = \frac{l_o}{u^*} = \frac{2h}{20u^*(2\mathrm{Re})^{\frac{1}{8}}} = \frac{h}{2V} \tag{22}$$

Equation (13) and (18), with $N = 100$, together with (22) are used for simulating the fluctuation components of turbulent velocity in a channel. The interaction of particles with the local turbulence is accounted for via equation (1), in which instantaneous fluid velocity field is used.

4. SIMULATION RESULTS

The simulation results for particle transport, dispersion, and deposition for turbulent air flow in a $2\ cm$ wide channel are described. A temperature of $288\ K$, $\mu = 1.85\times10^{-5}\ N.s/m^2$ and $\rho = 1.225\ kg/m^3$ for air are used. A mean velocity of $V = 5\ m/s$ in the channel is assumed. Thus, the flow Reynolds number based on the channel width is 6657 and air is in a state of turbulent motion. The corresponding shear velocity in the turbulent field is $0.3\ m/s$.

Ensemble of 3000 particles of various sizes which are initially uniformly distributed within 30 wall units from the wall are generated and statistically analyzed. Two density ratios of $S = 1000, 2000$ and different particle diameter ranging from $0.01-100\ \mu m$ are used in these simulation. In the present simulation the particle initial velocity is set equal to the local fluid velocity. To maintain the uniform concentration in the near wall region, a reflecting boundary condition is imposed at 30 wall units. When a particle leaves the 30 wall unit boundary, an identical particle is assumed to enter the region with opposite vertical velocity.

The cases of vertical and horizontal channels are studied. In the former case, gravity is neglected. For the horizontal flow channel, simulations are performed for the lower wall region for which the gravitational sedimentation would increase the particle deposition rate.

For a uniform concentration of C_o near a surface, the deposition velocity is defined as

$$u_d = J / C_o \tag{23}$$

where J is the particle flux to the wall per unit time. The nondimensional deposition velocity is given as

$$u_d^{+} = u_d / u^* \tag{24}$$

is commonly used in the literature as a convenient measure of particle flux to the wall. In the simulations, when an initial number of particles N_o is uniformly distributed in a region within the distance of H_o from the wall, the nondimensional deposition velocity is given by

$$u_d^{+} = \frac{N_d / t_d^{+}}{N_o / H_o^{+}} \tag{25}$$

Where N_d is the number of deposited particle in the time duration t_d^{+} in the wall units. In practice, t_d^{+} should be selected in the quasi-equilibrium condition such that N_d / t_d becomes a constant.

In this study, the numerical simulation results are compared with the semi-empirical model predictions. Wood [8] developed a simple empirical equation for the nondimensional particle velocity deposition given as

$$u_d^{+} = 0.057\,Sc^{-2/3} + 4.5\times10^{-4}\,\tau^{+2} + \tau^{+}\,\boldsymbol{g}^{+}\cdot\boldsymbol{j} \tag{26}$$

where Sc is Schmidt number, and τ^+ is non-dimensinal particle relaxation time are given as

$$Sc = \frac{\nu}{D} \qquad , \qquad \tau^+ = \frac{S\, d^2\, u^{*2}}{18\nu^2} C_c \tag{27}$$

with D being the particle mass diffusivity and g^+ is nondimensional acceleration of gravity is defined as

$$g^+ = \nu\, g / u^{*3} \tag{28}$$

The first term in equation (26) accounts for the influence of the Brownian forces. This term was derived theoretically in an early study by Davies [5]. The second term models the effect of eddy diffusion. The last term in equation (26) is the gravitational sedimentation on the lower wall of horizontal ducts. In equation (26), it is assumed that the gravitational effect is linearly additive to the Brownian and turbulent eddy impaction effects.

Figure 1 compares the present simulation results with those of earlier studies in the absence of gravity. The experimental data as collected by Papavergos and Hedley [10] are also shown in this figure.

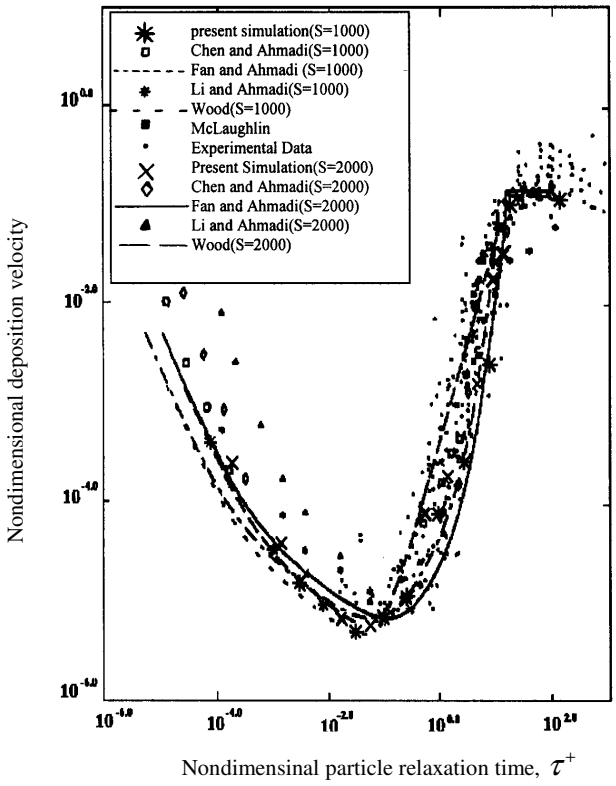

Fig. 1 Nondimensional deposition velocity versus relaxation time in a vertical channel

For a shear velocity of $u^* = 0.3$ and density ratios of $S = 1000, 2000$, the deposition velocity in a vertical channel flow for different particle relaxation times are evaluated and results are compared with the experimental and earlier simulation results in Fig. 1. The deposition velocity has a V-shape variation and is quite high for both submicron and large particles. For large particles (particle with nondimensional relaxation time over 0.1 and less than 20), the deposition efficiency increases as particle diameter

increases. The deposition velocity also approaches a roughly constant value for very large particles ($\tau^+ > 20$). For submicron particles, Brownian motion is an important mechanism near wall and deposition rate increases with decrease in particle size.

The present simulation results are in good agreement with the experimental data of Papavegos and Hedley [10], and the simulations Li and Ahmadi [25], McLaughlin [12], Chen and Ahmadi [16] and the empirical models of Fan and Ahmadi [26] and Wood [8].

Figure 2 shows the variation of nondimensional deposition velocity with particle nondimensional relaxation time in horizontal channel which includes gravitational sedimentation. A good agreement is observed between the present simulation and empirical equation given by (26). The V-shape variation is clearly observed from this figure. The minimum deposition velocity occurs for τ^+ in the range of $1.68\times10^{-3} - 1.78\times10^{-2}$ (d about $0.1-0.5\,\mu m$). This is an order of magnitude higher than for the vertical channel shown in Fig. 1.

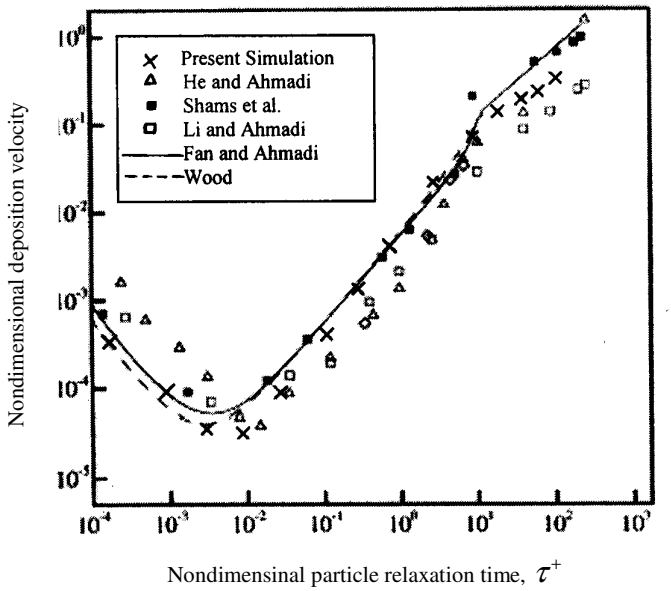

Fig. 2 Nondimensional deposition velocity versus relaxation time in a horizontal channel

5. CONCLUSION

In this study the dispersion and deposition of particles in a turbulent channel flow are studied. An empirical mean velocity profile and experimental data for turbulent intensities are used. The instantaneous turbulence fluctuation field is simulated by a continuous Gaussian random field model. The particle equation of motion, which includes the fluid drag, the Brownian force, and the Saffman lift force, is solved numerically and ensembles of trajectories for particle of different sizes are generated and statistically analyzed. The cases of horizontal and vertical channels for which the gravitational effect becomes important or negligible are studied. Based on the presented results, the following conclusions may be drawn:

1) The simulation results are in good agreement with the experimental data, the model predictions of Wood [8], He and Ahmadi [27], Shams et al. [17], Fan and Ahmadi [26], McLaughlin [12], Chen and Ahmadi [16] and Li and Ahmadi [25].

2) The deposition velocity has the expected V-shape variation in both vertical as well as horizontal channels.
3) In the vertical channel, the minimum deposition rate occurs for particle diameter in the range of $0.5-3.0\,\mu m$. For the horizontal channel, the gravitational effect shifts the position of minimum to the $0.1-0.5\,\mu m$ size range.
4) Brownian force significantly affects the deposition of small particles ($d < 0.05\mu m$) within the inner region of viscous sublayer of about 1 wall unit from the surface.
5) Small particle deposition rate increases rapidly with a decrease in particle diameter.
6) Except for the region very near the wall, turbulence is the dominating dispersing mechanism.
7) Gravity is the dominating mechanism for deposition of particles larger than $2\,\mu m$ within 1 wall unit from the surface.

REFRENCES

[1] Levich VG. ***Physicochemical Hydrodynamics***. Prentice-Hall: Englewood Clifts, NJ, 1962.
[2] Cooper DW, Peters MH, Miler RJ. *Aerosol Science Technol.* 1989, **11**, 133.
[3] Lui BY, Ahn KH. *Aerosol Sci. Technol.* 1987, **6**, 215
[4] Fuchs NA. **The Mechanics of Aerosol**. Pergamon Press: Oxford 1964.
[5] Davies CN. **Aerosol Science.** Academic Press: London 1966.
[6] Friedlander SK and Johnstone HH. *Ind. Engng Chem.* 1957, **49**, 1151.
[7] Cleaver JW and Yates B. *Chem. Engng Sci.* 1975, **30**, 983.
[8] Wood NB. *J. Inst. Engng.* 1981, **76**, 76.
[9] Hidy GM. **Aerosol, An Industrial and Environmental Science**. Academic Press: New York, 1984.
[10] Papavergos PG and Hedley AB. *Chem. Engng Res. Des.* 1984, **62**, 275.
[11] Ahmadi G and Goldschmidt V J. *Appl. Mech. ASME*, 1970, **2**, 561-563.
[12] McLaughlin JB. Aerosol particle deposition in numerically simulated channel flow. Phys. Fluids. 1989, A **1**, 1211- 1224
[13] Pedinotti S, Mariotti G, Banerjee S. Direct numerical simulation of particle behavior in the wall region of turbulent flows in horizontal channels. *Int. J. Multiphase Flow.* 1992, **18**, 927-941.
[14] Ounis H and Ahmadi G. Motion of small rigid spheres in simulated random velocity field. *ASCE J. Engng Mech.*1989, **115**, 2107-2121.
[15] Soltani M and Ahmadi G. Direct numerical simulation of particle entrainment in turbulent channel flow, *Physics Fluids*, 1995, **7**, 647-657.
[16] Chen Q and Ahmadi G. Deposition of particles in a turbulent pipe flow. **J. Aerosol Sci.** 1997, **5**, 789- 796.
[17] Shams M, Ahmadi G, Rahimzadeh H. A sublayer model for deposition of nano- and micro- particle in turbulent flows, *Chemical Eng. Sci.*, 2000, **55**, 6097-6107.
[18] Saffman PG. The lift on a small sphere in a slow shear flow. 1965, *J. Fluid Mech.*, **22**, 385-400.
[19] Chandrasekhar S. Stochastic problems in physics and astronomy. *Rev. Modern Phys*. 1943, **15**, 20-44.
[20] Ahmadi G, Goldschmidt VW, Dean B. *Iranian J. Sci. Technol*. 1976, **5**, 147.
[21] Kreplin HP and Eckelman H. *Phys. Fluids*.1979, **22**, 1233
[22] Kraichnan RH. Diffusion by random velocity field. *Phys. Fluids.* 1970, **13**, 22-31.
[23] Hinze JO. **Turbulence**. McGraw-Hill: New York, 1975
[24] Davies JT. **Turbulence Phenomena**, Academic Press: New York, 1972.
[25] Li A and Ahmadi G. Deposition of aerosols on surfaces in a turbulent channel flow. *Int. J. Engng Sci*. 1993, **31**, 435-451.
[26] Fan FG and Ahmadi G. A sublayer model for turbulent deposition of particles in vertical ducts with smooth and rough surfaces. *J. Aerosol Sci*. 1993, **24**, 45-64
[27] He C and Ahmadi G. Particle deposition in nearly developed turbulent duct flow with electrophoresis. *J. Aerosol Sci.* 1999, **30**, 739-758.

Proceedings of the Tenth Asian Congress of Fluid Mechanics

17-21 May 2004, Peradeniya, Sri Lanka

PARTICLE DISPERSION IN A DOUBLE FREQUENCY FORCED SHEAR LAYER

V. Aga, P. Bala, R.I. Sujith
Department of Aerospace Engineering, Indian Institute of Technology Madras, Chennai-600036, India

ABSTRACT: Particle laden shear layer flows are encountered in many industrial and environmental systems. In this paper, a shear layer formed due to the flow over a splitter plate is studied. Shear layer flows have a natural instability frequency of vortex shedding. This paper investigates the effect of exciting this flow with a combination of its natural instability frequency and an added sub-harmonic. The enhancement of vortex pairing leading to subsequent enhanced dispersion is the motivation for this forcing. The combination of such frequencies and the phase difference between the first and second frequency are parameters which affect the vortex pairing. Discrete vortex methods are successfully applied to calculate such a flow including oscillations imposed on it. Being a high Reynolds number calculation, the viscosity effects are ignored. Lagrangian tracking of particles introduced into the flow using drag correlations are used to detect their dispersion. Spatial and temporal dispersion are quantified and the results suggest that dispersion increases when there is increase in vortex pairing as well as when the shear layer strength is high thereby causing greater asymmetric entrainment (entrainment of the particles away from the high speed side). Vortex pairing is enhanced by a judicious choice of forcing frequencies and their phase difference combinations. Asymmetric entrainment increases when the difference between the high-speed and low-speed flow velocities is increased.

1. INTRODUCTION

Particle laden turbulent flows occur in numerous technological and environmental systems. A mixing chamber where dispersion of the liquid phase in the gas phase occurs is a general example of such systems. Shear layer flows are often encountered in such geometries. It has been shown by Sujith et al. [17, 18] that droplet motion and evaporation is affected by acoustic oscillations. Calculation of a shear layer flow by discrete vortex method gives an accurate picture of the flow, as reviewed by Leonard [13] and later applied by Horender [7] and Uchiyama and Naruse [19] to study the dynamics of particle-laden shear flows in the absence of oscillations. Experimental results by Husain and Hussain [8] and Oster and Wygnanski [15] have studied the presence of a 'natural instability frequency' of a shear layer. At a sub-harmonic of the natural instability frequency, Husain and Hussain [8] observed the growth of the shear layer and enhanced vortex pairing. Aggarwal et al. [2], and, Martin and Meiburg [14] have observed that maximum particle dispersion takes place when the Stokes number of the particle is intermediate (St~1). Aggarwal and Xiao [1] in a Flux Corrected Transport (FCT) simulation have calculated the effect of forcing by oscillations of a single frequency on a particle-laden shear layer. They observed that forcing at the sub-harmonic of the natural frequency tends to increase the dispersion. However, they did not investigate the effect of forcing with double/multiple frequencies and effect of shear strength. Inoue [10] has calculated, using vortex methods, a single-phase double-frequency forced shear layer.

Since the above studies have shown that harmonic and sub-harmonic forcing have a significant effect on the dynamics of large-scale structures of the shear layer, it would be of interest to study their effect on the dispersion of particles in such a flow.

In this study, the flow itself is simulated using Krasny vortex blobs as fluid elements [11]. Unlike previous discrete vortex method simulations [7, 9, 19], the splitter plate here is divided into panels with a linear variation of vortex strengths across each panel, for a more accurate representation of the vorticity field. The code is validated by comparing the mean velocity profiles with the experimental results by Horender [7].

The multi-phase flow considered in this study is quite dilute and hence owing to this low loading one-way coupling is sufficient, i.e., the particles do not affect the evolution of the flow. The Stokes number of the particles is maintained at 1 to observe the maximum centrifuging effects. The momentum thickness of the shear layer very near the splitter plate is calculated to give the length scale for the flow, which can be used to obtain the Stokes and Strouhal numbers. The forcing frequency is then obtained from the Strouhal number. The mean velocity is sinusoidally forced using two frequencies with the second one having a phase difference with respect to the first. Various dispersion functions are used to fully quantify the dispersion both in a spatial as well as the temporal sense. The dependence of the dispersion functions on the parametric space comprising shear layer strengths, frequency and phase combinations is investigated.

2. MATHEMATICAL FORMULATION AND NUMERICAL PROCEDURE

The unsteady two dimensional flow over the splitter plate is simulated using the vortex methods. In vortex methods, each fluid element possessing vorticity is represented as a vortex blob. Each vortex blob is convected

according to the velocity induced at its centre by the remaining blobs and the vorticity distributions at appropriate boundaries. The gas phase is calculated in terms of the vorticity.

Neglecting 3-D effects and viscous diffusion because of the high Reynolds number of the flow, the vorticity transport equation reduces to:

$$\frac{Dw}{Dt} = 0 \tag{1}$$

This implies that if one travels with the fluid element, the vorticity remains constant. This is the basis for simulating the flow using point vortices. To prevent singularities near the vortex centre a Krasny blob is introduced as given by Krasny [11]. The velocity induced at any point (x, y) is given by the Biot-Savart law:

$$u(x,y) = \frac{1}{2p}\sum_{i=1}^{N}\frac{y - y_i}{|r - r_i|^2 + b^2} + u_{convect} \qquad v(x,y) = \frac{1}{2p}\sum_{i=1}^{N}\frac{x - x_i}{|r - r_i|^2 + b^2} \tag{2}$$

Here, b is the core radius of each vortex blob. The convective velocity imposed over the whole flow field is given by the average of U_1 and U_2, the velocities above and below the splitter plate respectively.

The geometry of the flow set-up (see Fig. 1) consists of a splitter plate separating the high speed fluid on the top and low speed fluid below to form a mixing layer. The two semi-infinite vortex sheets are used to satisfy the inflow and outflow conditions for this setup. The end of the splitter plate is divided into a hundred panels, having a linear variation of vortex strength as shown in Fig. 2. Each arrow in Fig. 2 represents the shear strength at the edge of the panel. The vortex strength varies linearly along a straight line across a panel from one shear strength arrow to the next.

Fig. 1. Geometry of flow

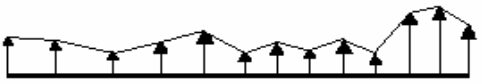

Fig. 2. The linear variation of the vortex strengths over the splitter plate panels

Unlike the simulations of Inoue [10], Horender [7] and Uchiyama and Naruse [19], the vortex blobs are not placed on the splitter plate, but at every time step the no-transpiration condition (i.e. normal velocity at any point on the panel is zero) is satisfied at pre-determined points on every panel to determine the new vortex strength variations. The vorticity is more accurately calculated because of the linear variation of vortex strengths along the splitter plate. Also, the effect of the previously convected flow on the evolution of the flow to be shed is captured. A semi-infinite vortex sheet originates from the splitter plate in the negative x-direction. This has a constant vortex strength $g = U_2 - U_1$. To satisfy the outflow condition, another similar semi-infinite plate originating from a conveniently distant point is placed.

Lagrangian tracking of the particles is carried out based on the drag due to the flow. The velocity is thus given by:

$$\frac{dU_{py}}{dt} = f_{Drag\ y} + g \qquad \frac{dU_{px}}{dt} = f_{Drag\ x} \tag{3}$$

The drag force f_{Drag} is given by the following:

$$f_{Drag} = \frac{3C_D|U_f - U_p|(U_f - U_p)}{4d_p g} \tag{4}$$

U_f is the stream wise or cross-stream velocity on the particle induced by every fluid element, and U_p is the corresponding stream wise or cross-stream particle velocity. A 4th order Runge-Kutta numerical integration is used to convect the particles from one position to the other at every time step.

The drag coefficient is estimated according to Clift et al. [3] as:

$$C_D = \frac{24}{Re_p}\left(1 + 0.15\,Re_p^{0.687}\right) \qquad Re_p = \frac{d_p|U_f - U_p|}{n} \tag{5}$$

This correlation is valid for $Re_p < 1000$, which will be the case for the present calculations.

The time step dt is taken, as 2.5 x 10^{-4}s as reducing it further does not significantly affect the results. The convective velocity; $(U_2 + U_1)/2$ was maintained at 18 m/s and computations were performed for various values of U_1 and U_2 for different shear strengths. The ratio $r = U_1/U_2$ is set to 0.5 for most of the forcing calculations. The unsteady velocity is expressed as:

$$U = U[1 + a\sin(2pf_1 t) + a\sin(2pf_2 t + f)] \tag{6}$$

The second frequency is normally a sub-multiple of the first and f is the phase difference between the two.

In order to calculate the Stokes and Strouhal numbers, a length scale representing the shear layer is required. Such a length scale is obtained by calculating the momentum thickness at the end of the splitter plate. Momentum thickness as used by Inoue [10] is:

$$q = \frac{U_c - U_2}{U_1 - U_2}\left(1 - \frac{U_c - U_2}{U_1 - U_2}\right) dy \qquad (7)$$

Here U_c is the convective velocity $Uc = (U_2 + U_1)/2$. This definition is an equivalent way of defining thickness for this inviscid computation in order to mimic the definition of a measured q observed in experiments.

The natural instability frequency as observed by Husain and Hussain [8] occurs at a Strouhal number of 0.012. The natural frequency of the shear layer, f, is then given by

$$\frac{fq}{U_1 + U_2} \quad 0.012 \qquad (8)$$

The Stokes number with respect to the flow determines the particle size. St ~ 1 is maintained for all the simulations as the work by Martin and Meiburg [14] and Aggarwal and Xiao [1] show that maximum dispersion takes place at such intermediate Stokes' numbers.

$$St = \frac{\rho_p U d_p^2}{\rho_f 18 \mu q} \qquad (9)$$

3. RESULTS AND DISCUSSION

The flow bereft of particles is first described. The convective velocity was oscillated according to equation (6). The comparison of unforced and forced flow is seen in Fig. 3a and 3b. The forced flow in Fig. 3b shows greater number of vortices pairing up than in Fig. 3a. The terminology used henceforth is: F is the forcing frequency, f denotes the instability frequency of the shear layer and f is the phase difference between the two frequencies as given by equation (6). A forcing of $U = U[1 + a\sin(2\pi f_1 t) + a\sin(2\pi f_1 t + f)]$ is represented as $(f_1 + f_2(f))$ for convenience. The particles are introduced from the edge of the splitter plate after the shear layer has developed for some time. The initial transient thus exits the region of interest and the particles are introduced into flow when the large-scale structures have assumed a quasi-periodic behavior. Figure 4 shows the particle distribution in the flow. It is observed that forcing at the double frequency i.e. $F = f + f/2$ does indeed lead to a greater dispersion of the particles as compared to an unforced flow.

Another important observation is the phenomenon of asymmetric entrainment in Fig. 4 wherein particles disperse more away from the high-speed side which is on the top-side of the splitter plate denoted by U_2. Koochesfahani et al [11] and Grinstein et al [6] have experimentally observed the phenomena of asymmetric entrainment, though previous simulations using vortex methods [14, 16, 19] have not reported this.

3.1 Temporal Dispersion Function

Firstly the temporal dispersion function as used by Aggarwal and Xiao [1] is defined in terms of a dispersion function D as:

$$D = \sum_{i=1}^{p} \frac{Y_t^2}{p}^{1/2} \qquad (10)$$

where p is the total number of particles released till time t and Y_t is the vertical distance of a particular particle from the splitter plate at that time.

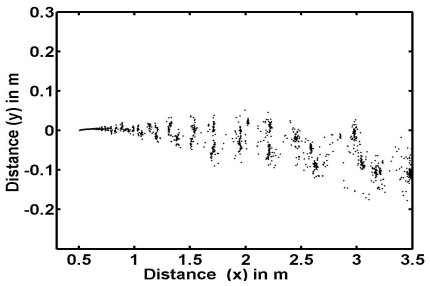

Fig. 3a. Fluid element distribution of an unforced flow.

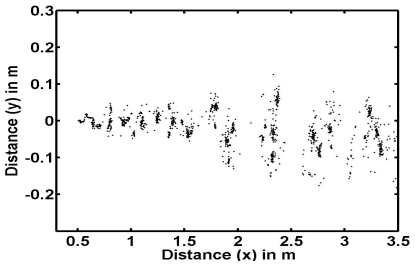

Fig. 3b. Fluid element distribution of $f+f/2(p/2)$ forced flow.

The effect of the various frequencies on temporal dispersion is seen in Fig. 5a and 5b. Figure 5a shows that when the sub-harmonic is an even sub-multiple of the instability frequency, greater dispersion is observed, rather than on forcing with an odd sub-multiple. Figure 5a also shows that when the sub-harmonic is 90° out of phase with respect to the natural frequency the temporal dispersion is much higher. For the forcing combination

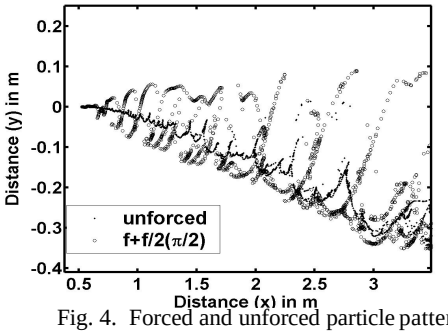

Fig. 4. Forced and unforced particle patterns

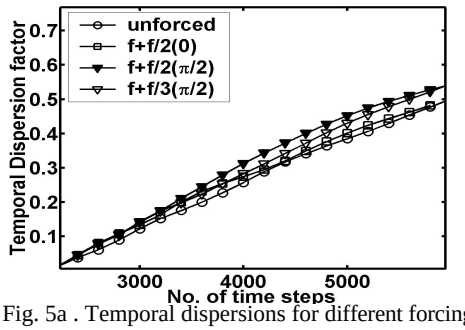

Fig. 5a . Temporal dispersions for different forcings.

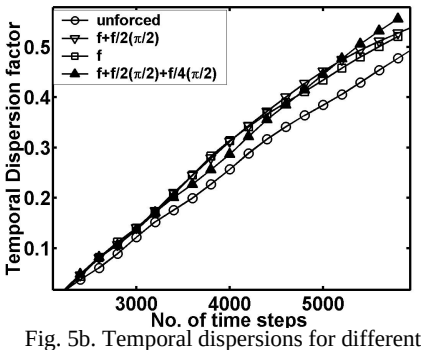

Fig. 5b. Temporal dispersions for different forcings

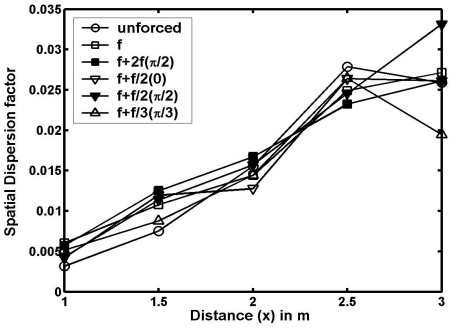

Fig. 6. Spatial dispersion function for various forcings.

f+f/3(*p*/2), the temporal dispersion is still greater than the *f+f/2*(0) combination even though the odd-sub multiple causes lesser dispersion than the even sub-harmonic. The phase difference between the two frequencies might have lead to enhanced vortex pairing notwithstanding the attenuating effects of the odd sub-multiple.

Figure 5b shows the influence of a single frequency and a combination of three frequencies with additional harmonics out of phase with the fundamental. Forcing at the natural frequency causes greater dispersion than its sub-multiple forcing alone. Adding more frequencies seems to enhance the dispersion, but this is so only if the third frequency is an even sub-multiple and the additional frequencies are ninety degrees out of phase with the fundamental as can be seen from Fig. 5b. The correspondence between vortex pairing and dispersion is established from these results.

3.2 Spatial Dispersion Function

In many applications the dispersion of the particles before they reach a particular distance (e.g. a flame holder in the case of a combustor) is critical. A spatial dispersion function is required to characterize such dispersions. At various horizontal distances, all particles within a sliver extending vertically are considered and the dispersion function (equation (10)) considering just those particles is computed, i.e., *p* in equation (10), is the number of particles at a particular horizontal distance at the end of the simulation. The dispersion function corresponding to each spatial value is plotted for different frequencies in Fig. 6.

It is observed from Fig. 6 that the (*f* + 2*f*(*p*/2)) component leads to lesser spatial dispersion, almost as if it was unforced. It is observed therefore that while a sub-harmonic component enhances dispersion, a higher multiple of the fundamental frequency does not. Again, the (*f+f*/3(*p*/2)) forcing has a lower dispersion than the other combinations, because the odd sub-multiple component leads to reduced vortex pairing than the even sub-harmonics. The (*f+f/2*(p/2)) frequency enhances vortex pairing the most and hence shows maximum dispersion.

3.3 Time-averaged particle concentration profile

The dispersion is also quantified using a profile with the stream-wise direction of particle concentrations at various probe cells. Cells are made at many cross-stream points at one stream-wise distance, say *x=2m*. Each cell is 1 cm by 1 cm in dimension. The number of particles passing through each cell at every time step is recorded and these values are time averaged to obtain a mean profile with respect to the cross-stream direction. A flatter curve with a greater longitudinal spread would indicate greater cross-stream dispersion as the particles pass through a wider range of vertical distances. As observed in Fig. 7, the longitudinal spread of the forced flows is more than the unforced ones. It is seen that a single frequency forcing creates a marginally larger longitudinal dispersion spread than the double frequency forcing. The phase difference between the two

frequencies does not radically affect the asymmetric entrainment or the longitudinal spread of the particles at the stream-wise direction under investigation. Owing to the time averaged nature of these plots, the effect of phase might be overshadowed by the additional frequency component. This plot clearly shows that the spread is not even about the $y = 0$ line and it is away from the high-speed side of the shear layer. Though gravity effects are considered in the simulation, its effect is not the primary cause of this asymmetric spread. Test simulations showed that the concentration plots with and without gravity didn't show any significant difference.

Shear strength effects on dispersion in a (f+f/2(p/2)) forced flow

Figure 8 shows the dispersion due to changes in shear layer strength expressed as $r = U_2/U_1$, the ratio of the low-speed velocity to high-speed velocity on opposite sides of the splitter plate. In order to get a relation only due to the shear strength and to reduce the effect of varying convective velocity, the mean velocity $(U_2+U_1)/2$ is maintained constant for all the cases and the values of U_2 and U_1 are changed to vary the ratio r.

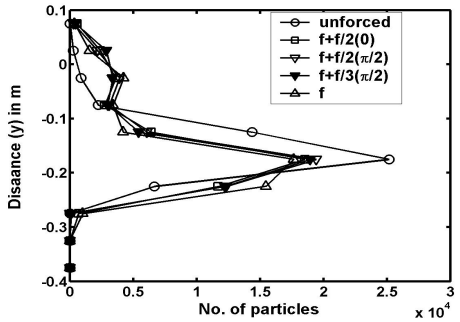

Fig. 7. Particle concentration plots for various forcings.

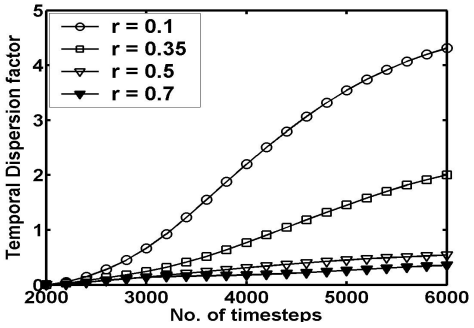

Fig. 8. Temporal dispersion for varying shear strengths.

All the flows are also oscillated with (f+f/2(p/2)), f being the natural instability frequency for a particular velocity ratio of that shear layer. The temporal dispersion pattern exhibits a marked increase in dispersion due to greater shear layer strengths. The response of a shear layer to forcing seems to be greater at lower r, as the dispersion increases very considerably for $r = 0.1$.

Figure 9 gives a particle concentration plot at $x = 2$m for different values of the shear strengths with all the flows being forced at (f+f/2(p/2)). This result shows a marked increase in asymmetric entrainment with increasing shear layer strength. This is deduced as there is an increase in the number of particles that are passing through a probe point far below the centerline, than through a probe point above the centerline. The asymmetric entrainment is enhanced very significantly for $r = 0.1$ and the peaks of the plots are nearer to the centerline for lower shear layer strengths, denoting the variation in asymmetric entrainment.

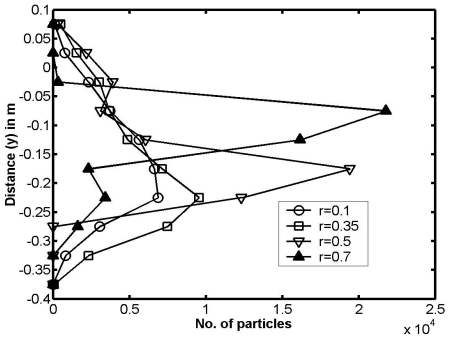

Fig. 9. Particle conc. plots for varying shear strengths.

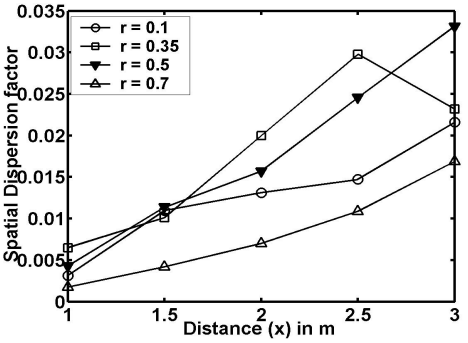

Fig. 10. Spatial dispersion plots for different shear strengths

An important observation is that though the peaks of the $r = 0.1$ and 0.35 plots are behind that of the $r = 0.5$ curve, the longitudinal spread in the region above the splitter plate is not significantly greater. The dispersion is enhanced mostly towards the low-speed direction. This shows a fairly strong dependence of asymmetric entrainment on the strength of the shear layer. Figure 10 shows the enhanced dispersion due to greater shear strengths with all the flows being forced at (f+f/2(p/2)). The $r = 0.5$ flow has a greater dispersion than the $r = 0.1$ flow at the 1 m stream-wise station. At later positions, the stronger response of the higher shear strengths to forcing is observed. The strongest shear layer has maximum dispersion at the furthermost spatial

location. At a very weak shear strength of $r = 0.7$, it is seen that the flow disperses the particles meagerly. It is to be noted from the observations of particle concentration plots (Fig. 10.) that the enhanced dispersion due to increasing shear strengths is more due to their asymmetric entrainment enhancement caused by the forcing than due to greater number of vortex pairings. The basis for the greater dispersion seen in Fig. 8 and 10 is given by Fig. 9 which shows greater asymmetric entrainment due to stronger shear layers.

4. CONCLUSIONS

The effect of a combination of the natural frequency of a shear layer combined with its sub-harmonic, on the dispersion of inertial particles of St ~ 1, in a shear layer is studied here. The effect of shear strength on the dispersion in such a forced flow is also investigated.

Dispersion enhancement in a shear layer is accomplished through two processes. One way of is by increasing the asymmetric entrainment, though it does not lead to an even spread about the centerline. Asymmetric entrainment increases with increase in strength of the shear layer. Another way to enhance dispersion would be by increasing vortex pairing by forcing at particular multiple frequencies with phase differences in order to create greater vortex pairing. A double frequency does indeed lead to a greater dispersion caused by enhanced vortex pairing. An even sub-multiple of the natural frequency having a phase difference of /2 with the fundamental, enhances dispersion. Higher multiples and odd sub-multiples of the natural frequency attenuate the dispersion. Adding more frequencies will increase dispersion provided they are even sub-multiples that are out of phase and so increase vortex pairing in the flow. Dispersion may be investigated using more than one quantification function and such a process would give a more comprehensive view of the dispersion process. This is validated as the time-averaged particle concentration plots exhibit the effect of asymmetric entrainment, although the spatial and temporal dispersion functions do not give insight into this process. Similarly the dispersion of particles in space as well as in time should be studied simultaneously for the complete picture.

5. REFERENCES

[1] Aggarwal SK and Xiao Y, Effect of external forcing on droplet dispersion in a developing shear layer. *J. Propulsion and Power*. 1994, 10(3), 395-401.

[2] Aggarwal SK, Yapo, JB, Numerical simulation of particle transport in planar shear layers. *Computers and Fluids.* 1996, 25(1), 39-59

[3] Clift R Grace JR and Weber ME. ***Bubbles, drops and particles***. Academic Press, New York, 1978.

[4] Crowe CT, Chung, JNC, Troutt, T R Particle mixing in free shear flows. *Prog. Energy Combus. Sci.* 1998, 14, 171-194.

[5] Ghoneim AF and Ng KK, Numerical study of vortex merging in mixing layers. *Phys. Fluids.* 1987, 28(6), 706-721.

[6] Grinstein, FF, Oran, ES, Boris JP, Numerical Simulations of asymmetric mixing in planar shear flows. *J. Fluid Mech.* 1986, 165, 201-220.

[7] Horender S Experiments and Simulations of particle laden turbulent shear flows. Ph. D. Thesis, 2002, Imperial College of Sci., Tech. and Medicine.

[8] Husain, SH and Hussain F, Experiments on subharmonic resonance in a shear layer. *J. Fluid Mech*. 304 (1995) 343-372

[9] Inoue, O Double-frequency forcing on spatially growing mixing layers. *J. Fluid Mech.* 1992, 234 , 553-581.

[10] Koochesfahani, MM, Dimotakis, PE, Broadwell, JE A flip experiment in a chemically reacting turbulent mixing layer. *AIAA J.* 1985, 23, 1191-1198.

[11] Krasny R Computation of vortex sheet roll-up in the Trefftz plane. *J. Fluid Mech.* 1987, 184, 123-155.

[12] Lazaro BJ and Lasheras JC Particle dispersion in the developing shear layer. Part 2, forced flow. *J Fluid Mech.* 1992, 235, 179-221.

[13] Leonard A. Vortex methods for flow simulation. *J. Comp. Physics*. 1980, 37, 289-335.

[14] Martin JE and Meiburg E The accumulation and dispersion of heavy particles in forced two-dimensional mixing layers. Part 1, The fundamental and subharmonic cases. *Phys. Fluids.* 1994, 6, 1116-1131.

[15] Oster D and Wygnanski I The forced mixing layer between parallel streams. *J. Fluid Mech.* 1982, 123, 91-130.

[16] Raju N and Meiburg E The accumulation and dispersion of heavy particles in forced two-dimensional mixing layers. Part 2, the effect of gravity. *Phys. Fluids.* 1995, 7(6), 1241-1264.

[17] Sujith RI, Waldherr GA, Jagoda JI and Zinn BT An Experimental Investigation of the Behavior of Droplets in Axial Acoustic Fields", *Journal of Vibration and Acoustics*. 1997, 119, 285-292.

[18] Sujith RI, Waldherr GA, Jagoda JI and Zinn BT Experimental Investigation of the Evaporation of Droplets in Axial Acoustic Fields, *Journal of Propulsion and Power*. 2000, 16(1), 278-285.

[19] Uchiyama T and Naruse M, A numerical method for gas-solid two-phase free turbulent flow using a vortex method. *Powder Technology*. 2001, 119, 206-214.

Proceedings of the Tenth Asian Congress of Fluid Mechanics
17–21 May 2004, Peradeniya, Sri Lanka

OBSERVATIONS ON SOME BUBBLE DRIVEN PLANE LAMINAR FLOWS

V. H. Arakeri, A. Pal and S. N. Goswami
Department of Mechanical Engineering, Indian Institute of Science, Bangalore 560012, India
M. Alam
Engineering Mechanics Unit, JNCASR, Bangalore 560064, India

ABSTRACT: We report observations on some bubble driven plane laminar flows. These flows are not only of interest due to their unique characteristics but can also serve as benchmarks for developing computational methods to handle broader class of two-phase flows. Two classes of bubble driven flows are considered here in some detail; one is interaction of bubble plumes with different boundary conditions and the second is analysis of bubble plume driven flow in a closed environment. From bubble plume interaction observations, we have been able to estimate the value for the entrainment coefficient.

1. INTRODUCTION

When bubbles are continuously released from a source in a large mass of liquid, a bubble driven plume flow is established. As shown in Fig. 1(a), the bubbles are confined in a narrow region of the plume which can be termed as the core region. Initially the flow is laminar, then goes through transition and finally becomes turbulent. Such flows, both axisymmetric and plane, find some applications in geophysical context and chemical and metallurgical industries. For example, uniformity in a molten metal pool can be established by injection of gas bubbles at selected locations. In such situations, it is of interest to predict the velocity field established by the bubble driven flow. To accomplish this, special tools to adequately model the influence of the core region containing bubbles are required. One simple way is to use the homogeneous model, where the two-phase region is considered to be a pseudo single-phase region with differing properties, which are generally evaluated on a weighted average basis[1]. Use of this model by us will be indicated in a later section. There are other more sophisticated models, like the use of two-way coupling simulations. Recently, such a model has been used by Caballina et al.[2] to investigate the instabilities in a plane bubble plume as depicted in Fig. 1(a). They have been able to show very good general agreement with experimental observations reported in Alam & Arakeri[3]. This clearly demonstrates that controlled experiments of the type reported here can not only provide basic information on the bubble-induced flows, but also provide a set of benchmark experiments against which numerical simulation results can be compared with. With this aim, in the present study, we look at two classes of basically two-dimensional or plane bubble-driven flows. One is the interaction of laminar bubble plumes either among themselves or with a wall, which has been done with different boundary conditions on access for entrained fluid. The second one is observation of flow induced by a bubble curtain and comparison of this with numerical computations has also been undertaken.

2. BUBBLE PLUME INTERACTIONS

When two plane bubble plumes, of the type shown in Fig. 1(a), are generated close to each other they interact and come together as illustrated in Fig. 1(b). Similarly, a bubble plume interacts with a wall, if it is in close proximity. The nature of interaction depends on the boundary conditions under which access of entrained fluid is allowed.

Here we have investigated various combinations of interactions as depicted schematically in Fig. 2. The interaction has been characterized by measuring the interaction height, h, as a function of the spacing, a, for various configurations indicated. In all the cases, the bubble plumes were generated using an electrolysis bubble generator (EBG). Basically it consisted of a cathode strip, etched out precisely from a pcb (printed circuit board), and an anode which was just a copper-clad plate immersed in the fluid and placed sufficiently away from the cathode such as not to disturb the bubble plume. The strength of the bubble plumes could be controlled by varying the magnitude of the DC voltage applied across the cathode and the anode. Using Faraday's law, the amount of gas produced can be precisely calculated by measurement of the current in the circuit. It may be noted that the bubble plumes generated using EBG are of low void fraction ($\sim 10^{-3}$), and consist of nearly uniform size bubbles estimated to be about 100 μm. The above features are of great advantage of generating bubble plumes using this technique over other methods like injecting gas through a porous plate. In the case of two plumes, special care was taken to ensure the equality of strengths of each plume. Observations consist of photographing the plume using a light sheet technique as described in [3] and from these photographs the interaction height h, as depicted in Fig. 2, could be measured. The variation of h with spacing, a, for various cases at one gas flow rate is shown in Fig. 3. The results were similar for other gas flow rates. Unlike in case (a) of Fig. 2, for case (b) the plumes did not merge to become a single plume, after attaining a minimum spacing they travelled parallel to each other. This is clearly the influence of entrainment from the bottom. As expected, the plume interaction is the strongest in case (d) where the access to entrainment is the least. As shown in Fig. 3, the plume interaction height is the minimum for this case. Flow visualization studies showed that a well defined recirculating region formed between the plume and the wall for this case. This difference in the interaction height observed for the cases (b) and (c) is due to the effect of the wall; otherwise, due to symmetry the two flows should have been very similar.

By analysing the results from case (b) and using a methodology described in Pera and Gebhart[4], it is possible to get an estimate for the entrainment coefficient E, defined by $E = V_\infty / U_c$. Here, V_∞ is the far field entrainment velocity and U_c is the average plume centerline velocity. We found a value for E ranging from 0.04 to 0.055 for various gas flow rates and plume spacings. Considering the fact that the entrainment coefficient for a turbulent plume is about 0.08 [5], it is surprising that for the laminar case the magnitude is comparable. This is perhaps an indication of the unique characteristics of bubble driven flows.

3. BUBBLE DRIVEN FLOW IN A RECTANGULAR BOX

When bubbles are released as a line source in a closed environment like in a large aspect ratio rectangular box, a bubble curtain driven, nearly two-dimensional, flow is established. The general

characteristics of such a flow are depicted in the flow visualization photograph of Fig. 4(A). One might expect some similarity of this flow with the classical lid-driven cavity flow[6]. However, there are two important differences: one is that the bubble plume which acts as driving wall does not have a constant velocity, and the second is that a free surface forms one of the boundaries.

By using the homogeneous model[1] to handle the bubble containing region, the two-dimensional flow field was computed by using the standard incompressible form of the Navier-Stokes equations with appropriate boundary conditions. It should be noted that the bubbles are assumed to leave the computational domain at the free boundary. One example of such simulations is indicated in Fig. 4(B). It is found that the computed flow field resembles the observed flow field quite closely; there are some noticeable differences, however, like the orientation of the primary vortex. Improved modelling of the two-phase region may result in better agreement with experimental observations.

4. CONCLUSIONS

Observations on bubble plume driven laminar flows indicate that they form an interesting class of flows. It appears that efficient mixing is possible even with laminar flows induced by a confined swarm of bubbles. This conclusion is based on our estimated value for entrainment coefficient being nearly of the same order as its turbulent counterpart. We might expect bubble plumes, where lateral dispersion of second species is limited, to behave as thermal plumes in the very high Prandtl number limit. This needs to be formally investigated and our present studies should form a basis towards this end. When a single bubble plume driven flow in an otherwise unconfined medium is considered, modelling is relatively straightforward since the location of the bubble core region can be assumed to be known. However, when bubble plume interactions are to be studied computationally, it may be a much more difficult task since in this case the position of the bubble core region is unknown *a priori* and needs to be calculated as part of the overall computations. The interaction studies reported here can again form a benchmark for verification of such calculations.

REFERENCES

[1] Wallis GB. **One-Dimensional Two-phase Flows**. New York: McGraw Hill, 1969.

[2] Caballina O, Climent E and Dŭsek J: Two-way coupling simulations of instabilities in a plane bubble plume. *Phys. Fluids.* 2003, **15**(6), 1565-1544.

[3] Alam M and Arakeri VH: Observations on transition in plane bubble plumes. *J. Fluid Mech.* 1993, **254**, 363-374.

[4] Pera L and Gebhart B: Laminar plume interactions. *J. Fluid Mech.* 1975, **68**, 259-271.

[5] Fannelop TK, Hirschberg S and Küffer J: Surface currents and recirculating cells generated by bubble curtains and jets. *J. Fluid Mech.* 1991, **229**, 629-657.

[6] Shankar PN and Deshpande MD: Fluid mechanics in the driven cavity. *Ann. Rev. Fluid Mech.*, 2000, **32**, 93-136.

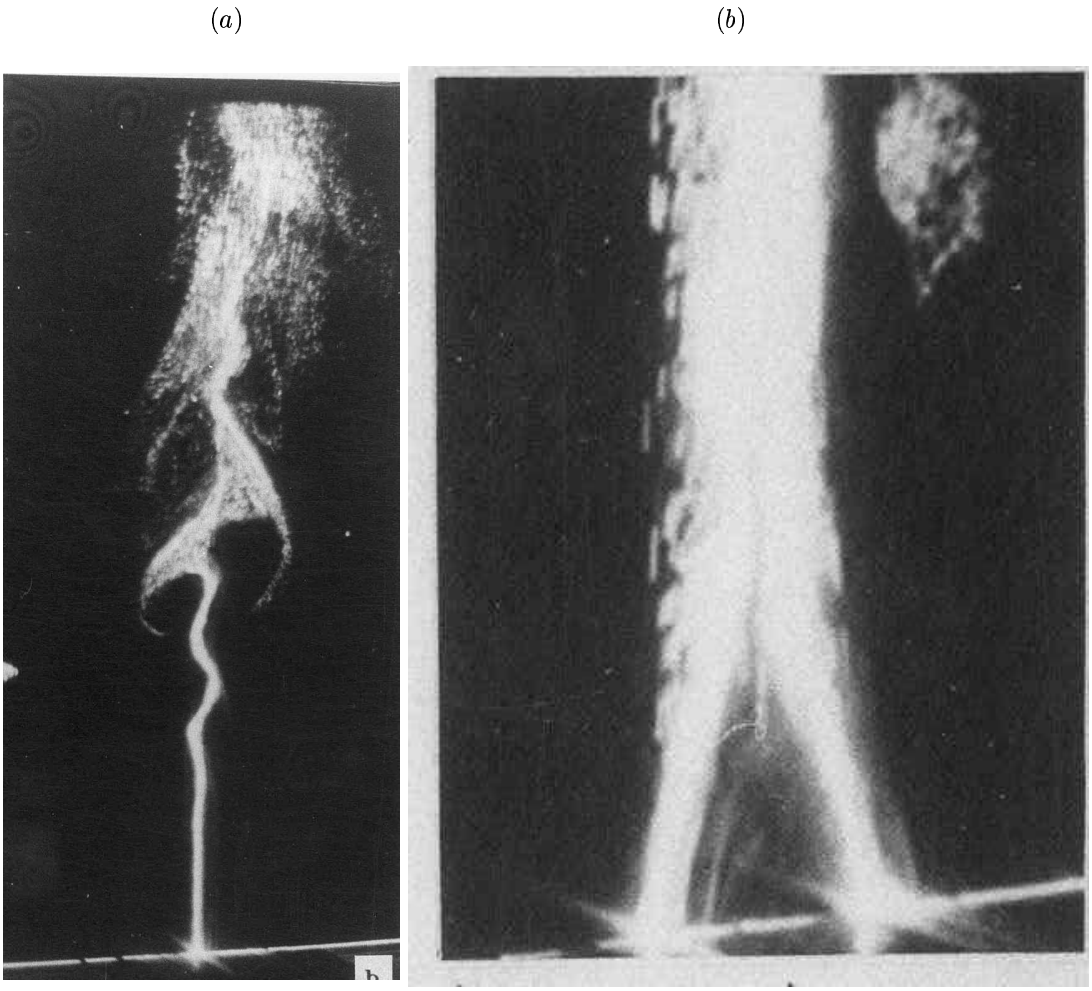

Figure 1: (a) Visualization of the core region of a plane bubble plume. Initially the plume is laminar, followed by transition to turbulence. The gas flow rate is 18.0×10^{-3} $mm^3/sec/mm$ of source length. (b) Visualization of interaction of two plane bubble plumes. The initial distance between two plumes is 33 mm. The gas flow rate is 21.6×10^{-3} $mm^3/sec/mm$ of source length.

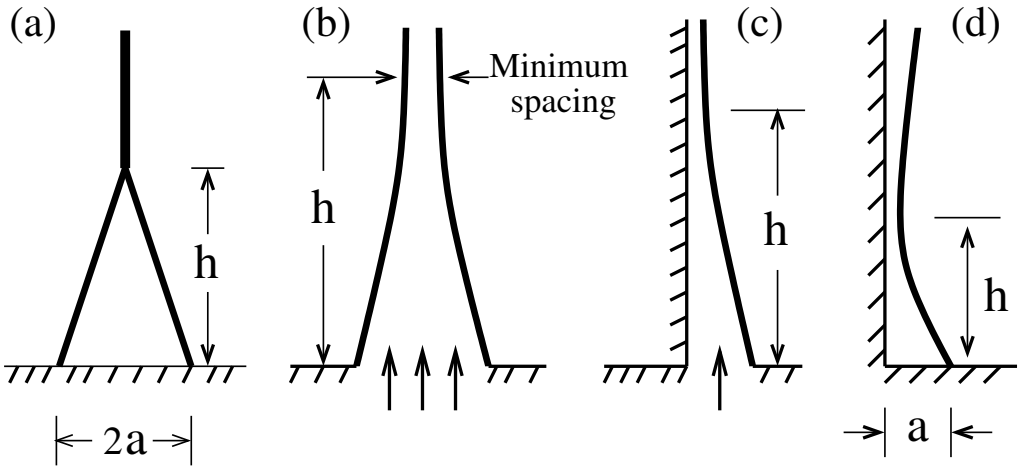

Figure 2: Schematic of various configurations used for bubble plume interaction studies.

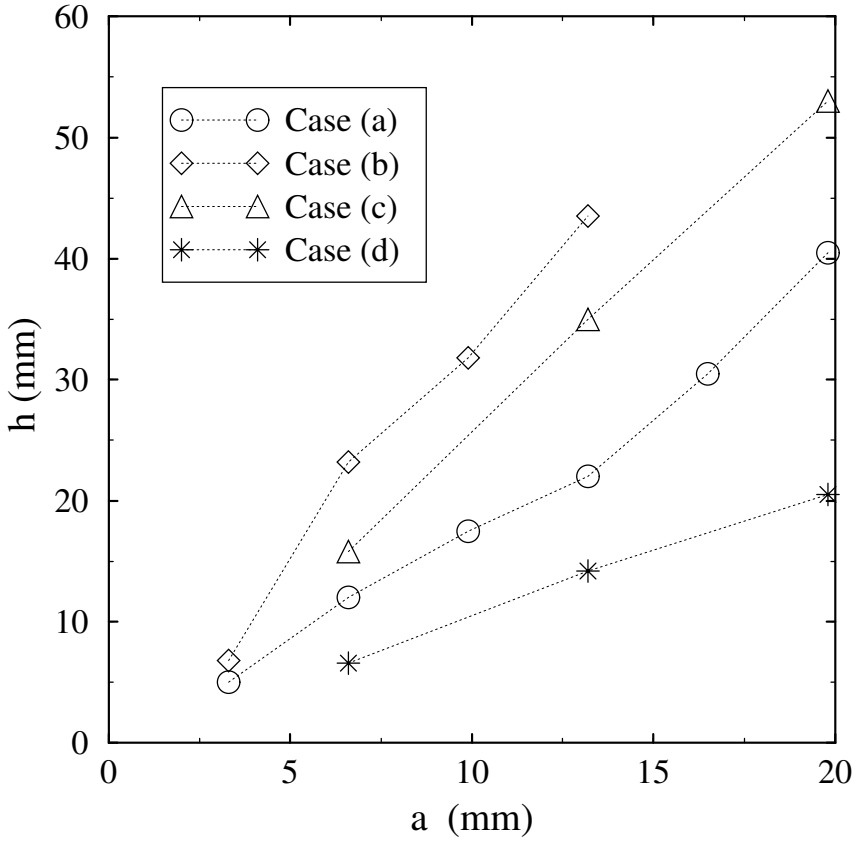

Figure 3: Comparison of interaction height, h, variation with spacing, a, for various combinations shown in Fig. 2. The gas flow rate per plume is 28.8×10^{-3} $mm^3/sec/mm$ of source length.

A. Experimentally observed streamline patterns.

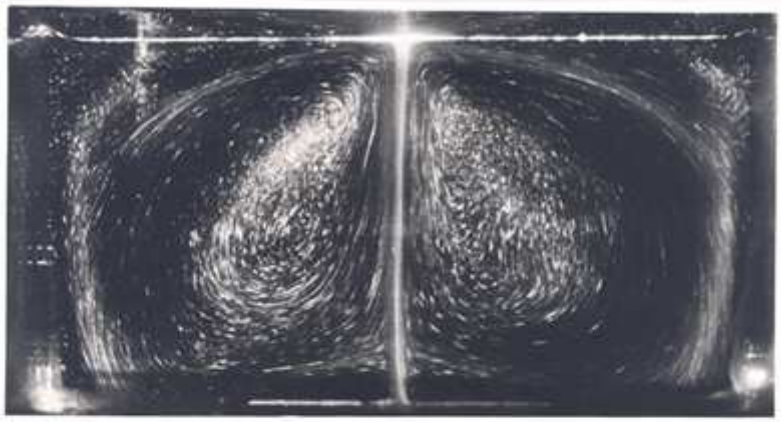

B. Computationally found streamline patterns.

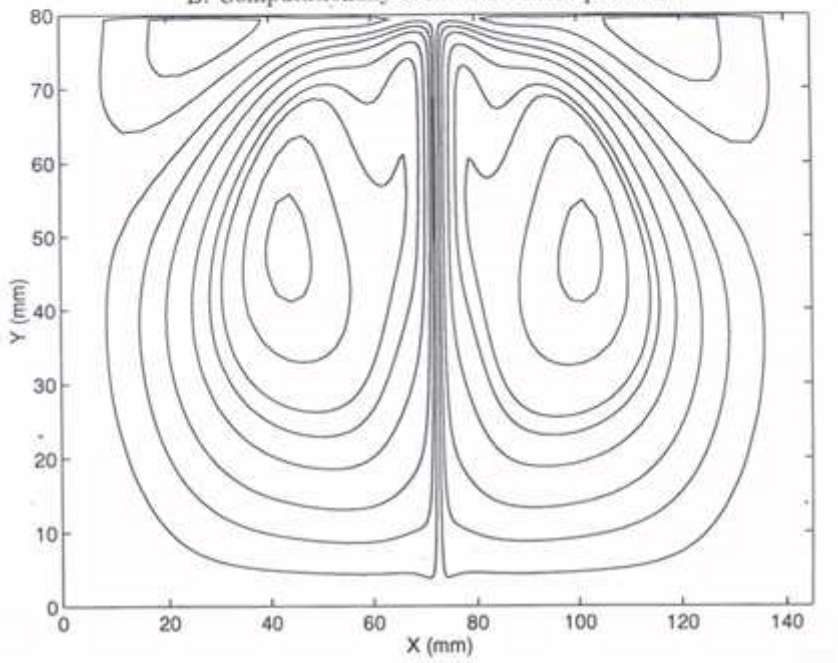

Figure 4: Comparison of observed (A) and computed streamline patterns (B) for a bubble curtain driven flow in a closed environment. The top surface is a free surface. The gas flow rate is $52.0 \times 10^{-3}\ mm^3/sec/mm$ of source length; the maximum predicted vertical velocity in the bubble plume is about 30 mm/sec.

Proceedings of the Tenth Asian Congress of Fluid Mechanics
17-21 May 2004, Peradeniya, Sri Lanka

THE IMPORTANCE OF INITIAL ATOMISATION OF A UREA SPRAY INJECTED INTO A DIESEL ENGINE EXHAUST TO THE FAR FIELD DROPLET FLUX DISTRIBUTION

M. I. Akbar, Y. Hardalupas and A. M. K. P. Taylor
Department of Mechanical Engineering, Imperial College London, London SW7 2BX, UK

B. Cumming, T. Taylor
Ford Motor Co., Basildon, Essex SS15 6EE, UK

ABSTRACT: One of the most effective NO_x aftertreatment technologies for Diesel engines is the Selective Catalytic Reduction (SCR) of NO_x gases using aqueous urea, which has very high NO_x conversion efficiencies. The urea decomposes within the exhaust to produce NH_3, which reacts with NO_x gases on the catalyst surface to produce nitrogen (N_2), water (H_2O). In order for the strategy to be effective, most, if not all of the urea needs to have evaporated and decomposed into NH_3 upstream of the catalyst, or a short distance within it. Hence the urea delivery system is of some importance, especially at the low exhaust temperatures (*i.e.* between 175°C and 250°C) experienced by light-duty vehicles, which are at the borderline of being able to evaporate all the droplets within practical lengths of an exhaust pipe. The aim of this study was to determine whether the unevaporated liquid flux reaching the catalyst, starting from an air assisted urea injection system, was uniquely influenced by the initial atomisation level close to the injector exit. Radial profiles of Sauter Mean Diameter (SMD) and flux were measured using a Phase Doppler Anemometer, 66 cm from the injector nozzle ("far field"), within the exhaust pipe for a gas temperature of about 175°C. Results showed that, at low urea flowrates (3 - 5 cc/min), a 12% reduction in flux-averaged SMD close to the injector exit, resulted in up to 68% lower liquid flux profiles just upstream of the catalyst. For higher flowrates (12.5 to 17.5 cc/min) the averaged SMD close to the injector exit no longer correlated with the unevaporated liquid flux close to the catalyst.

1 INTRODUCTION

Stringent future NO_x and PM emission regulations for Diesel vehicles are necessitating the use of exhaust aftertreatment strategies to meet the required standards [1, 2]. One of the most effective NO_x aftertreatment technologies is the Selective Catalytic Reduction (SCR) of NO_x gases, based on the spraying of aqueous urea to the Diesel exhaust, with demonstrations of more than 90% conversion efficiency [3, 4]. In this approach, also known as urea-SCR, the aqueous urea is injected, typically as an atomised spray, into the exhaust pipe, where it decomposes primarily into ammonia (NH_3) gas within the hot environment. So the amount of evaporation and subsequent decomposition of the urea determines the concentration of NH_3 available for SCR of NO_x. Equations 1 and 2 show the two main reaction pathways for the production of NH_3 from aqueous urea, the former pathway being the initial decomposition of urea and the latter being the hydrolysis of the isocyanic molecule produced from the reaction given in equation 1.

$$\underset{\text{(urea)}}{(NH_2)_2CO} \rightarrow NH_3 + \underset{\text{(isocyanic acid)}}{HNCO} \quad (1)$$

$$HNCO + H_2O \rightarrow NH_3 + CO_2 \quad (2)$$

The NH_3 then reacts with NO_x gases on the catalyst surface to produce nitrogen (N_2) and water (H_2O) vapour [5]. In order to ensure that there is an optimum level of NH_3 for the reduction process, and to prevent urea wastage and so-called NH_3 "slip" from the exhaust, it is necessary for most, if not all, of the urea to evaporate and decompose before reaching the upstream face of the catalyst surface or a short distance within the catalyst substrate. There have been many studies conducted to date on the reduction

mechanism involving the NH_3 and NO_x gases and the surface chemistry of the catalyst [6]. However, apart from brief mention during experimental descriptions, there are virtually no works in the literature that have investigated the actual urea delivery system itself, which is another important aspect of the system [7]. The method of delivery is likely to be critical at lower exhaust temperatures, since the largest droplets in the spray may not have enough residence time to evaporate completely in the relatively short distance between the injector and the catalyst substrate. The urea spraying strategy must be improved to aid in the overall evaporation, and subsequent decomposition, of the aqueous urea (It is well known that the evaporation time of an isolated droplet, at least, is proportional to the square of its diameter [8]. So the smaller the droplet, the faster it will evaporate. A basic mathematical model developed during this study, shows that it would take a 150 μm droplet approximately 0.8 seconds to evaporate completely at a temperature of 175^{o}C). The aim of this study was to determine whether the unevaporated liquid flux reaching the catalyst, starting from an air assisted urea injection system, was uniquely influenced by the initial atomisation close to the injector exit.

2 EXPERIMENTAL ARRANGEMENT AND TECHNIQUES

The details and numerical quantification of the following items and parameters are deliberately undisclosed to protect commercial confidentiality: the atomisation system and its operating conditions, the length of exhaust pipe test section, catalyst type, dimensional flux values, and molar concentration of the aqueous urea mixture.

Atomisation characterisations of the sprays, using the liquid volume flux and the Sauter Mean Diameter (SMD) of the droplets in the spray as response variables, for different operating conditions of an air assisted injection system, were conducted using a custom-built Phase Doppler Anemometer (PDA), capable of measuring single-point size-flux data. For spray measurements within the exhaust, the arrangement consisted of a 2.5 l naturally aspirated Diesel engine controlled by a dynamometer and connected to a precision drawn stainless steel exhaust pipe test section having an internal diameter of 47 mm and containing a commercial honeycomb SCR catalyst. The pipe test section and the PDA set-up, including a special movable optical window section, are shown schematically in figure 1 (a). Since the PDA was a single-point instrument, the radial profile of the droplet size-flux characteristics, along a horizontal line, was built up by measuring across the diameter of the exhaust pipe. Figure 1 (b) shows a photograph of the test section and figure 1(c) presents a schematic of the injector placement within the exhaust pipe. Spray measurements along the radial profiles were carried out 66 cm downstream of the nozzle exit (the so-called “far field”) at an average exhaust temperature of 175^{o}C. The specific measurement plane was chosen as the closest plane to the upstream face of the catalyst at which measurements were possible and the temperature because it was at the lower end of the “window” for the operation of urea-SCR.

Spray measurements in the ambient (*i.e.* unconfined by the exhaust pipe) were conducted close to the injector nozzle exit (20 mm downstream) to determine the structure of the spray, gain information into the initial level of atomisation (by measuring the SMD of the droplets), and subsequently compare and map, within the exhaust environment, the spray’s development from its initial stages to a plane close to the upstream catalyst face. The 20 mm measurement plane (the so-called “near field”) was selected because the PDA can size only spherical droplets accurately, and any plane closer to the atomiser than 20 mm did not show adequate liquid break-up and droplet formation for this to be the case. Since it was not possible to measure close to the nozzle exit within the exhaust pipe, the SMD information of each test from the *ambient* measurements at 20 mm were used to represent the initial spray distribution in the exhaust. It was assumed that there would be little difference between the ambient and exhaust spray structures at such a short distance from the nozzle.

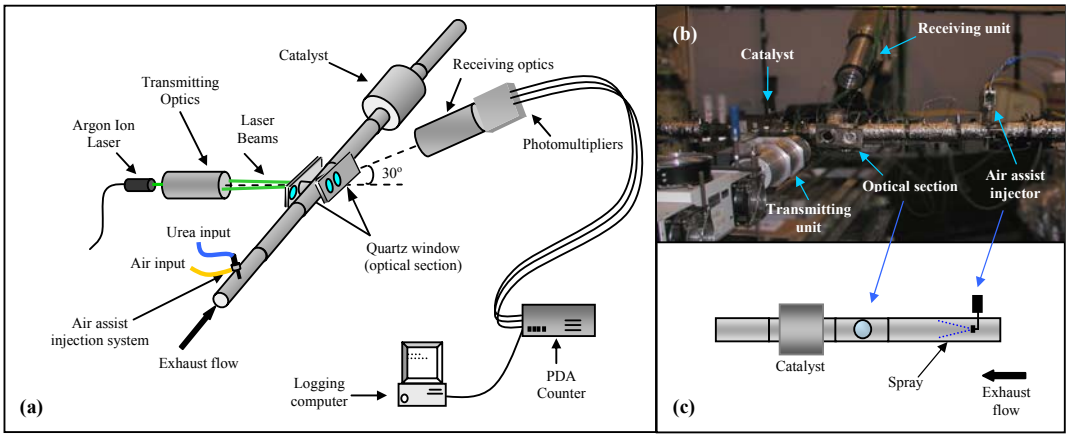

Figure 1: Experimental arrangement for PDA measurements within the Diesel exhaust (a), photograph of the test section (b), and schematic of the exhaust pipe showing the placement of the injector (c).

3 RESULTS AND DISCUSSION

While the tests were being conducted, some parameters (engine operating conditions, exhaust gas temperature, injector-type and fluids) were maintained nominally constant. The only variable parameters were the initial level of atomisation of the spray, altered by changing the air flowrate and the total urea flowrate. Henceforth the designation "ambient" refers to data gained during ambient spray tests 20 mm downstream of the injector nozzle, while "exhaust" refers to data gained during measurements within the exhaust pipe, 66 cm downstream of the injector nozzle. In all the graphs presented in this study, the values of the response variables at each point along the profile were based on 24,000 validated droplet measurements. Repeat measurements of tests, for the same nominal operating conditions, showed an average variation in the SMD of around 5%, while the flux was found to have a variation within 10% of the maximum value in the central region, *i.e.* away from regions of steep gradient in the profile.

The main spray dependent (or "response") variables considered during this investigation were the volume flux [9] of the spray (an indication of the liquid flowrate) normalised by the maximum value taken from all the flux profiles, and the SMD (a measure of the level of atomisation). Typical spray profiles for the normalised flux and SMD measured during *ambient* characterisation are shown in figure 2. The flux profile presents a solid cone spray structure, where the flux is largest around the central region of the spray.

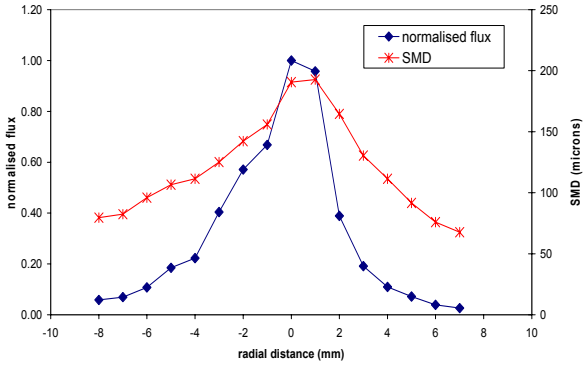

Figure 2: Normalised flux and SMD profiles typically measured during measurements 20 mm downstream of the nozzle exhausting into the ambient.

To analyse the importance of initial atomisation on far-field spray development relative to the effect of changing the total flowrate, normalised volume flux and SMD profiles for different operating conditions, measured within the exhaust, were selected for comparative study. Five cases are compared in this discussion, with the flux profiles being normalised by the maximum flux value in all five profiles. The first example presented below concerns two conditions, designated cases (a) and (b), which had the same aqueous urea flowrate (5 cc/min) but different ambient (near field) SMD profiles, produced here by varying the air flowrate in the injection system.

If the dominant effect were the total flowrate only, and the atomisation did not play a part in the structure and distribution of the spray profile by the "far" downstream station, then it could be expected that the normalised flux values would be similar for both cases since these had the same initial flowrate. However, there was a significant difference between cases (a) and (b) in figure 3, with a maximum difference of about 68%, indicating that some factor other than the flowrate was noticeably influencing the spray development. This factor is proposed to be the near field atomisation of the spray. For completeness, figure 4 shows the far field SMD profiles in the exhaust for the same test cases and also reveals clear differences in the SMD between the two conditions.

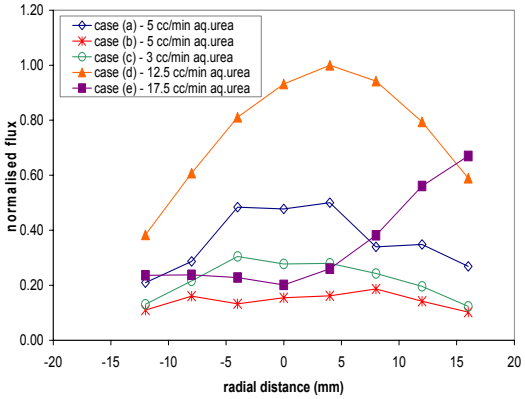

Figure 3: Comparison of normalised flux vs. radial distance for five tests cases, (a) to (c), measured 66 cm downstream of the nozzle under exhaust conditions.

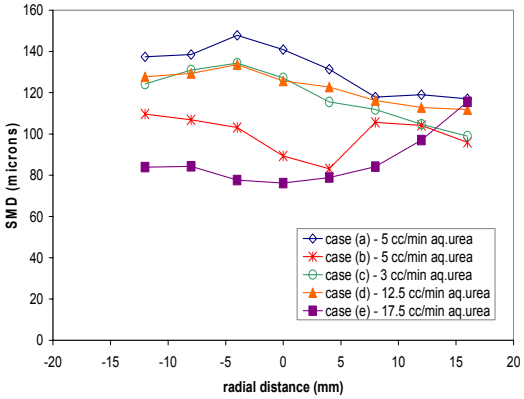

Figure 4: Comparison of SMD vs. radial distance for five tests cases, (a) to (c), measured 66 cm downstream of the nozzle under exhaust conditions.

The question arises as to whether there is a dependence of the far field in the exhaust to the near field "initial conditions" of atomisation. A convenient way to summarise the initial conditions is through the flux-weighted area-averaged SMD, given in equation 3, where G(r) and SMD (r) are the flux and SMD values at radial position 'r' from the centre of the exhaust pipe, of radius R.

$$AverageSMD = \overline{SMD} = \frac{\int_0^{+R} 2\pi\, rG(r)\, SMD(r)\, dr}{\int_0^{+R} 2\pi\, rG(r)\, dr} \qquad (3)$$

Note that the flux-weighted area-averaged value of SMD was expected to have a substantially smaller error than the 'raw' SMD measurement itself. The ambient and exhaust flux-weighted SMD values for case (a) were 142 and 126 μm, respectively, while for case (b) the corresponding average SMD values

were 125 and 101 μm, respectively. The case with the finer near field atomisation (*i.e.* the smaller SMD) had the lower flux distribution, thus indicating that the atomisation level *did* play a part in the droplet distribution profiles close to the upstream catalyst face.

We now consider another test case, case (c), which had a liquid urea flowrate of 3 cc/min. If only the flowrate was considered, this test condition could be expected to have a lower far field flux profile than both the distributions of the test cases measured at the higher flowrate. However, as seen in figure 3, the flux profile lay between those of cases (a) and (b), both associated with a 5 cc/min liquid flowrate. Once again, for completeness, the corresponding far field SMD profile is given in figure 4. The average values of SMD in ambient and exhaust conditions were 136 and 113 μm, respectively. Thus, at least for variations between 3 and 5 cc/min, it appears that the far field flux falls monotonically with reduction in the near field average SMD.

A third (and final) set of results consisted of comparing two tests having larger urea flowrates. Case (d) had a flowrate of 12.5 cc/min while case (e) had a flowrate of 17.5 cc/min (which was at the upper limit of the required urea dosing "window"). The flux and SMD profiles measured within the exhaust, close to the catalyst (i.e. 66 cm downstream of the nozzle), are also presented in figures 3 and 4, respectively. Ambient and exhaust flux-weighted SMD values for case (d) were 123 and 118 μm, respectively, while for case (e) the average SMD values were 96 and 104 μm, respectively. It is clear that the magnitude of the flux profile is no longer uniquely determined by the near field average SMD. Figure 3 does show case (d) to have a higher flux distribution than case (e), although the symmetry is poor in the latter case, with the flux rising on one side of the pipe (possibly due to an impediment of the nozzle causing an asymmetric spray). For cases (d) and (e), once again, the case having the lower of the two near field SMD profiles also had the lower far field flux profile. However, overall comparison between the high (*d* and *e*) and low (*a* to *c*) liquid flowrate cases shows that similar initial atomisation leads to different level of liquid flux close to the catalyst, which suggests that other factors became important. These factors could be (i) the change of the spray angle, leading to larger amount of liquid reaching the exhaust wall, (ii) the change in the droplet velocity, leading to different droplet residence times in the exhaust, (iii) the change of the liquid flowrate, leading to reduced gas temperature in the exhaust as the liquid requires more heat in order to evaporate. Experimental observation showed that a liquid film was present on the exhaust wall for high liquid flowrates, which is consistent with the expected contribution of the above factors.

Thus, as might be expected, the far field droplet flux distribution is certainly influenced by the initial atomisation of the spray. However, other factors, including the increase of the total liquid flowrate, are also important parameters. It is consistent with the results to expect that the flux distribution be determined by the fineness of the initial atomisation, but only for small changes in the flowrate.

4 CONCLUSIONS

To examine whether the spray flux profile at the catalyst face was uniquely influenced by the initial atomisation close to the injector exit, five sets of measurements were compared. The SMD profiles were measured within the exhaust manifold 66 cm downstream of the injector nozzle and, for flowrates between 3 and 5 cc/min, it was found that the sprays with the smaller initial average SMD led to a smaller far field flux profile. However, for higher flow rates, between 12.5 and 17.5 cc/min, it is clear that the far field flux depends not only on the initial average SMD but also on other factors.

These factors are likely to include the change in the spray angle, the droplet velocity and the influence of the liquid flow rate. The spray angle influences the amount of liquid reaching the exhaust pipe wall, the droplet velocity influences the residence time within the given length of the exhaust pipe and the increase of the liquid flow rate leads to a reduction in the gas temperature and hence a reduction in the evaporation rate.

ACKNOWLEDGEMENTS

The authors wish to acknowledge and thank the Ford Motor Co., Dunton, UK for providing the support and funding for this study, which was part of a larger project concerning urea-SCR systems for Diesel vehicles. Discussions with Robert Hammerle and his team at Ford Research Labs, Dearborn, MI, USA during the course of this research were also very beneficial and much appreciated.

REFERENCES

[1] California Environmental Protection Agency: Air Resources Board (2001). California Exhaust Emission Standards and Test Procedures for 2001, and Subsequent Model Passenger Cars, Light-Duty, and Medium-Duty Vehicles. *Public report,* 2001, California, USA.

[2] DieselNet. Emission Standards: European Union - Heavy Duty Diesel Truck and Bus Engines. *DieselNet: Engine and Emission Technologies online report,* 2001.

[3] Fritz N, Mathes W, Zuerbig J. On-Road Demonstration of NOx Emission Control for Diesel Trucks with $SINO_x$ Urea SCR System. *SAE Technical Paper Series 1999*, 1999-01-0111.

[4] Elsener M, Kleemann M, Koebel M. Urea-SCR: A Promising Technique to Reduce NOx Emissions from Automotive Diesel Engines. *Catalysis Today*, 2000, **59**: 335-345.

[5] Backes R, Hammerle RH, Horrocks RW, Hurley RG, Huthwohl G, Ketcher DA, Luders H. An Urea Lean NOx Catalyst System for Light Duty Diesel Vehicles. *SAE Paper,* 1995, 952493.

[6] Elsener M, Koebel M, Madia G. Reaction Pathways in the Selective Catalytic Reduction Process with NO and NO2 at Low Temperatures. *Ind. Eng. Chem. Res.,* 2001, **40**: 52-59.

[7] Calabrese JL, Davis GW, Grimston K, Patchett JA, Rice GW. The Influence of Injector Operating Conditions on the Performance of a Urea-Water Selective Catalytic Reduction (SCR) System. *SAE Technical Paper Series,* 2000, 2000-01-2814.

[8] Leferbrve AH. **Atomisation and Sprays.** Purdue University, Indiana, USA. Taylor and Francis Publishers, 1989.

[9] Hardalupas Y, Taylor AMKP. On the Measurement of Particle Concentration Near a Stagnation Point. *Exper. In Fluids*, 1989, **8**: 113-118.

Proceedings of the Tenth Asian Congress of Fluid Mechanics
17-21 May 2004, Peradeniya, Sri Lanka

BUBBLE FLOW THROUGH THE BRANCHING PIPE

H. Ishikawa
Department of Mechanical Engineering, Tokyo University of Science, Tokyo 162-8601, Japan

O. Mochizuki
Department of Mechanical Engineering, Toyo University, Kawagoe 350-8585, Japan

M. Kiya
Kushiro National College of Technology, Kushiro 084-0916, Japan

ABSTRACT: Bubble flow in the pipe causes flow unsteadiness, noise and vibration. Well-known bubble removal devices make use of the buoyant force. In this paper, it was described a phase separation phenomena of bubble flow through the branching pipe, which might be a potential of new bubble removal technique. Bubble behavior through the branching pipe in the air/water loop system was investigated experimentally by flow visualization. The microgravity experiment was also performed in free fall tower. The microgravity condition was convenient to study bubble flow because the buoyant force does not act on the bubble in pipe. As a result the distribution ratio of bubble between the main pipe and the branching pipe was varied depending on the bubble diameter. The number of bubbles flowed into the branching pipe increased as the bubble diameter increased. When the mean diameter of bubble was over 3.0mm, 80% of the bubbles flow into the branching pipe. This is because, a large bubble experiences the body force caused by favorable pressure gradient in the direction of the branching pipe. Therefore, bubble was subjected to suction in the branching pipe. This pressure gradient was caused by the flow separation from the corner of the branching pipe.

1. INTRODUCTION

Two-phase gas/liquid flow in a pipe can be classified into some different states according to void fraction. In the case of large void fraction, the flow pattern shows the slug flow which was consisted of a large bubble filling the pipe cross section and small bubbles. With decreasing of void fraction, the gas in flow posses the dispersive state – Bubble flow.

Bubble flow is often taken up as serious problem in many pipeline systems. Contamination with small amount of gas from cracks or gaps on the pipeline would be easily grew the large bubble in pipe flow. Especially bubbles in the pipeline systems, such as fuel, cooling water in plant and domestic water, might be cause flow unsteadiness, noise and vibration. It is expected to develop the special device for bubble removing using some phase separation technique. Well-known bubble removal device is the method of using the buoyant force. However, the buoyancy method requires other special devices to collect bubbles, such as a collecting tank. The occupied space for such devices is too large to install itself.

Interesting phase separation phenomena occurs when two phase flow flows through the branching pipe. Regarding air/water two phase flow in a pipe, Fabre & Liné[1] reviewed that the flow pattern of slug flow through the branching pipe was found to depend on the flow structure, such as separation and reattachment. Hwang et al.[2] investigated phase separation for impacting two-phase flow in T branching pipe experimentally. Fujii et al.[3] and Asano et al.[4] categorized the phase separation characteristic of gas/liquid flow in T- and Y-branching pipes. And Suu[5] studied experimentally the distribution ratio of N_2 gas and water phase in the branching pipe. Theoretically, Azzopardi et al.[6] proposed the simple model for prediction of behavior of two phase flow in impacting T branching pipe. Their model shows the good agreement with the experimental data.

In this study, behavior of bubble flow through the branching pipe, which has a 90 degrees junction, was investigated experimentally. The number of bubble flowed into the main pipe and the branching pipe respectively was observed by flow visualization. Experiments were also carried out under microgravity condition. Bubble doesn't experience any buoyant force under the microgravity condition. Therefore the bubble, passing through along the center of the pipe, was not affected the shearing stress on the wall. Bubbles were distributed in the main pipe and the branching pipe with different distribution ratio. It was

Fig.1: Air/water loop system

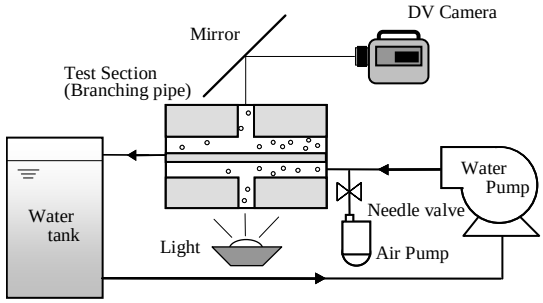

Fig.2 : Schematic diagram of the air/water loop system

founded that the bubble was subjected the drag and the pressure gradient in proportion to the bubble diameter. The pressure gradient was enhanced by flow separation from the corner of the branching pipe.

2. EXPERIMENTAL SETUP

Experimental air/water loop system is shown in Fig.1. This loop system has 90cm length, 43cm width and 40cm height. The total weight of this loop, including the water, was within 25kg. These dimensions are adapted to install in free fall capsule for the microgravity experiment, as described later. The schematic diagram of the air/water loop system is also shown in Fig.2. The loop system was composed mainly of the water pump, water tank, and branching pipes as test section. The branching pipe of 90 degrees was made of an acrylic resin to enable visualizing the bubble behavior. The bubble behavior was projected on the reflecting mirror, observing via the digital video camera. The branching pipe had a uniform cross section of its diameter was 2.0cm. The surface of inner wall of the pipe was finished smoothly. It should be noted that the branching pipe was set up horizontally to the gravity force. Hence, buoyant force doesn't act on bubble in the direction of the center axis of the main pipe and the branching pipe.

In order to except the buoyant force, the microgravity experiment has also carried out in free fall tower system. Under microgravity condition the bubbles flow through the center of the pipe without any buoyant force, the shearing stress on the wall doesn't affect the bubble behavior. The microgravity experiment was performed in the underground microgravity experiment center (JAMIC) in Kamisunagawa-cho, Hokkaido. The fall tower system of 710m in JAMIC provided the 10 seconds of microgravity condition.

The experimental procedure is described as follows; the water pump circulated the flow in the loop system. The uniform velocity of U was 0.30m/s. Reynolds number ($=UD/\nu$, ν: kinematic viscosity) was 6,000 and so the flow in the pipe was turbulent. The bubble supplied by the air pump was injected and flowed into the branching pipe. The injection timing of the bubbles was 10 seconds before the free fall onset. The mean diameter of bubble was controlled in the range of 0.1-3.0 mm by adjusting an air nozzle and a needle valve. The bubbles that once passed through the branching pipe were collected in the water tank. This loop was designed so that the traveling distance of the water loop would be long enough to prevent that any bubble has passed through the branching pipe again. The increment of internal pressure suppressed by air injection was suppressed at a constant by means of the pressure-regulating valve.

3. RESULTS AND DISCUSSION

Bubble behavior through the branching pipe under normal gravity and microgravity condition were respectively shown in Figure 3 and Figure 4. The flow direction is from left to right. That is, the flow

comes from the upstream main pipe, passing through the downstream main pipe and the branching pipe (upper part of the Figure 3). Under normal gravity condition, the gravity force act on negative direction of z-axis, which is the gravity force, does not act on the both direction of main and branching pipe. The time interval of each picture was 1/30 seconds. Bubble diameter was directly measured from these still

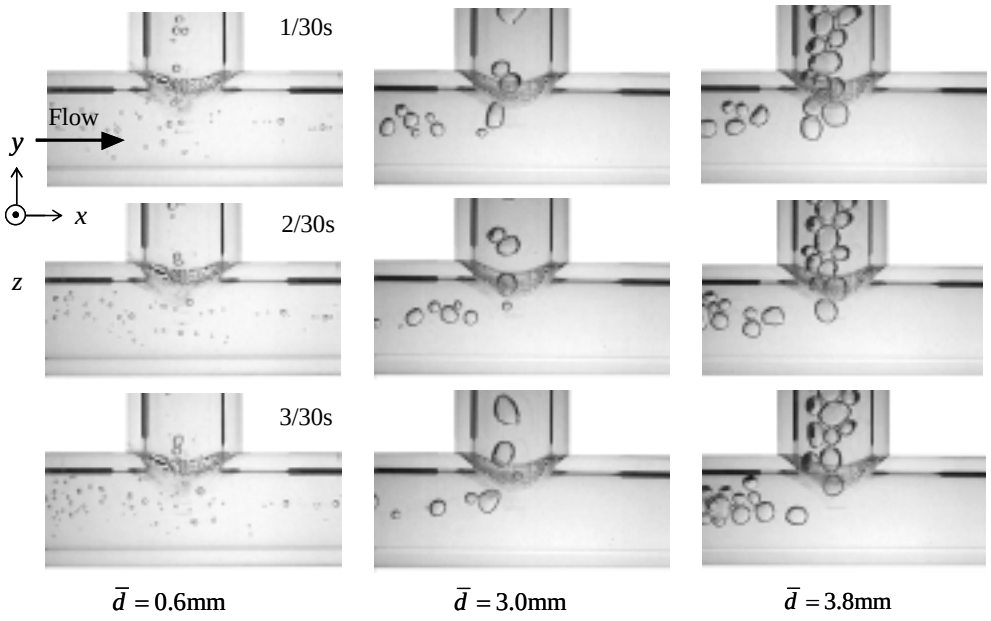

Fig .3:Bubble behavior in the branching pipe under normal gravity condition

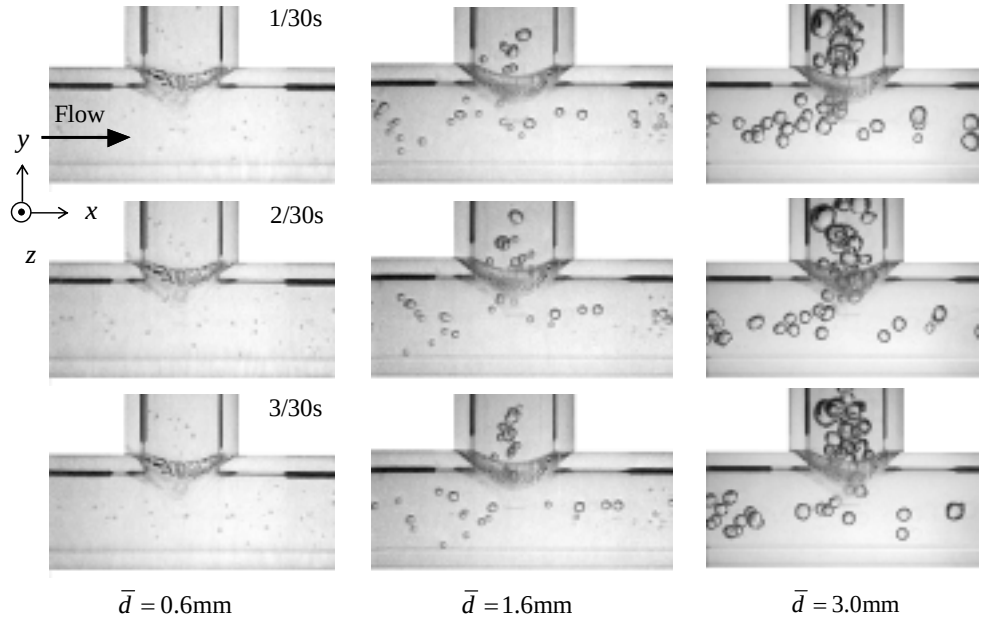

Fig. 4:Bubble behavior in the branching pipe under microgravity condition

pictures. In that case, the influence of the refraction didn't take into consideration in measuring the bubble diameter. There is still a room for improvement.

Under normal gravity condition, bubbles flowed into the main and branching pipe with different distribution ratio. The number of bubbles flowed into the branching pipe was increased as the mean diameter of the bubble $\bar{d}$ increased. This tendency was not remarkable under microgravity condition than normal gravity condition. When the mean bubble diameter $\bar{d}$ is larger than 3.0mm under normal gravity condition, almost all bubbles flowed into the branching pipe. The stagnation of bubble was observed at the corner where the flow separated in the branching pipe (not shown). These stagnating bubbles occasionally amalgamated each other and then flowed downstream. It suggests that bubble behavior was strongly depended on the flow structure in the branching pipe.

In order to confirm the flow structure in the branching pipe, the numerical simulation was performed by the computer code, FLUENT. Air/water two phase flow was solved by the Discrete Phase Model of FLUENT. The Algebraic Slip Mixture Model which can calculate the different velocities between two phases was adopted. Figure 5 shows the computational domain of the branching pipe. Its dimensions were the same as that used by the experiment. The number of three-dimensional unstructured mesh was about 131,700. Bubble diameter is set as 0.2, 1.0, and 2.0mm, and the void fraction at that time are 1.33×10^{-5}, 8.33×10^{-4}, and 6.67×10^{-3}, respectively.

Figure 6 shows *x*-, *y*- velocity and the static pressure distribution solved by FLUENT[7] simulation. This result is the single phase flow of only water. The accelerated region of *x*-velocity was observed on this side of the corner of the branching pipe. Bubble in the pipe appeared to be accelerated when passing through there. In the branching pipe section, there existed a reverse flow region which indicated low pressure. This low pressure region was developed by the flow separation from the corner of the branching pipe.

In accordance with the above numerical results, behavior of bubble flowed through the branching pipe could be explained as follows: bubble in the pipe is subjected both the drag force and the pressure force. The drag force by the main flow acts on the main pipe direction. On the other hand, there are two pressure forces caused by the adverse pressure gradient in the main pipe direction and the favorable pressure gradient in the branching pipe direction. The adverse pressure gradient acted on bubbles to push back upstream and the favorable pressure gradient sucked bubble for the branching pipe direction. Besides the favorable pressure gradient in the branching pipe was enhanced by the flow separation. These pressure forces are the body force proportional to the bubble's volume, i.e., these pressure force was more dominant for a large bubble than the drag force. Therefore, a large bubble is apt to flow into the branching pipe. Under normal gravity condition, bubble goes upward due to the buoyant force in the pipe, flowing adjacent to the upper inside wall of the pipe. Flow velocity was low because the boundary layer on the inside wall was not fully developed. In consequent, the drag force caused by main flow is

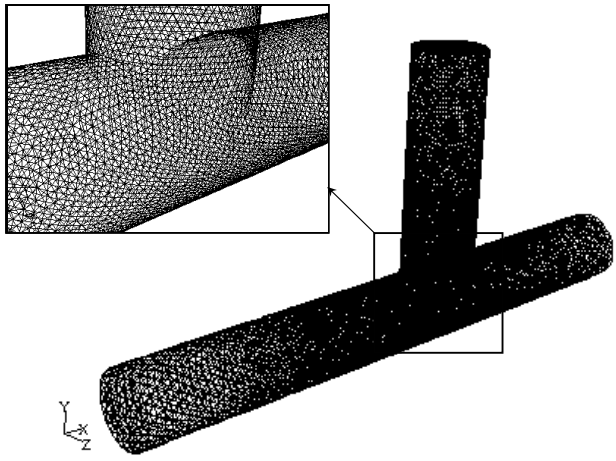

Fig.5:Computational domain of the branching pipe

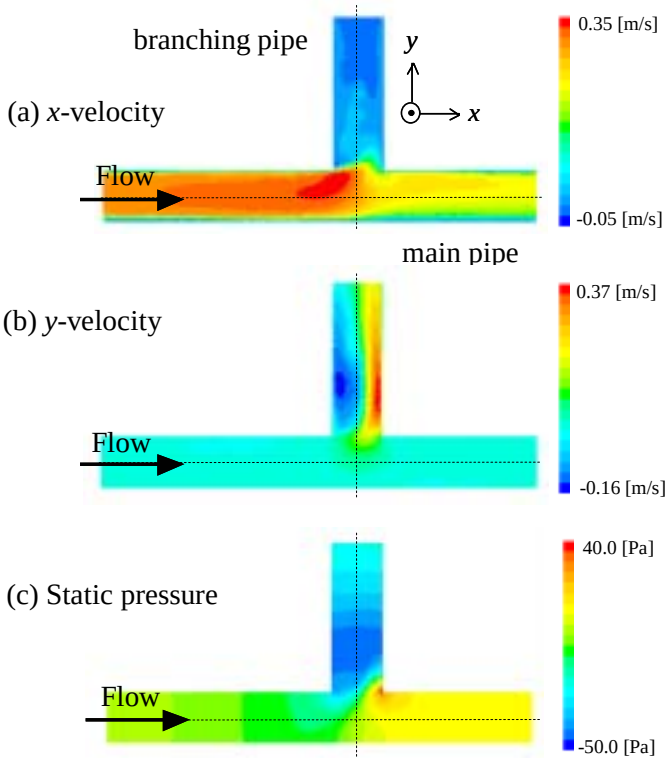

Fig.6 : *x*- and *y*-velocity and static pressure distributions by numerical simulation

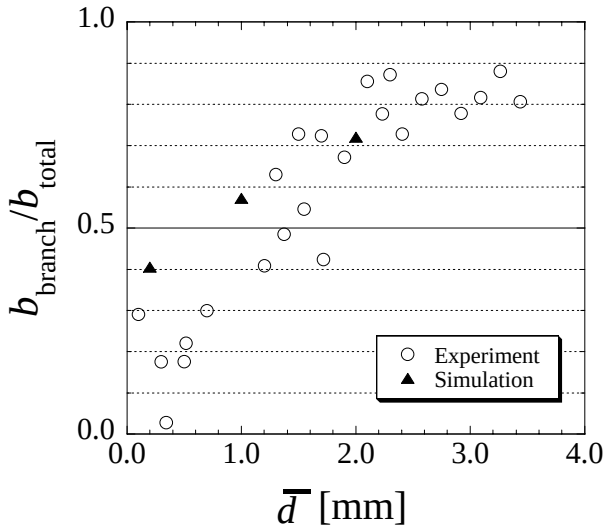

Fig.7: Distribution ratio of bubbles flowed into the branching pipe

further decreased; the pressure force in the branching pipe would be more dominant than that of under microgravity condition.

Figure 7 shows the distribution ratio of bubbles which flow into the main pipe and branching pipe. The vertical axis shows the distribution ratio of bubbles flowed into the branching pipe to all bubbles. In

the case of experiment, the number of bubbles was directly counted from the still pictures as shown in Fig. 3. It is interested that the bubble flowed into the branching pipe is increased as the bubble diameter increased. When the mean diameter of bubble $\bar{d}$ was over 3.0mm, 80% of bubbles flow into the branching pipe. Numerical result shows the agreement with the experimental results.

4. CONCLUSIONS

Bubble flow through the branching pipe was investigated under normal gravity and microgravity condition. Undergoing the pressure gradient enhanced by flow separation, large bubble which diameter was over 3.0 mm is apt to flow into the branching pipe in our experimental condition. It was found that bubble flow could be separate into air and water phase just using the branching pipe. It would be possible to develop a new bubble removal device, which has a simplified form without buoyant force. If some kind of another device forming a large bubble was installed before this side of the branching pipe, this method could be apply for the bubbles in the all range of diameter.

ACKNOWLEDGMENT

This research was supported in a part of a research-aid fund for a short time microgravity experiments. We wish to express our thanks Hokkaido Aerospace Science and Technology Incubation Center (formerly Hokkaido Microgravity Research Society) for their help.

REFERENCES

[1] Fabre, J. and Liné, A.: Modeling of Two-Phase Slug Flow. *Ann. Rev. Fluid Mech.*, Vol.24, 21-46, 1992.

[2] Hwang, S.T., Soliman, H.M. and Lahey Jr, R.T.: Phase Separation in Impacting Wyes and Tees. *Int.J.Multiphase Flow*, Vol.15 (6),965-975, 1989.

[3] Fujii, T., Nakazawa, T. Asano, H. Takenaka, N. and Yamada, H.: Characteristics of Phase Separation for Gas-Liquid Two-Phase Flow Using an Impacting T-Junction. *Tans. JSME*, Vol.62 (594), 447-453, 1996.

[4] Asano, H., Fujii, T., Takenaka, N. and Sakoda, K.: A Study of the Phase Separation Characteristics in Gas-Liquid Two-Phase Flows by an Impacting Y-Junction. *Tans. JSME*, Vol.67 (654), pp.350-355, 2001

[5] Suu T.:Air-Water Two-Phase Flow through a Pipe Junction (Experiment on the Local Void Fraction Distribution Adjacent to the Branching Part). *Tans. JSME*, Vol.54 (508), pp.3521-3528, 1988

[6] Azzopardi, B.J., Purvis, A. and Govan A.H.: Annular Two-Phase Flow Split at an Impacting T. *Int.J.Multiphase Flow*, Vol.13(5),605-614,1987.

[7] Fluent Inc:FLUENT 5 Documentation,1992.

Proceedings of the Tenth Asian Congress of Fluid Mechanics
17-21 May 2004, Peradeniya, Sri Lanka

TIDAL HARMONIC ANALYSIS AND PREDICTION

J.-J. Shu
School of Mechanical & Production Engineering, Nanyang Technological University
50 Nanyang Avenue, Singapore 639798

ABSTRACT: An efficient algorithm of tidal harmonic analysis and prediction is presented in this paper. Some conditions are found by means of the known approximate relationships between the harmonic constants of the tidal constituents. A system of linear equations for least square solutions under these restricted conditions is obtained. In the case of inadequate data, ill conditioning in the system of equations that has appeared in other algorithms is conveniently avoided. In solving the resultant normal equations, the Goertzel iteration is adopted so that the whole computation time is dramatically reduced.

1. INTRODUCTION

Tides and tidal currents offer clean and inexhaustible energy sources. Better prediction and analysis of tides and tidal currents are crucial to utilize hydro-dams more efficiently as energy generators. Tides are cyclic variations in the level of seas and oceans, while tidal currents are cyclic variations in the motion of seas and oceans. The present understanding of tides and tidal currents as natural phenomena due to the gravitational forces of the sun and moon acting on a rotating earth came from the development of Newton's gravitation theory[10]. Harmonic techniques were first used to analysis and predict tides and tidal currents by Thomson[12] and expended by Darwin[4], Harris[9] and Doodson[5]. Tides and tidal currents may be considered as the sum of tidal constituents according to harmonic analysis. With the development of digital computers, least squares technique is used to evaluate the tidal constituents from observed data and this is a principal method used today.

The harmonic method of tidal analysis has been further refined for improvement in accuracy of tidal prediction. A method for superfine resolution of tidal harmonic constituents has been developed by Amin[1-3] adding a corrective step into the harmonic method. The species concordance method has been developed by George & Simon[7] and Simon[11] using relationships between species of the tide at the studied station and at a reference station where the tide is well known or easily predicted. Here we reexamine the harmonic method from a practical point of view and propose an efficient algorithm of tidal harmonic analysis and prediction.

2. HARMONIC METHOD FOR REGULAR OBSERVATIONS

Let us consider real-time regular observed data of tidal height $h_n = h(t_0 + n\Delta T)\ (n = 0,1,\cdots,2N)$, where t_0 is the initial time, $2N+1$ is the number of the real-time observed data, and ΔT is the sampling time interval. The tidal height can be expressed as a sum of cosine functions plus random errors denoted by $r_n = r(t_0 + n\Delta T)$.

$$h_n = x_0 + \sum_{m=1}^{M} R_m \cos\left[\sigma_m\left(t_0 + n\Delta T\right) - \varphi_m\right] + r_n, \quad n = 0,1,\cdots,2N \tag{1}$$

where

$$R_m = f_m H_m,\ \varphi_m = g_m - \chi_m,\quad m = 1,2,\cdots,M.$$

x_0, f_m, H_m, σ_m, g_m, and χ_m are the mean tidal height, node factor, mean amplitude, angular velocity, epoch, and astronomical argument of the *m*th tidal constituent, respectively. M is the number of tidal constituents.

Eq. (1) can be rewritten as

$$h_n = x_0 + \sum_{m=1}^{M} \{x_m \cos[(n-N)\sigma_m \Delta T] + y_m \sin[(n-N)\sigma_m \Delta T]\} + r_n, \quad n = 0,1,\cdots,2N, \tag{2}$$

where

$$\{x_m, y_m\} = R_m \{\cos[\varphi_m - \sigma_m (t_0 + N\Delta T)], \sin[\varphi_m - \sigma_m (t_0 + N\Delta T)]\}$$
$$m = 1,2,\cdots,M.$$

Letting $\sigma_0 = 0$ and using matrix notation, Eq. (2) can be expressed as

$$R = H - QZ \tag{3}$$

where

$$R = \left(\frac{r_0}{\sqrt{2}}, r_1, \cdots, r_{2N-1}, \frac{r_{2N}}{\sqrt{2}}\right)^T, \quad H = \left(\frac{h_0}{\sqrt{2}}, h_1, \cdots, h_{2N-1}, \frac{h_{2N}}{\sqrt{2}}\right)^T.$$

$Z^T = (X^T, Y^T)$, and $X^T = (x_0, x_1, \cdots, x_M)$, $Y^T = (y_1, y_2, \cdots, y_M)$. The column vectors of the coefficient matrix Q are

$$Q_0, Q_1, \cdots, Q_{2M},$$

where

$$Q_m^T = (\frac{1}{\sqrt{2}}\cos[-N\sigma_m \Delta T], \cos[-(N-1)\sigma_m \Delta T], \cdots, \cos[(N-1)\sigma_m \Delta T], \frac{1}{\sqrt{2}}\cos[N\sigma_m \Delta T]),$$
$$m = 0,1,\cdots,M,$$

$$Q_m^T = (\frac{1}{\sqrt{2}}\sin[-N\sigma_m \Delta T], \sin[-(N-1)\sigma_m \Delta T], \cdots, \sin[(N-1)\sigma_m \Delta T], \frac{1}{\sqrt{2}}\sin[N\sigma_m \Delta T]),$$
$$m = M+1, M+2, \cdots, 2M.$$

We make

$$\|R\|_2^2 = \|H - QZ\|_2^2 = \min,$$

where $\|R\|_2$ is an Euclidean norm of R. Then

$$\frac{\partial \|R\|_2^2}{\partial x_0} = \frac{\partial \|R\|_2^2}{\partial x_m} = \frac{\partial \|R\|_2^2}{\partial y_m} = 0, \quad m = 1,2,\cdots,M.$$

That is

$$Q^T Q Z = Q^T H. \tag{4}$$

We arrive at

$$Q^T Q = \begin{bmatrix} F & O \\ O & G \end{bmatrix}, \quad Q^T H = \begin{bmatrix} C \\ S \end{bmatrix},$$

where

$$F_{lm}=\frac{1}{2}\left\{\frac{\sin\left[N(\sigma_l-\sigma_m)\Delta T\right]}{\tan\left[\frac{1}{2}(\sigma_l-\sigma_m)\Delta T\right]}+\frac{\sin\left[N(\sigma_l+\sigma_m)\Delta T\right]}{\tan\left[\frac{1}{2}(\sigma_l+\sigma_m)\Delta T\right]}\right\},\quad l,m=0,1,\cdots,M,$$

$$G_{lm}=\frac{1}{2}\left\{\frac{\sin\left[N(\sigma_l-\sigma_m)\Delta T\right]}{\tan\left[\frac{1}{2}(\sigma_l-\sigma_m)\Delta T\right]}-\frac{\sin\left[N(\sigma_l+\sigma_m)\Delta T\right]}{\tan\left[\frac{1}{2}(\sigma_l+\sigma_m)\Delta T\right]}\right\},\quad l,m=1,2,\cdots,M.$$

$$C_l=\frac{1}{2}\sum_{n=1}^{2N}\left\{h_{n-1}\cos\left[(n-1-N)\sigma_l\Delta T\right]+h_n\cos\left[(n-N)\sigma_l\Delta T\right]\right\},\quad l=0,1,\cdots,M, \tag{5}$$

$$S_l=\frac{1}{2}\sum_{n=1}^{2N}\left\{h_{n-1}\sin\left[(n-1-N)\sigma_l\Delta T\right]+h_n\sin\left[(n-N)\sigma_l\Delta T\right]\right\},\quad l=1,2,\cdots,M. \tag{6}$$

Therefore Eq. (4) can be decomposed into two linear equations

$$FX=C,\quad GY=S. \tag{7}$$

The accuracy of tidal prediction can be improved as longer data time series are analyzed and more tidal constituents are selected in Eq. (7).

3. ITERATING ALGORITHM FOR COMPUTING C AND S

In terms of complex form

$$C_l+iS_l=\frac{1}{2}\sum_{n=1}^{2N}\left\{h_{n-1}e^{i(n-1-N)\sigma_l\Delta T}+h_n e^{i(n-N)\sigma_l\Delta T}\right\}\quad l=1,2,\cdots,M. \tag{8}$$

Using Goertzel iteration[8],

$$\begin{cases}\rho_k=h_k+2\rho_{k+1}\cos(\sigma_l\Delta T)-\rho_{k+2}\quad k=2N-1,2N-2,\cdots,1\\ \rho_0=\dfrac{h_0}{2}+2\rho_1\cos(\sigma_l\Delta T)-\rho_{2,}\end{cases} \tag{9}$$

under initial conditions

$$\rho_{2N+1}=0,\ \rho_{2N}=\frac{h_{2N}}{2}.$$

After $2N$ time iterations, whence

$$C_l+iS_l=\left(\rho_0-\rho_1 e^{-i\sigma_l\Delta T}\right)e^{-iN\sigma_l\Delta T}. \tag{10}$$

In this method, only $2N$ multiplications are needed.

4. HARMONIC METHOD FOR SEGMENTS OF REGULAR OBSERVATIONS

For K equal-length segments of observed data (overlapping is allowed). $h_n^{(k)}(n=0,1,\cdots,2N,\ k=1,2,\cdots,K)$ are observations starting at time $t_0^{(k)}$ in kth segment. The corresponding random errors are $r_n^{(k)}$. For each segment, the same M is chosen. The corresponding R and H have

$$\overline{R}_k = \left(\frac{r_0^{(k)}}{\sqrt{2}}, r_1^{(k)}, \cdots, r_{N-1}^{(k)}, \frac{r_N^{(k)}}{\sqrt{2}} \right)^T, \overline{H}_k = \left(\frac{h_0^{(k)}}{\sqrt{2}}, h_1^{(k)}, \cdots, h_{N-1}^{(k)}, \frac{h_N^{(k)}}{\sqrt{2}} \right)^T \quad k = 1,2,\cdots,K.$$

Then

$$\overline{R} = \overline{H} - \overline{Q} W \overline{Z}, \tag{11}$$

where

$$\overline{R}^T = (\overline{R}_1^T, \overline{R}_2^T, \cdots, \overline{R}_K^T), \quad \overline{H}^T = (\overline{H}_1^T, \overline{H}_2^T, \cdots, \overline{H}_K^T).$$

For $\overline{Z}^T = (\overline{X}^T, \overline{Y}^T)$, the components of $\overline{X}$ and $\overline{Y}$ are

$$\begin{gathered} \overline{x}_0^{(k)} = x_0^{(k)}, \\ \left\{ \overline{x}_m^{(k)}, \overline{y}_m^{(k)} \right\} = R_m^{(k)} \left\{ cos\left(\varphi_m^{(k)} - N\sigma_m \Delta T \right), sin\left(\varphi_m^{(k)} - N\sigma_m \Delta T \right) \right\}, \quad m = 1,2,\cdots,M. \end{gathered} \tag{12}$$

$$\overline{Q} = \begin{bmatrix} Q & & & \\ & Q & & \\ & & \ddots & \\ & & & Q \end{bmatrix}$$

is a $[(2N+1)K] \times [(2M+1)K]$ matrix.

$$W^T = [W_1, W_2, \cdots, W_K], \tag{13}$$

where

$$W_k = \begin{bmatrix} U_1^{(k)} & U_3^{(k)^T} \\ -U_3^{(k)} & U_2^{(k)} \end{bmatrix}, \quad k = 1,2,\cdots,K,$$

and

$$\begin{gathered} U_1^{(k)} = \mathrm{diag}\left[1, \cos\left(t_0^{(k)} \sigma_1 \right), \cdots, \cos\left(t_0^{(k)} \sigma_M \right) \right], \\ U_2^{(k)} = \mathrm{diag}\left[\cos\left(t_0^{(k)} \sigma_1 \right), \cos\left(t_0^{(k)} \sigma_2 \right), \cdots, \cos\left(t_0^{(k)} \sigma_M \right) \right], \\ U_3^{(k)} = \begin{bmatrix} 0 & \sin\left(t_0^{(k)} \sigma_1 \right) & & & \\ 0 & & \sin\left(t_0^{(k)} \sigma_2 \right) & & \\ \vdots & & & \ddots & \\ 0 & & & & \sin\left(t_0^{(k)} \sigma_M \right) \end{bmatrix}. \end{gathered}$$

From

$$\left\| \overline{R} \right\|_2^2 = \left\| \overline{H} - \overline{Q} W \overline{Z} \right\|_2^2 = \min, \tag{14}$$

we have the normal equations

$$A\overline{Z} = P, \tag{15}$$

where

$$A = \sum_{k=1}^{K} \begin{bmatrix} U_1^{(k)} F U_1^{(k)} + U_3^{(k)^T} G U_3^{(k)} & U_1^{(k)} F U_3^{(k)^T} - U_3^{(k)^T} G U_2^{(k)} \\ U_3^{(k)} F U_1^{(k)} - U_2^{(k)} G U_3^{(k)} & U_3^{(k)} F U_3^{(k)^T} + U_2^{(k)} G U_2^{(k)} \end{bmatrix},$$

and $P^T = \left(\overline{C}^T, \overline{S}^T \right)$. The components of $\overline{C}$ and $\overline{S}$ are

$$\overline{C}_l = \frac{1}{2}\sum_{k=1}^{K}\sum_{n=1}^{2N}\left\{h_{n-l}^{(k)}\cos\left[\left(n-1-N+\frac{t_0^{(k)}}{\Delta T}\right)\sigma_l\Delta T\right]+h_n^{(k)}\cos\left[\left(n-N+\frac{t_0^{(k)}}{\Delta T}\right)\sigma_l\Delta T\right]\right\} \qquad l=0,1,\cdots,M,$$

$$\overline{S}_l = \frac{1}{2}\sum_{k=1}^{K}\sum_{n=1}^{2N}\left\{h_{n-l}^{(k)}\sin\left[\left(n-1-N+\frac{t_0^{(k)}}{\Delta T}\right)\sigma_l\Delta T\right]+h_n^{(k)}\sin\left[\left(n-N+\frac{t_0^{(k)}}{\Delta T}\right)\sigma_l\Delta T\right]\right\} \qquad l=1,2,\cdots,M.$$

5. CONSTRAINED CONDITIONS FOR INADEQUATE OBSERVED DATA

In the circumstances of analyzed data with insufficient-length (manly tidal currents), the tidal constituents cannot be separated effectively due to ill conditioning appeared in Eqs. (7) and (15). Some constrained conditions must be provided.

For two tidal constituents, we have the following relationship proposed by Dronkers[6]

$$\begin{aligned} F_{2j-1} &: \bar{x}_{2j-1} - \alpha_{2j-1,2j}\left(\bar{x}_{2j}\cos\theta_{2j-1,2j} + \bar{y}_{2j}\sin\theta_{2j-1,2j}\right) = 0, \\ & \qquad\qquad j = 1,2,\cdots,J, \\ F_{2j} &: \bar{y}_{2j-1} - \alpha_{2j-1,2j}\left(\bar{y}_{2j}\cos\theta_{2j-1,2j} - \bar{x}_{2j}\sin\theta_{2j-1,2j}\right) = 0, \end{aligned} \tag{16}$$

where J is the number of couples of tidal constituents to be chosen among the M tidal constituents. $\alpha_{2j-1,2j}$ and $\theta_{2j-1,2j}$ are functions of j. In matrix notation, Eq. (16) can be expressed as

$$B\overline{Z} = 0, \tag{17}$$

$$B = \begin{bmatrix} D_1 & & & \overbrace{0 \;\; 0 \;\; \cdots \;\; 0}^{(M+1)K-2J} & E_1 & & & \overbrace{0 \;\; 0 \;\; \cdots \;\; 0}^{MK-2J} \\ & D_2 & & 0 \;\; 0 \;\; \cdots \;\; 0 & & E_2 & & 0 \;\; 0 \;\; \cdots \;\; 0 \\ & & \ddots & \vdots \;\; \vdots \;\; \cdots \;\; \vdots & & & \ddots & \vdots \;\; \vdots \;\; \cdots \;\; \vdots \\ & & D_J & 0 \;\; 0 \;\; \cdots \;\; 0 & & & E_J & 0 \;\; 0 \;\; \cdots \;\; 0 \end{bmatrix},$$

where

$$D_j = \begin{bmatrix} 1 & -\alpha_{2j-1,2j}\cos\theta_{2j-1,2j} \\ 0 & \alpha_{2j-1,2j}\sin\theta_{2j-1,2j} \end{bmatrix}, \; E_j = \begin{bmatrix} 0 & -\alpha_{2j-1,2j}\sin\theta_{2j-1,2j} \\ 1 & -\alpha_{2j-1,2j}\cos\theta_{2j-1,2j} \end{bmatrix}, \quad j = 1,2,\cdots,J.$$

If taking

$$\left\|\overline{R}\right\|_2^2 + \sum_{j=1}^{2J}\lambda_j F_j = \min,$$

we can get the linear equations

$$\begin{bmatrix} A & B^T \\ B & O \end{bmatrix}\begin{bmatrix} \overline{Z} \\ \Lambda \end{bmatrix} = \begin{bmatrix} P \\ O \end{bmatrix}, \tag{18}$$

where the vector of LaGrange multiplier is

$$\Lambda = \left(\lambda_1, \lambda_2, \cdots, \lambda_{2J}\right)^T.$$

In order to eliminate unknown Λ in Eq. (18), we take

$$B^* = \begin{bmatrix} \overbrace{\begin{matrix} D_1^* & & & & & & \\ & D_2^* & & & & & \\ & & \ddots & & & & \\ & & & D_J^* & & & \\ & & & & 1 & & \\ & & & & & 1 & \\ & & & & & & \ddots \end{matrix}}^{(M+1)K} & \overbrace{\begin{matrix} E_1^* & & & & \\ & E_2^* & & & \\ & & \ddots & & \\ & & & E_J^* & \\ & & & & \end{matrix}}^{MK} \\ \begin{matrix} & & & & & & 1 \end{matrix} & \begin{matrix} & & & & \\ & & & & \\ & & & & \\ & & & & \\ & & & & \\ & & & & \ddots \\ & & & & & & 1 \end{matrix} \end{bmatrix},$$

where

$$D_j^* = \begin{bmatrix} 1 & \alpha_{2j-1,2j}^{-1}\cos\theta_{2j-1,2j} \\ 0 & -\alpha_{2j-1,2j}^{-1}\sin\theta_{2j-1,2j} \end{bmatrix},\ E_j^* = \begin{bmatrix} 0 & \alpha_{2j-1,2j}^{-1}\sin\theta_{2j-1,2j} \\ 1 & \alpha_{2j-1,2j}^{-1}\cos\theta_{2j-1,2j} \end{bmatrix},\quad j = 1,2,\cdots,J.$$

Taking advantage of $B^*B^T = O$, we have

$$\begin{bmatrix} B^* & O \\ O & I \end{bmatrix}\begin{bmatrix} A & B^T \\ B & O \end{bmatrix}\begin{bmatrix} \overline{Z} \\ \Lambda \end{bmatrix} = \begin{bmatrix} B^*P \\ O \end{bmatrix},$$

where I is unit matrix. Now the rank of matrix equation Eq. (18) is reduced by an equivalent form

$$\begin{bmatrix} B^*A \\ B \end{bmatrix}\overline{Z} = \begin{bmatrix} B^*P \\ O \end{bmatrix}. \tag{19}$$

6. CONCLUDING REMARKS

The least square method has broadly been adopted in tidal harmonic analysis. For a concrete problem using a computer, a better algorithm not only requests a less computing time but also is able to identify effectively the tidal constituents from observed data. An efficient algorithm of tidal harmonic analysis and prediction is presented here. It is the algorithm that can calculate coefficients of normal equations very simply and efficiently. To compute the right-hand terms of the normal equations, Goertzel iteration[8] is adopted to accomplish whole calculation processes quickly and accurately. In order to handle the segments of the observed date (mainly adapted to analyze tidal currents), a general algorithm for K sets of real-time regularly observed date in equal observing length can be derived from above results.

If the above algorithm is used to analyze the tidal constituents, the total analyzed data must have sufficient length. Otherwise ill conditioning in the system of equations appears so that conventional algorithm cannot separate tidal constituents effectively. Consequently in the circumstances of insufficient data (manly tidal currents), some constrained conditions can be established based on known approximate relationships among the harmonic constants of the tidal constituents. Then the lease squares solutions can be obtained from these constrained conditions. To various circumstances, the resultant linear equations can be deduced from this algorithm in order to avoid appropriately the emergence of ill conditioning. Because the

constrained conditions can reasonably be established, usually final solutions do not have to be corrected so that the harmonic constants can be determined with sufficient accuracy.

REFERENCES

[1] Amin M: The fine resolution of tidal harmonics. *Geophysical Journal of the Royal Astronomical Society*, 1976, **44**(2), 293-310.

[2] Amin M: A method for approximating the nodal modulations of the real tide. *International Hydrographic Review*, 1987, **64**(2), 103-113.

[3] Amin M: Superfine resolution of tidal harmonic constants. In Parker BB ed. *Tidal Hydrodynamics*, John Wiley & Sons, Inc., 1991, 711-724.

[4] Darwin GH: Reports of a committee for the harmonic analysis of tides. *British Association for the Advancement of Science*, 1883-1886.

[5] Doodson AT: The harmonic development of the tide-generating potential. *Proceedings of the Royal Society of London Series A. Mathematical and Physical Sciences*, 1921, **100**, 305-329.

[6] Dronkers JJ: *Tidal computations in rivers and coastal waters*. Amsterdam: North-Holland Publishing Co, 1964.

[7] George KJ & Simon B: The species concordance method of tide prediction in estuaries. *International Hydrographic Review*, 1984, **65**(1), 121-146.

[8] Goertzel G: An algorithm for the evaluation of finite trigonometric series. *The American Mathematical Monthly*, 1958, **65**(1), 34-35.

[9] Harris RA: Manual of tides. *Appendices to Reports of the U.S. Coast and Geodetic Survey*, 1897-1907.

[10] Newton I: *Philosophia Naturalis Principia Mathematica*, 1687.

[11] Simon B: The species concordance method of tide prediction. In Parker BB ed. *Tidal Hydrodynamics*, John Wiley & Sons, Inc., 1991, 725-735.

[12] Thomson W: Reports of committee for harmonic analysis. *British Association for the Advancement of Science*, 1868-1876.

Proceeding of the Tenth Asian Congress of Fluid Mechanics
17-21 May 2004, Peradeniya, Sri Lanka

ESTABLISHING TIDAL DISCHARGE BOUNDARIES BASED ON INCOMPLETE FIELD DATA FOR A HYDRODYNAMIC MODEL OF A COASTAL AREA

S. Kumuthini, M.M.G.S. Fernando and R. Galappatti
Lanka Hydraulic Institute, Katubedda, Moratuwa, Sri Lanka

ABSTRACT: The coastal reach in Beruwela, adjacent to the Bentara river estuary in the southwest of Sri Lanka is known as the "Golden Mile" on account of intensive tourism development along the beachfront. The stability of this coastal reach depends on tidal dynamics of the estuary as well as the outflow of sand and water from the river. The river outlet alternates on either side of a small rocky island every decade or so, causing seasonal erosion of different parts of this coastal stretch. In order to develop proposals to stabilise this coastal reach, mathematical models were established to simulate the behaviour of the beaches.

This paper describes the two-dimensional hydrodynamic model set up for this exercise. The paper discusses the measures taken to overcome difficulties that arose when it was found that the field measurements made for establishing boundary conditions for the model were found to be inadequate for directly establishing a viable tidal discharge boundary either for calibration or for simulating the required scenarios. In particular it describes the use of a one-dimensional model of the Bentota River to provide the necessary boundary conditions for the two-dimensional model.

1. INTRODUCTION

The impact of coastal erosion is quite evident along Sri Lanka's West, Southwest and South coasts and it is more pronounced and complicated closer to the river mouths. Bentara River mouth on the Southwest coast of Sri Lanka plays an important role in the stability of prime tourist beaches in Beruwela and Bentota. Combined action of the wave attack and the current pattern associated with the dynamics of the estuary play a key role on the stability of the coast. The current patterns in this area are characterised by a rocky island (previously a headland) in the shallow coastal waters in front of the river mouth. If the river outlet falls between the rock and the southern coast, then there is a kind of tombolo formation from the shore to the rock, and the beach is well nourished. If the river outlet shifts to a location between the rock and the northern beach, the beach first gets heavily eroded and then recovers slowly. In recent times, the river outlet has been seen between the rock and the northern beach. On occasion, the beach hotels adjacent to the river mouth have suffered heavy beach erosion.

2. MATHEMATICAL MODELS

A two-dimensional model (MIKE21) and a one-dimensional model (MIKE11) developed by DHI Water and Environment (formerly Danish Hydraulic Institute) have been applied to simulate tide, wave and discharge at the Bentara River mouth. For the present study three different modules of MIKE products were applied:

- Hydrodynamic Module, MIKE21 HD
- Nearshore Spectral Wind-Wave Module, MIKE21 NSW
- Hydrodynamic Module, MIKE11 HD

2.1 Hydrodynamic Module, MIKE21 HD

It is a general modelling system for the simulation of water levels and flows in estuaries, bays and coastal area. It simulates unsteady two-dimensional flows in one layer (vertically homogeneous) fluid.

The following equations, the conservation of mass and momentum integrated over the vertical, describe the flow and water level variations.

$$\frac{\partial \zeta}{\partial t} + \frac{\partial p}{\partial x} + \frac{\partial q}{\partial y} = \frac{\partial d}{\partial t} \tag{1}$$

$$\frac{\partial p}{\partial t} + \frac{\partial}{\partial x}\left(\frac{p^2}{h}\right) + \frac{\partial}{\partial y}\left(\frac{pq}{h}\right) + gh\frac{\partial \zeta}{\partial x} + \frac{gp\sqrt{p^2+q^2}}{C^2h^2} - \frac{1}{\rho_w}\left[\frac{\partial}{\partial x}\left(h\tau_{xy}\right) + \frac{\partial}{\partial y}\left(h\tau_{xy}\right)\right] - \Omega q - fVV_x + \frac{h}{\rho_w}\frac{\partial}{\partial x}\left(p_a\right) = 0 \tag{2}$$

$$\frac{\partial q}{\partial t} + \frac{\partial}{\partial y}\left(\frac{q^2}{h}\right) + \frac{\partial}{\partial x}\left(\frac{pq}{h}\right) + gh\frac{\partial \zeta}{\partial y} + \frac{gq\sqrt{p^2+q^2}}{C^2h^2} - \frac{1}{\rho_w}\left[\frac{\partial}{\partial y}\left(h\tau_{xy}\right) + \frac{\partial}{\partial x}\left(h\tau_{xy}\right)\right] - \Omega p - fVV_y + \frac{h}{\rho_w}\frac{\partial}{\partial y}\left(p_a\right) = 0 \tag{3}$$

where, $h\,(x,y,t)$ - water depth (m)

$d\,(x,y,t)$	- time varying water depth (m)
$\zeta\,(x,y,t)$	- surface elevation (m)
$p,q(x,y,t)$	- flux density in x and y directions ($m^3/s/m$)
$C(x,y)$	- Chezy resistance ($m^{1/2}/s$)
g	- acceleration due to gravity (m/s^2)
$f\,(V)$	- wind friction factor
$V,\ V_x,\ V_y(x,y,t)$	- wind speed and components in x and y directions (m/s)
$\Omega\,(x,y,t)$	- Coriolis parameter, latitude dependent (s^{-1})
$p_a(x,y,t)$	- atmospheric pressure ($kg/m/s^2$)
$\rho_w(x,y,t)$	- density of water (kg/m^3)
x,y	- space co-ordinates (m)
t	- time (s)
$\tau_{xx},\ \tau_{xy},\ \tau_{yy}$	- components of effective shear stress

2.2 Nearshore Spectral Wind-Wave Module, MIKE21 NSW

The basic equations in the model are derived from the conservation equation for the spectral action density. A parameterization of this equation in the frequency domain is performed introducing the zeroth and first moment of the action spectrum as dependent variables. This leads to the following coupled partial differential equations:

$$\frac{\partial(c_{gx}m_0)}{\partial x}+\frac{\partial(c_{gy}m_0)}{\partial y}+\frac{\partial(c_\theta m_0)}{\partial \theta}=T_0 \quad (4)$$

$$\frac{\partial(c_{gx}m_1)}{\partial x}+\frac{\partial(c_{gy}m_1)}{\partial y}+\frac{\partial(c_\theta m_1)}{\partial \theta}=T_1 \quad (5)$$

Where,

$m_0(x,y,\theta)$	- zeroth momentum of the action spectrum
$m_1(x,y,\theta)$	- first momentum of the action spectrum
c_{gx} and c_{gy}	- group velocity C_g components in x and y direction
c_θ	- propagation speed representing the change of action in the θ direction
x and y	- Cartesian co-ordinate
θ	- direction wave propagation
T_0 and T_1	- source terms

The momentum $m_n(\theta)$ are defined

$$m_n(\theta)=\int_0^\alpha \omega^n A(\omega,\theta)d\omega$$

Where ω is the absolute frequency and A is the spectral wave action density.

Wave-induced currents can be well described by radiation stresses S_{xx}, S_{yy} and S_{xy}.

$$S_{xx}=\frac{1}{2}\rho g\ \left(F_u + F_p\right) \quad (6)$$

$$S_{xy}=\frac{1}{2}\rho g\ \ F_{uv} \quad (7)$$

$$S_{yy}=\frac{1}{2}\rho g\ \left(F_v + F_p\right) \quad (8)$$

Where,

$$F_v=\int_0^{2\pi}\sin^2\theta.(1+G)E(\theta)d\theta$$

$$F_{uv}=\int_0^{2\pi}\sin\theta\cos\theta.(1+G)E(\theta)d\theta$$

$$F_u=\int_0^{2\pi}\cos^2\theta.(1+G)E(\theta)d\theta$$

$$F_p = \int_0^{2\pi} G.E(\theta)d\theta$$

$$G = \frac{2kd}{\sinh 2kd}$$

3. MODEL SET UP

Due to the fact that the tidal differences of the boundaries are small within the area of interest, it was not safe to drive a small model reliably by using only tidal water levels. Therefore, the HD modelling was carried out on a nested grid set up starting from a larger regional model and gradually reducing to smaller models while moving towards the area of interest.

A 1000m **x** 1000m grid regional model (coarse model), which extends from Galle in the south, up to Kalpitiya in the north, was set up with the bathymetry information extracted from the relevant Admiralty chart supplemented with measured local bathymetry.

A local model of 25m **x** 25m was required in this study to secure better resolution. Since it was not possible to step down from the established regional model to the 25m **x** 25m local model directly due to limitations on interpolation, an intermediate model of 250m **x** 250m grid was also introduced for smooth transformation.

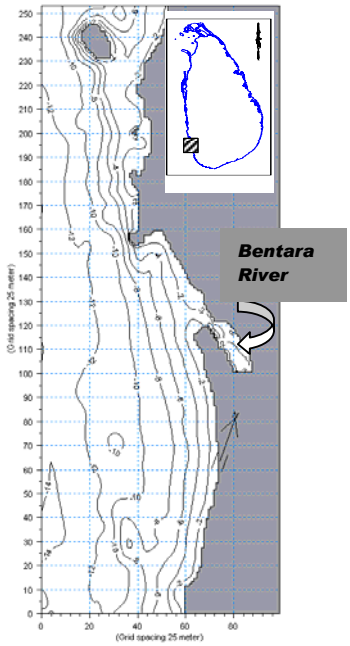

Fig. 1: Study Area

Figure 1 shows the local model and Table 1 shows the model grid definition.

Table 1: Model Grid Definition

	Regional Model	Intermediate Model	Local Model
Origin (easting, northing)(m)	80000, 67750	98000, 100000	112500, 134800
Orientation (deg)	10	20	20
Model size (km x km)	358 x 88	65.50 x 34.75	6.3 x 2.4
Grid spacing (m)	1000	250	25

Tidal levels from Kalpitiya and Galle predicted from tidal constituents (From Admiralty Tide Tables) as listed in Table 2, are applied at the northern and southern boundaries of the regional model, respectively.

Table 2: Derived Tidal Constituents for the Northern and Southern boundaries of the Regional Model

Boundary	Derived Amplitude of Tidal Constituents				Derived Phase of Tidal Constituents			
	M2	S2	K1	O1	M2	S2	K1	O1
Kalpitiya	0.12	0.08	0.06	0.03	97	147	71	91
Galle	0.16	0.11	0.05	0.01	56	99	21	73

Model Calibration

In order to rely on the results of any modelling study, the model should be calibrated and verified to a satisfactory accuracy. In "coarse modelling", calibration was carried out against predicted water levels and the results are presented in Figure 2. Bed resistance and eddy viscosity were the main calibration parameters considered.

Table 3: Tidal Constituents for calibration and verification of water level predictions in Regional Model

Boundary	Derived Amplitude of Tidal Constituents				Derived Phase of Tidal Constituents			
	M2	S2	K1	O1	M2	S2	K1	O1
Colombo	0.18	0.12	0.07	0.03	46	93	32	59
Hikkaduwa	0.13	0.09	0.04	0.02	45	86	21	68

Comparison of predicted and simulated water levels at Colombo showed good agreement. Calibrated model is validated against predicted tide at Hikkaduwa (Figure 3).

----- Predicted Tide at Colombo
___ Simulated Tide at Colombo

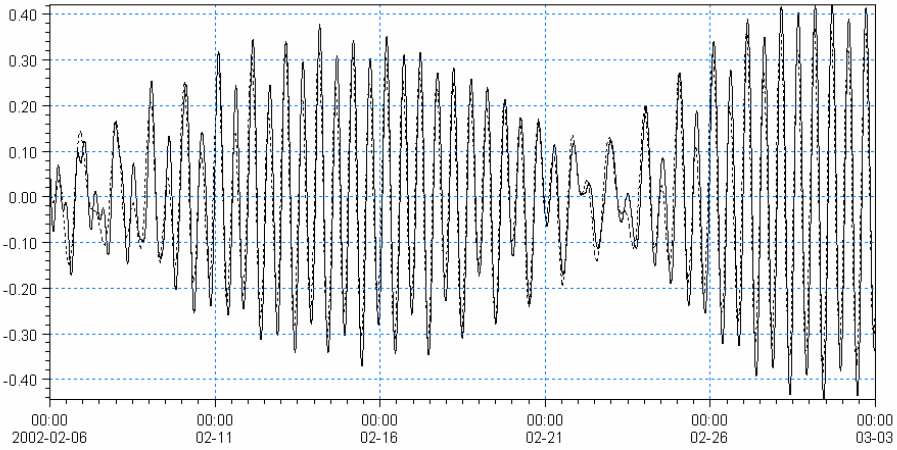

Fig. 2: Model Calibration - Comparison of Tide at Colombo

] ----- Predicted Tide at Hikkaduwa Tide at Hikkaduwa
___ Simulated Tide at Hikaduwa

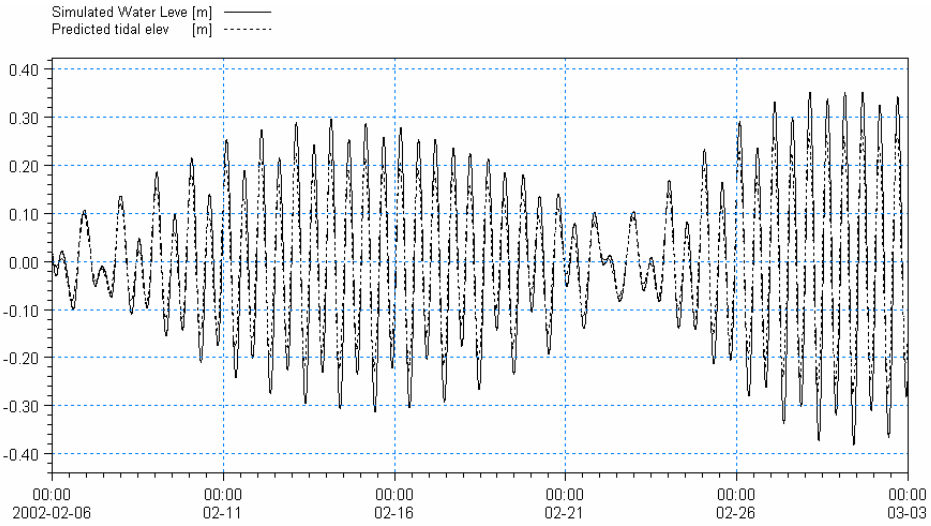

After the calibration of the regional model, boundary conditions for wet and dry seasons were extracted for the intermediate model. Having introduced these boundary conditions, simulations were carried out with the intermediate model. Similarly appropriate boundary conditions for the local model were extracted.

4. LOCAL MODEL SET UP

For the local model, discharge time series for the boundary of Bentara River was considered. In order to gather the required data, a self-recording current meter (Anderaa RCM7) was deployed 600m upstream of the river mouth. Analysis of velocity data indicated that the flood volume in a tidal cycle was higher than the ebb volume. After the possibility of instrument malfunction having been eliminated, it was concluded that the flow was either returning along another path, or the current meter was affected by the saline wedge. Additional detailed measurements were carried out to clarify the process. Eventually it was decided that there was no satisfactory method of processing the current meter data to obtain a viable inflow boundary time series.

The final solution adopted was to survey a longer reach of the river and use a MIKE11 model of the river and which could be calibrated against the field measurements (Figure 4). This model was used to simulate the tidal boundary two kilometres upstream of the original model boundary. The use of a MIKE11 model to obtain the upstream tidal discharge time series of the MIKE21 model gives the additional advantage of generating different seasonal flows.

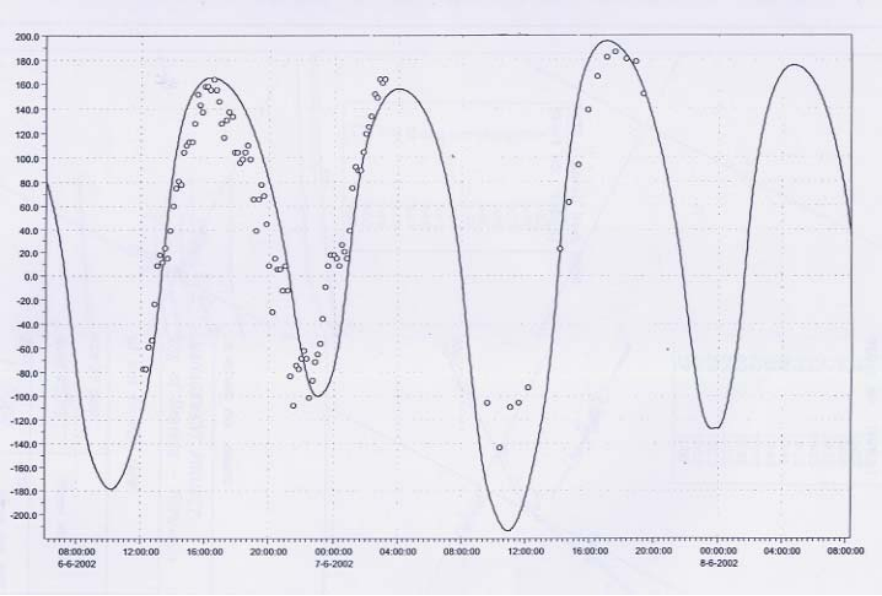

Figure 4: Calibration of MIKE11 HD Model against Measured Data

Three different coastal stabilisation schemes were considered in this study. Simulations were carried out for different combinations of tides, waves (sea & swell), wave induced currents and different discharges in the river. Wave induced currents were introduced by applying wave radiation stresses generated by Nearshore Spectral Wave Model (NSW). Model studies were carried out in an interactive manner and some of the interesting findings are presented in Figure 5.

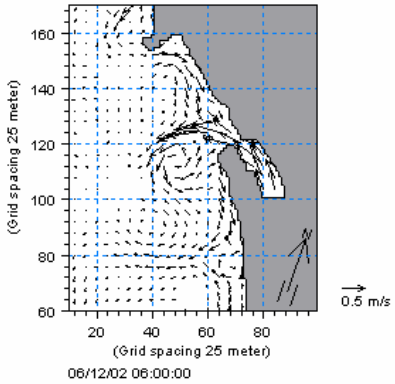
(Grid spacing 25 meter)
(Grid spacing 25 meter)
0.5 m/s
06/12/02 06:00:00

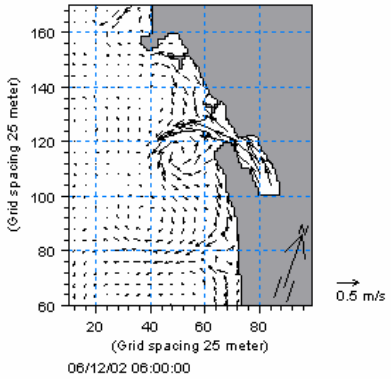
(Grid spacing 25 meter)
(Grid spacing 25 meter)
0.5 m/s
06/12/02 06:00:00

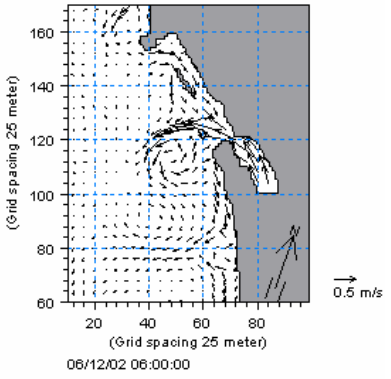
(Grid spacing 25 meter)
(Grid spacing 25 meter)
0.5 m/s
06/12/02 06:00:00

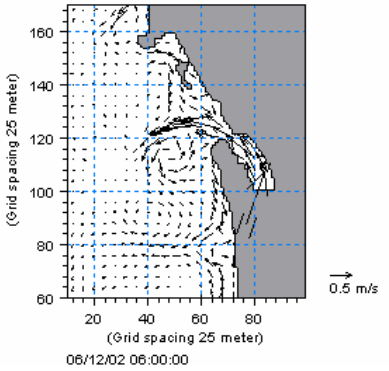
(Grid spacing 25 meter)
(Grid spacing 25 meter)
0.5 m/s
06/12/02 06:00:00

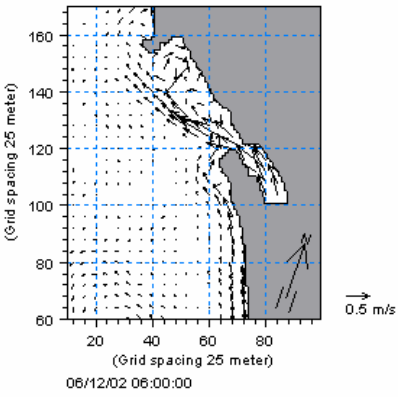
(Grid spacing 25 meter)
(Grid spacing 25 meter)
0.5 m/s
06/12/02 06:00:00

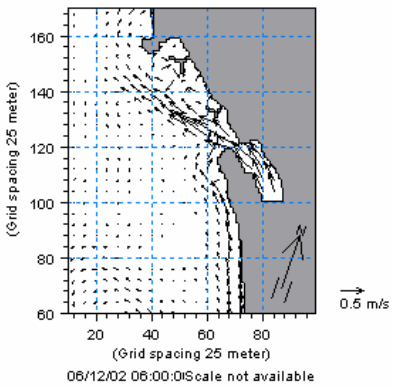
(Grid spacing 25 meter)
(Grid spacing 25 meter)
0.5 m/s
06/12/02 06:00:0Scale not available

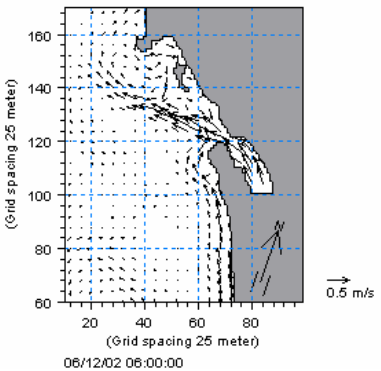
(Grid spacing 25 meter)
(Grid spacing 25 meter)
0.5 m/s
06/12/02 06:00:00

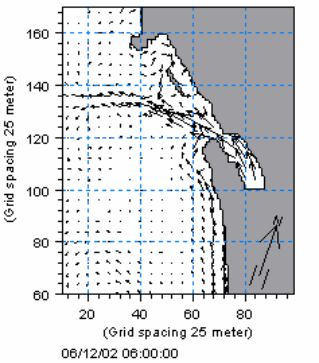
(Grid spacing 25 meter)
(Grid spacing 25 meter)
06/12/02 06:00:00

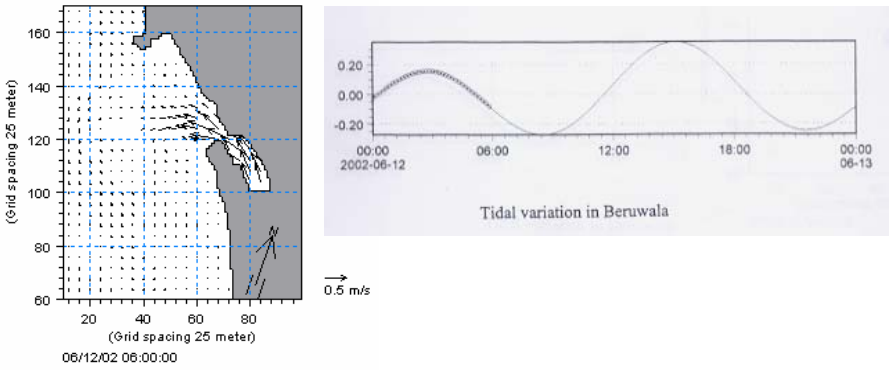

Figure 5: Vector Plots of Currents during SW Monsoon – Spring Tide (Ebb Flow)

5. CONCLUSION

The numerical model established in the present study was used as a tool for studying and evaluating the alternatives proposed by the designers of the coastal stabilisation scheme in Bentota-Beruwela. The inadequacy of field data gathered for providing a realistic tidal discharge boundary on the river was overcome by using a one-dimensional model to improve and extend the field data gathered. The methodology developed out of necessity in this project is now being applied at other locations in Sri Lanka.

ACKNOWLEDGEMENT

Coastal Resources Management Project (Coastal Stabilisation Component) identified 7 sites on the West Coast of Sri Lanka. Beruwela–Bentota is one of the identified sites. This study was carried out by Lanka Hydraulic Institute under the sub contract with NIRAS Portconsult a/s.

REFERENCES

[1] Lanka Hydraulic Institute, Hydrodynamic Model Study of Bentota – Beruwala Area, 2002.

[2] NIRAS Portconsult a/s, Coastal Resources Management Project- Stabilisation Component, Draft Detailed Design Report, 2001.

[3] PRIMIX – LHI, Coastal Resources Management Project, Sri Lanka (TA No. 3034 – SRI), 1999.

[4] The United Kingdom Hydrographic Office, Admiralty Tide Table Vol. 3, 2002.